Physics-based synthesis of wind turbine noise

David Mascarenhas

INSTITUT POLYTECHNIQUE DE PARIS

NNT : 2022IPPAE020

Thèse de doctorat

Physics-based synthesis of wind turbine noise

Thèse de doctorat de l'Institut Polytechnique de Paris
préparée à l'École nationale supérieure de techniques avancées

École doctorale n°626 École doctorale de l'Institut Polytechnique de Paris (EDIPP)
Spécialité de doctorat : Mécanique des fluides et des solides, Acoustique

Thèse présentée et soutenue à Palaiseau, le 14 Décembre 2022, par

DAVID MASCARENHAS

Composition du Jury :

Catherine Lavandier Professeur, Université de Cergy-Pontoise	Présidente
François Coulouvrat Directeur de recherche, CNRS	Rapporteur
Marc Jacob Professeur, École Centrale de Lyon	Rapporteur
Hadrien Beriot Ingénieur de recherche, Siemens Digital Industries Software	Examinateur
Julien Maillard Ingénieur de recherche, CSTB	Examinateur
Olivier Doaré Professeur, ENSTA Paris	Directeur de thèse
Benjamin Cotté Maître de conférence, ENSTA Paris	Co-directeur de thèse

Abstract

It is known that wind turbine noise is a potential source of annoyance and sleep disturbance for the people living in the vicinity of wind farms. The goal of this work is to develop a physics-based wind turbine noise synthesis tool that is validated against field measurements. The frequency-domain model for wind turbine noise predicts the broadband aerodynamic noise generated by the moving blades interacting with the turbulent atmosphere. It is based on Amiet's theory and includes both the trailing edge noise for a turbulent boundary layer and the leading edge noise associated with a turbulent inflow. The parabolic equation in moving medium is used to account for the refraction and ground reflection effects, while the Harmonoise model is considered to account for the scattering due to turbulence. The noise from the blade segments are synthesized as monopoles, moving through different layers of the atmosphere. A synthesis tool is created to convert the frequency-domain noise predictions to a time signal with the help of a cross-fading window function. The window function is designed to account for the difference in the propagation time between one blade segment and a fixed receiver due to the rotation. Sounds are synthesized for various test cases to emphasize the influence of the ground impedance, of wind shear, of turbulence scattering and of the shadow zone on wind turbine noise. The model predictions are finally compared to field measurements for a wind farm of eight turbines. The source model is validated first, and then fairly good predictions are obtained with the complete model at distances between 350m and 1.4km from the closest wind turbine. The developed model can be used for psychoacoutic evaluation to understand the perception and annoyance factor of wind turbine noise.

Keywords: wind turbine noise, physics-based synthesis, turbulent inflow noise, trailing edge noise, adaptive window function, physical validation, parabolic equation

Résumé

Le bruit des éoliennes est une source potentielle de gêne et de troubles du sommeil pour les personnes vivant à proximité des parcs éoliens. Une caractéristique notable du bruit des éoliennes est la modulation d'amplitude du bruit aérodynamique à large bande généré par les pales tournant dans une atmosphère turbulente. L'objectif de ce travail est de développer un outil de synthèse du bruit des éoliennes basé sur des modèles physiques capable de produire des signaux audio reproduisant ses principales caractéristiques.

Le modèle de bruit des éoliennes dans le domaine fréquentiel prédit le bruit aérodynamique large bande généré par les pales en mouvement qui interagissent avec l'atmosphère turbulente. Il est basé sur la théorie d'Amiet et comprend à la fois le bruit de bord de fuite pour une couche limite turbulente et le bruit de bord d'attaque associé à un écoulement amont turbulent. Les pales sont divisées en un certain nombre de segments et le bruit généré en champ libre est prédit pour chaque segment de pale en rotation, en prenant en compte l'effet Doppler et l'amplification convective. L'équation parabolique en milieu en mouvement est utilisée pour tenir compte des effets de réfraction atmosphérique et de la réflexion des ondes acoustiques sur un sol d'impédance finie. Il s'agit d'une des principales originalités du modèle par rapport aux études précédentes, car cette formulation évite d'utiliser l'approximation de vitesse du son effective pour prendre en compte les gradients verticaux de vent. Un terme empirique issu du modèle Harmonoise est utilisé pour tenir compte de la diffusion acoustique due à la turbulence, et l'effet de l'absorption atmosphérique est inclus dans les prédictions. Suivant le modèle de monopôles mobiles, l'équation parabolique est calculée pour un nombre fixe de hauteurs réparties sur le plan de rotation de l'éolienne.

Un outil de synthèse est développé pour convertir les prévisions de bruit dans le domaine fréquentiel en un signal temporel à l'aide d'une transformée de Fourier discrète inverse. Le bruit rayonné par chaque segment passant par des transitions angulaires discrètes est synthétisé et les transitions entre les signaux successifs sont lissées à l'aide d'une fonction de fondu enchaîné. La fenêtre utilisée pour le fondu enchainé est conçue pour tenir compte de la différence de temps de propagation entre un segment de pale en rotation et le récepteur fixe. Une étude est réalisée pour trouver les valeurs optimales du taux de recouvrement et du pas de discrétisation angulaire. Des sons sont ensuite synthétisés pour différents cas-test afin de souligner l'influence de l'impédance au sol, du cisaillement du vent, de la diffusion par la turbulence et de la zone d'ombre sur le bruit des éoliennes.

Pour la validation du modèle, une campagne de mesures sur un parc éolien contenant huit éoliennes est étudiée. Les données météorologiques et fonctionnelles des éoliennes ainsi que les enregistrements acoustiques réalisés au cours de 10 jours d'observation intensive sont analysées. Les données météorologiques et fonctionnelles des éoliennes sont prises comme entrées pour le modèle et le résultat du modèle est comparé aux données acoustiques enregistrées. Le modèle de source est validé par rapport à des données acoustiques enregistrées au sol à proximité d'une éolienne afin de minimiser les effets de propagation. En vent de travers, le modèle d'Amiet tend à sous-estimer les niveaux acoustiques, comme cela a déjà été montré dans la littérature. L'introduction d'une correction dans la directivité du modèle d'Amiet permet d'obtenir des niveaux en bon accord avec les mesures. Le modèle complet est ensuite comparé aux données acoustiques enregistrées à des hauteurs comprises entre 1,5 m et 2 mètres à des distances comprises entre 350 et 1400 mètres de l'éolienne la plus proche. De bonnes prédictions sont obtenues à la fois sous

le vent et contre le vent, même si l'influence du bruit de fonds est plus significative pour les grandes distances de propagation.

Ce projet de thèse ouvre de nombreuses perspectives. Tout d'abord, il est envisageable d'inclure dans le modèle fréquentiel d'autres de bruit d'éolienne telles que le bruit de décrochage, le bruit mécanique, et le bruit d'interaction pale-mât. Il est également possible d'ajouter un bruit de fonds pour rendre le signal synthétisé plus réaliste. L'outil de synthèse développé permet d'auraliser le bruit des parcs éoliens pendant la phase de conception, ce qui peut être utile pour dialoguer avec les riverains et les collectivités locales. Enfin, le modèle peut être utilisé pour l'évaluation psychoacoustique afin de mieux comprendre la perception du bruit des éoliennes et la gêne associée.

Mots clés: le bruit des éoliennes, synthèse par modèles physiques, bruit d'interaction de turbulence, bruit de bord de fuite, fonction de fondu enchaîné, validation physique, équation parabolique

Acknowledgements

Firstly, I would like to thank my parents Joseph and Angela Mascarenhas for their constant and undying support throughout my life. I am full of gratitude for the help and support of Christina, Reuben, Gabriella, Olivia and Lucia Lobo, Naomi, Issac, Veronica and Isabelle Nile and Peter Mascarenhas. Secondly, I would like to thank Benjamin Cotté and Olivier Doaré for their guidance during the thesis, encouragement and most importantly their patience with me. The motivation and drive for research from both of them was always transmissible and is forever inspiring. I appreciate the support and help from all my friends in the lab and outside who were always kind towards me during every rough time. I thank the team and lab of CEREMA, especially David Ecotière for the hospitality extended towards me during my secondment in Strasbourg. Lastly, for all future doctorate students I pass on to you a very valuable piece of advice which was given to me by an experienced doctorate student: *"It is just a PhD"*. During the COVID pandemic crisis of 2020, I lost numerous friends and also family due to the pandemic. Faced with situations of life and death, it makes one reconsider the set priorities. It is without any doubt that a thesis can be exceedingly stressful at times. Take a break, listen to music, but do not give up because the finale is so close. But remember that eventually "It is just a PhD".

This project has received funding from the European Union's Horizon 2020 research and innovation program under the Marie Sklodowska-Curie grant agreement No. 812719.

Contents

List of Figures

List of Tables

List of Symbols

α	Wind shear exponent
α_{abs}	Atmospheric absorption coefficient
β_z	Elevation angle between the observer and the plane of the airfoil
β_c	Clauser's parameter
ΔL	Total sound pressure level relative to free field
ΔL_{PE}	Relative sound pressure level due to the propagation effects obtained by the WAPE in moving medium
ΔL_{scat}	Relative sound pressure level due to the scattering due to turbulence obtained by the Harmonoise model
Δ	Zagarola and Smits's parameter (δ/δ^*)
δ	Boundary-layer thickness
δ^*	Boundary-layer displacement thickness
ϵ	Turbulence dissipation rate
γ	Blade angular position with respect to the z-axis
Λ	Turbulence integral length scale
λ	Wavelength of the sound
$\mathcal{A}$	Directivity correction of the airfoil in percentage.
$\mathcal{D}$	Directivity of the airfoil
$\mathcal{L}_{\mathcal{TI}}$	aeroacoustic transfer function for the turbulent inflow noise
$\mathcal{L}_{TE}$	Transfer function for trailing edge noise
ν	Kinematic viscosity
Ω	Rotational speed of the blades
ω	Angular frequency
Φ_{pp}	Wall pressure fluctuation spectrum (WPS)
Φ_{ww}	2D energy spectrum of the vertical velocity fluctuations
Π	Wake strength parameter
Ψ	Overlap amount
ρ_0	Air density
τ_w	Wall shear stress

τ_{max}	Maximum shear stress along the normal distance
c	Chord length of the airfoil
c_0	Speed of sound
C_f	Friction coefficient
C_K	Kolmogorov constant
C_T	Turbulent structure parameters for temperature fluctuations
C_v	Turbulent structure parameters for wind speed fluctuations
f	Frequency
k	Acoustic wave number
L	Span length of the airfoil
l_y	Spanwise coherence length
N_γ	Number of discrete angular position
p_{ref}	Reference pressure 2×10^{-5}Pa
R	Direct distance between the source and the receiver
R_T	Ratio of the outer to inner boundary layer time scales
Re_θ	Momentum-thickness-based Reynolds number
S_{pp}	Power spectral density
t_p	Propagation time
t_r	Receiver time
t_s	Emission time
u_*	Friction velocity
U_0	Inflow velocity of the flow
U_c	Convected velocity
U_e	Velocity at the boundary-layer edge
U_{ref}	Reference wind speed at the height z_{ref}

List of Acronyms

SPL_{FF}	Sound pressure level in free field
SPL	Sound pressure level
OASPL	Overall A-weighted Sound pressure level
AM	Amplitude modulation
TIN	Turbulent inflow noise
TEN	Trailing edge noise
PSD	Power spectral density
WPS	Wall pressure spectrum
APG	Adverse pressure gradient
ZPG	Zero pressure gradient
MOST	Monin-Obukhov similarity theory
WAPE	Wide angle parabolic equation
IDFT	Inverse Discrete Fourier Transform
PIBE	Prévoir l'impact du bruit des éoliennes
IEC	International Electrotechnical Commission
POI	Period of Intensive Observation
SCADA	Supervisory Control and Data Acquisition
WT	Wind Turbine
LIDAR	Light Detection and Ranging
TDR	Turbulence Dissipation Rate

1

Introduction

Contents

1.1 Wind energy and wind turbines

There is a pressing need in the present time for the replacement of conventional electrical energy sources that depend on perishable and polluting resources such as fossil fuels. A recent study on the impact of the carbon footprint and CO_2 emission levels has shown that this substitution is urgent [42]. The necessary replacement is to be done with green, renewable sources of energy that are not harmful to the environment. A report from the World Energy Outlook [41] shows the maximum consumption of coal for electricity generation in the year 2019 (See Fig. 1.1). Possible replacements of such non-renewable sources are hydro energy, solar energy and wind energy. The initiative undertaken in the form of building wind farms has been on a steady rise in many countries [65, 52]. As of 2020, the Global Wind Energy Council [44] reports that the total installed onshore wind turbines represent a capacity of 194GW in Europe (27% of the total), including 17GW in France (See Fig. 1.2). Recent studies conclude that the wind energy sector may continue to grow worldwide as long as the factors critical to its development are addressed [36].

One of the factors that hinder the progressive development of wind farms is the noise generated by the wind turbines [58]. This noise generated by the blades of the wind turbines have been known to cause annoyance and possibly disturbances in sleep patterns leading to decreased quality of life [85, 66, 57]. This significant factor is taken into account by imposing noise level restrictions that can lead to the wind

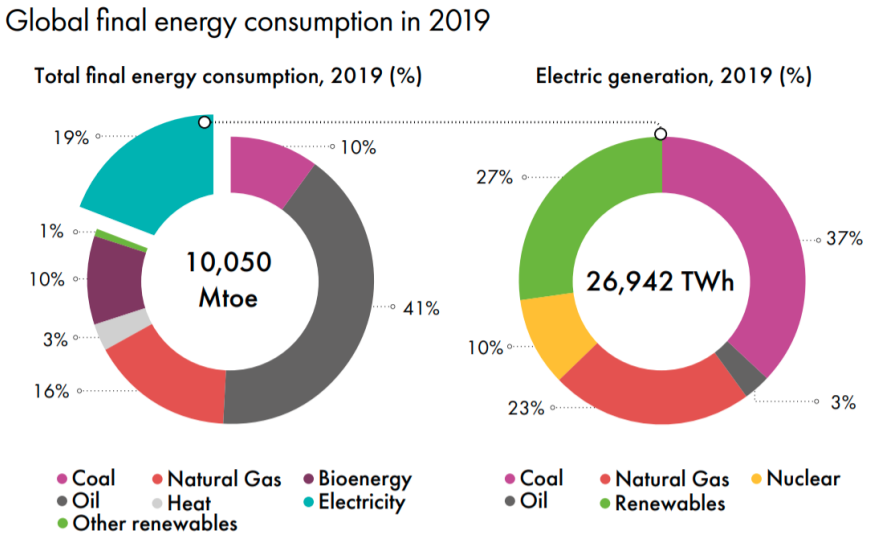

Figure 1.1: Schematics of the total global energy consumption in 2019 [41].

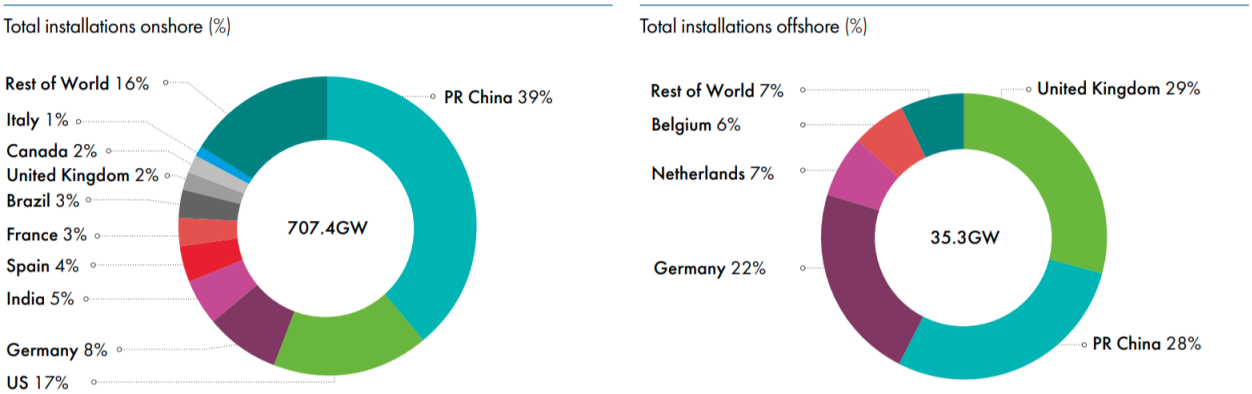

Figure 1.2: Schematics of the number of installed wind turbines in 2020 [44].

farm's temporary or permanent shutdown [95, 48]. In France, the regulation states that the emergence noise levels from a wind farm should be less than 5 dBA during the day and less than 3 dBA during the night [5, 48]. This decommissioning or inactivity of the wind farms leads to direct ecological as well as economical impacts. For example, a single inactive 2.3MW wind turbine needs to be substituted with replacement energy sources mainly based on coal, oil and natural gas. Scaled up to a level of a wind farm, this ecological impact can be significant.

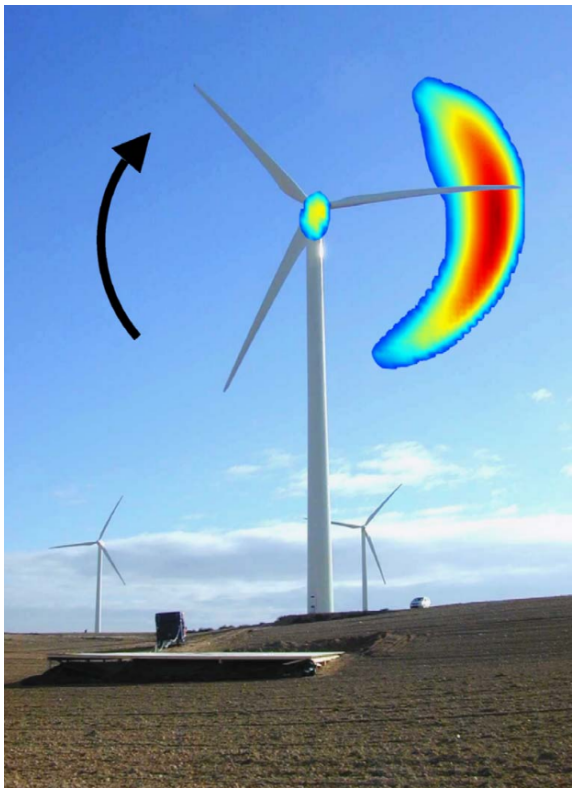

Figure 1.3: Noise source distribution in the rotor plane of a wind turbine of rotor diameter 58m, measured by Oerlemans *et al.* [64] with a microphone array located on a horizontal platform 58m upwind from the wind turbine.

1.2 Importance of the synthesis model for wind turbine noise

The trade-off between the noise-caused impacts and the power production of the wind farms strongly emphasises the importance of research on wind turbine noise. Studies analyzing the mechanisms of wind turbine noise sources have been carried out with success [64, 63, 99]. One of the characteristics of wind turbine noise is the modulation in the level of the broadband aerodynamic noise which is caused by the rotation of the blades. Fig. 1.3 shows the noise distribution in the rotor plane of a modern wind turbine measured by Oerlemans *et al.* [64] using a microphone array. As shown in the figure, most of the noise is produced during the downward motion of the blade, which can be attributed to convective amplification and the directivity of trailing edge noise. The noise from the trailing edge of the wind turbine blade can be related to the boundary layer fluctuations occurring at the trailing edge of the wind turbine blade. Similarly, the turbulent gusts interacting with the leading edge of the blade or occasionally boundary layer separation noise occurring at high angles

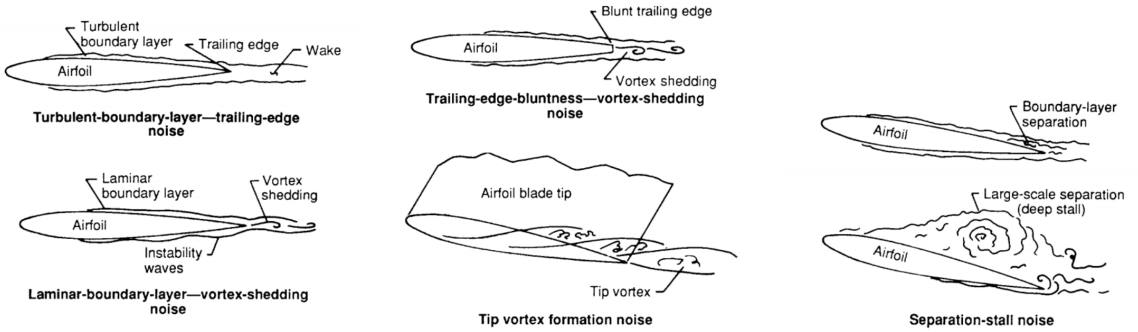

Figure 1.4: Airfoil self-noise mechanisms. Taken from Brooks *et al.* [16].

of attack [62, 9] are other noise generating mechanism that contribute to the wind turbine noise. Certain noise generating mechanisms of the blade are always present and are called airfoil self noise as schematically shown in Fig.1.4. Other sources of noise from a wind turbine are blade-tower interaction producing tonal noise [98, 97], mechanical noise, etc. The amplitude modulation (AM) noise fluctuations that occur at the blade passing frequency is typically between 0.5 Hz to 0.8 Hz. Having a model of the wind turbine noise that is able to predict the noise levels accurately would be helpful but not sufficient. It is also important for the wind turbine noise model to be able to synthesize time signals of the predicted noise for psychoacoustic analysis. The eventual outcome of the model would be to synthesize the expected noise in the vicinity of the desired wind turbine.

In general there exist two types of synthesis techniques, namely sample-based and physics-based [94]. Sample-based synthesis consists in analysing pre-recorded signals and processing them as per desired. However, this technique does not allow us to have much control on the physical input parameters of the system and is limited by the extent of the recording database. As this technique is based on recordings it is known to be occasionally contaminated by background noise. Using a physics-based synthesis technique, there is greater control over the parameters influencing the noise mechanisms that need to be studied and there is no influence of background noise. It is important for the wind turbine noise prediction model to be physics-based so that the individual parameters owing to the generation of the noise can be studied with clarity. In the literature a few sampled-based wind turbine noise synthesis tools exist [77, 88], and the physics-based approach used in this study has not been developed until recently [14].

Two fundamental components need to be considered for the realistic synthesis of wind turbine noise. Firstly, the aeroacoustic sources that originate from the leading and trailing edges of the wind turbine blades can be modelled as moving

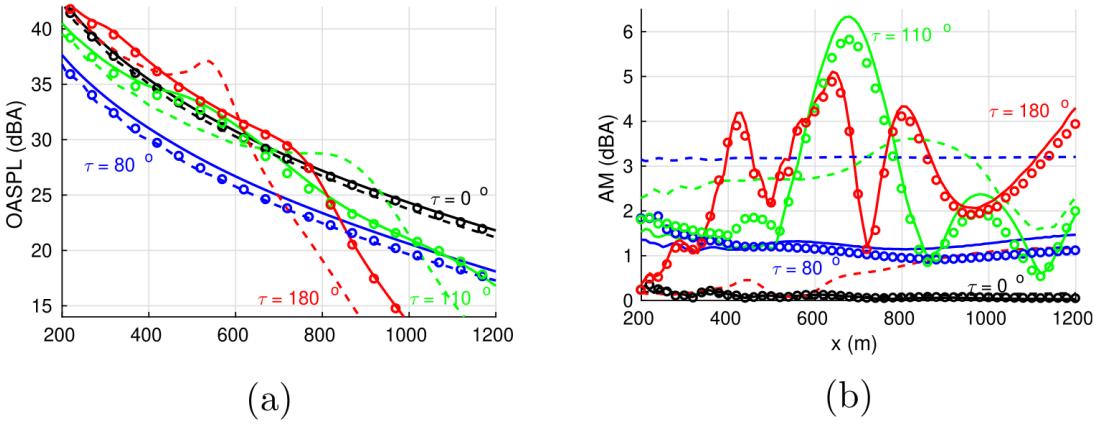

Figure 1.5: (a) OASPL and (b) AM of the predicted wind turbine noise for different receiver positions [64]. The receiver orientation with respect to the wind direction is shown as τ, with $\tau = 0°$ corresponding to the downwind direction.

monopoles. Secondly, the noise spectrum of the source is modified due to the propagation effects in an outdoor environment [7, 20]. The aeroacoustic sources from the wind turbine blades which originate from the leading edge and trailing edge can be modelled as moving monopoles. The noise spectrum emitted by the source is modified due to the effects of propagation. One of the propagation effect is atmospheric absorption that acts as a low-pass filter. Interference patterns are observed due to the ground reflection and upward or downward refraction of the sound paths occur due to the wind speed vertical gradients. When the noise is propagating upwind, upward refraction produces an acoustic shadow zone at some distance from the wind turbine that depends on the source and receiver heights. The noise level in the shadow zone is highly dependent on atmospheric turbulence fluctuations that scatter acoustic waves into these shadow zones [84, 11]. Coupling the source and propagation models of wind turbine noise gives varied noise levels depending on the position of the receiver. Fig. 1.5 shows the predicted Overall A-weighted Sound pressure level (OASPL) and the amplitude modulation (AM) of the wind turbine noise for different receiver orientations and distances. The low OASPL but high AM is seen in the crosswind direction as expected. The shadow zone can be clearly seen from the steep decrease of the OASPL above 800m for $\tau = 180°$ and above 1000m for $\tau = 110°$ and the high level of the AM is seen for the same directions.

The coupling of this model with Virtual Reality (VR) or Augmented Reality (AR) technology is a useful tool for multiple applications. The direct usage of this tool is to strategically design wind farms while accounting for the detailed knowledge of the noise generated beforehand and also bridges communication between

citizens and local authorities. The model can also be used for the application of the psychoacoustic analysis. With the control of individual physical parameters, the impact of wind turbine noise on sleep and annoyance can be studied in detail [24]. The study in this direction can possibly link the psychoacoustic impact to the characteristics of wind turbine noise.

1.3 Objectives and outline of the thesis

We precise the objectives that we desire to achieve in this thesis:

- Develop a frequency-domain model for the prediction of the wind turbine noise.
- Propose a synthesis tool to convert the frequency-domain information into a time-signal.
- Validate the model against field measurements.

To the aim of attaining a physics-based synthesis model for wind turbine noise we avail of the source model developed previously by Tian and Cotté [89] to obtain frequency-domain spectra of the predicted noise in free field. In Chapter 2, the components of the frequency-domain model are revised with certain advancements based on recent literature. To account for the propagation effects associated with the wind speed gradient and ground reflection, the use of the wide-angle Parabolic Equation in moving medium [70] is explained in Chapter 2. The scattering due to atmospheric turbulence is included using the Harmonoise model are studied. In Chapter 3, the development of the synthesis tool to obtain a time signal from the frequency-domain model is explained in detail. Finally, in Chapter 4, the model predictions are compared to field measurements to investigate the limitations and validity of the model. The state of the art of each component of the developed wind turbine noise synthesis model is described in the respective section. We give some concluding remarks in Chapter 5 about the model that is developed along with a few perspectives.

2

Modelling of aeroacoustic sources and atmospheric propagation in the context of wind turbines

Contents

2.1 Introduction

The noise generated from the blades of a wind turbine can be viewed as moving sound sources in an outdoor environment. As shown in Figure 2.1, the blade is

usually divided into a set of segments that correspond to acoustic point sources. Assuming these segments can be modeled as rotating monopoles as in Cotté (2019), the sound pressure level at a far-field receiver can be calculated using:

$$SPL(\omega, \gamma) = SPL_{\mathrm{FF}}(\omega, \gamma) + \Delta L(\omega, \gamma) - \alpha_{\mathrm{abs}}(\omega) R(\gamma), \tag{2.1}$$

where SPL_{FF} (dB) is the sound pressure level observed at the receiver position in free-field, ΔL (dB) is the sound pressure level relative to free field, α_{abs} (dB/m) is the atmospheric absorption coefficient [84], R (m) is the direct distance between the point source and the receiver, ω is the angular frequency and γ is the angular position of the segment. SPL_{FF} is characteristic of the source considering geometric spreading and while $(\Delta L - \alpha_{\mathrm{abs}} R)$ includes the effects observed due to propagation of the sound through the atmosphere.

The source part of the wind turbine noise corresponds to all the aeroacoustic mechanisms that are responsible for the generation of the noise from the blades which can be categorised as trailing edge noise (TEN), turbulent inflow noise (TIN), stall noise or other such generated noise. Stall noise occurs only at high angles of attack and so only TEN and TIN are observed at all times. Section 2.2 explains the state

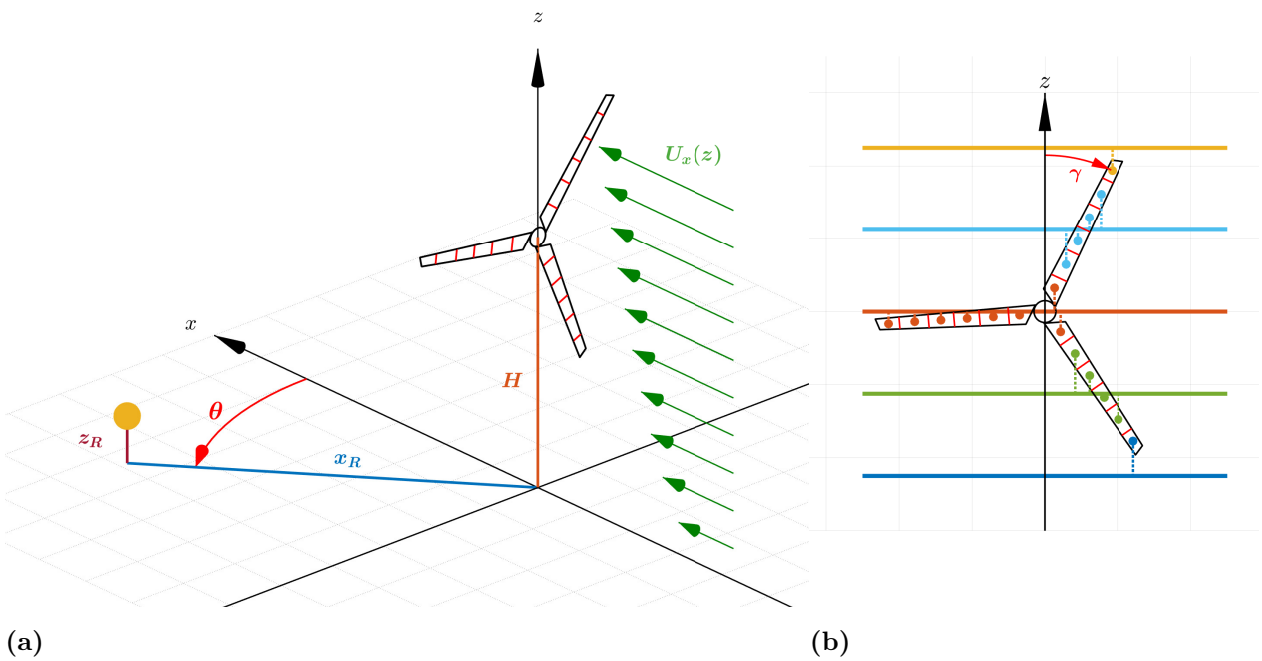

(a) (b)

Figure 2.1: Schematics for (a) the wind turbine modelled with the receiver represented as a sphere. (b) the segmented blade in motion represented a set of point sources where the required heights for the propagation effect is distributed to the nearest-neighbouring height between five heights represented as different colors.

of the art of the wind turbine source modeling, and details the frequency-domain model used in this study. This model is an extension of the one proposed by Tian and Cotté [89] based on Amiet's theory.

The propagation part of the wind turbine noise system corresponds to how the noise generated at the source is modified as it propagates through the atmosphere. The propagation effects correspond to the refraction due to the wind speed gradient, the interference patterns caused by the ground reflection, scattering due to turbulence, etc. In Section 2.3 previous models used for the study of outdoor noise are presented, and the model based on the parabolic equation in moving medium used in this work is explained. We finally give a few concluding remarks on the developed wind turbine noise model in Section 2.4.

2.2 Source model

2.2.1 Existing models for wind turbine noise aerodynamic sources

Several wind turbine noise source models have been proposed in the literature that are themselves based on a few aerodynamic noise prediction models. The most widely used models for the prediction of the aerodynamic noise sources are the one of Brooks *et al.* [15], also known as BPM model and the models of Amiet for trailing edge noise and turbulent inflow noise [2, 3]. The BPM model named after the three developers, is a semi-empirical model based on extensive measurement data of a NACA 0012 airfoil. Using this model, certain wind turbine noise models have been developed such as by Zhu *et al.* [99] and Oerlemans *et al.*[63] with some success. However, as the model is based on the data of the NACA 0012 airfoil which is not representative of a realistic wind turbine, it is difficult to assess its validity.

Amiet [2] derived a statistical model to predict the noise generated by the leading edge of an airfoil when subjected to a turbulent gust by using Schwartzschild's solution and Curle's [21] far-field acoustic solutions. The model assumes a homogeneous and isotropic turbulent inflow which can be modelled with the von Kármán spectrum. Later, Amiet [3] extended the model to predict the noise that is generated by the trailing edge of an airfoil. For the prediction of TEN, the information of the wall pressure fluctuation at the trailing edge of the airfoil is necessary. The wall-pressure spectrum used by Amiet is an empirical formulation based on the data of Willmarth and Roos [96]. The original models of Amiet or modifications of them have been used extensively in the development of the wind turbine noise models

such as the ones of Glegg *et al.* [33], Tian and Cotté [89]. It has to be mentioned that the Howe's model [40] is also used for the prediction of the trailing edge noise in the far field. The TEN can be modeled using Amiet's model or Howe's model as both account for the diffraction effects by assimilating the airfoil as a flat plate. Furthermore, both models need the wall pressure spectrum as an input. This can be obtained using semi-empirical models [34, 81, 49], TNO-Blake models [87, 46, 26]. The input parameters of the semi-empirical models and TNO-Blake models can be obtained by panel methods (Xfoil) or Reynolds-averaged Navier–Stokes (RANS) simulations [39]. Note that empirical models have also been proposed for stall noise [10] and have been implemented recently in a wind turbine noise model [100].

The frequency-domain model of wind turbine noise developed by Tian and Cotté [89], uses the model of Amiet to predict the noise from the leading edge and trailing edge of the blades. The blades of the wind turbine are divided in segments corresponding to individually sources that contribute to the total noise in the far field (Fig. 2.1a). The segmentation of the blade is done ensuring the segment span is greater than the spanwise correlation length so that the individual contribution of the segments can be summed in an incoherent manner at the receiver. The rotation of the blade is included by assuming the blade moving through a discrete number of angular position γ (Fig. 2.1b). The Doppler effect and convective amplification observed due to the rotation of the blades are accounted for in the frequency domain following Sinayoko *et al.* [86] by:

$$S_{pp}(\mathbf{x_0}, \omega) = \left(\frac{\omega_e}{\omega}\right) S^{\mathrm{N}}_{pp}(\mathbf{x}, \omega_e), \tag{2.2}$$

where $S_{pp}(\mathbf{x_0}, \omega)$ and $S^{\mathrm{N}}_{pp}(\mathbf{x}, \omega_e)$ is the PSD of the TEN or TIN for a blade in motion and for a fixed blade correspondingly, ω_e and ω are the emitted and observed angular frequencies, $\mathbf{x_0}$ and $\mathbf{x}$ are the observer coordinates in the hub (stationary frame) and blade (moving frame) coordinate systems. The power spectral density S_{pp} of the TEN and TIN are thus calculated for each segment of the wind turbine blades at each discrete angular position. The noise in free field is thus predicted for the receiver at the position defined by (x_R, z_R, θ), where x_R is the distance of the receiver from the base of the hub, z_R is the receiver height and θ is the orientation of the receiver with respect to the wind direction (Fig. 2.1a).

For the calculation of TEN, as different boundary layer conditions are observed for the upper (suction) side and the bottom (pressure) side, the model uses a different wall pressure spectrum (WPS) for each. (See Fig. 2.2) Rozenberg's model is used for the WPS on the suction side while Goody's model is used for the WPS on

the pressure side of the airfoil. Rozenberg's model is valid for an adverse pressure gradient flow while Goody's model has been derived for a zero pressure gradient flow which is a flat plate with zero incidence. The calculation of TIN is done using the von Kármán spectrum and also accounting for the airfoil thickness correction. The thickness correction is done using an empirical correction formulation that is based on the data of Roger and Moreau [80].

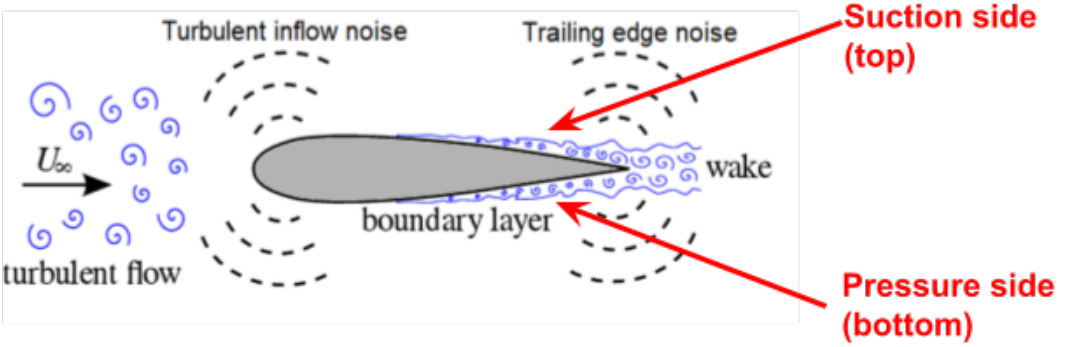

Figure 2.2: Schematic showing suction side and pressure side of the airfoil (adapted from Gea-Aguilera [29]).

We closely follow this model proposed by Tian and Cotté [89] and revisit a few components of the model, specifically the WPS that influences the TEN and the turbulence spectra that influences the TIN. We discuss the WPS semi-empirical models in Section 2.2.2 and the replacement of the von Kármán spectrum with the Kolmogorov spectrum in Section 2.2.3. Amiet's theory for the TEN and TIN is valid for a large span to chord aspect ratio which restricts us to use a relatively small number of blade segments. Using the inverse strip theory [18], the large aspect ratio requirement is not needed anymore and the influence of the number of blade segments on the noise predictions can be investigated. Finally the modification of the directivity of the airfoil is addressed in Section 2.2.5, based on the suggestion of Oerlemans *et al.* [63].

2.2.2 Trailing edge noise theory based on semi-empirical wall pressure spectral models

2.2.2.1 Fixed airfoil

The turbulent boundary layer fluctuations convected along the airfoil surface at a velocity U_c interact with the trailing edge to generate broadband noise, as shown schematically in Figure 2.3. The Power spectral density (PSD) of trailing edge noise

observed at a far-field receiver (x, y, z) by an airfoil with large span L to chord c aspect ratio ($L > 3c$) is given by [3, 80]:

$$S_{pp}{}^{\text{TEN}}(x, y, z, \omega) = \left(\frac{kcz}{4\pi S_0^2}\right)^2 2L\Phi_{pp}(\omega) l_y\left(\omega, \frac{ky}{S_0}\right)\left|\mathcal{L}_{TE}\left(x, \frac{\omega}{U_c}, \frac{ky}{S_0}\right)\right|^2, \tag{2.3}$$

where k is the acoustic wavenumber, $S_0 = \sqrt{x^2 + \beta_0^2(y^2 + z^2)}$ is the modified distance between the source and the observer with $\beta_0 = \sqrt{1 - M^2}$, M is the Mach number of the inflow gust, Φ_{pp} is the wall pressure fluctuation spectrum (WPS), l_y is the spanwise coherence length estimated by the Corcos model and $\mathcal{L}_{TE}$ is the transfer function for trailing edge noise.

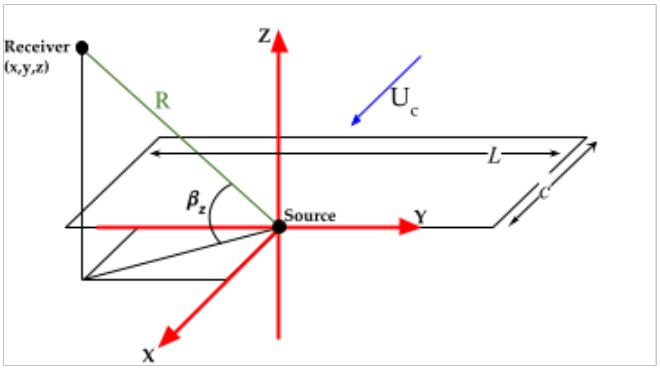

Figure 2.3: 3D geometry showing the position of the receiver with respect to the plane of the airfoil.

The estimation of Φ_{pp} is a key element for accurately predicting the far-field SPL generated by the airfoil. Amiet [3] originally suggested an empirical model for Φ_{pp} is based on scaling the experimental data of Willmarth and Roos' [96] by the boundary-layer displacement thickness δ^*. The model does not accurately predict the WPS in the high frequency range as the small scales in the boundary layer are not well represented by δ^*. Goody [34] proposed an improved model with a few more variables that captures the values of the WPS at higher frequency given by:

$$\frac{\Phi_{pp}(\omega)U_e}{\tau_w^2\delta} = \frac{3.0(\omega\delta/U_e)^2}{[(\omega\delta/U_e)^{0.75} + 0.5]^{3.7} + [1.1R_T^{-0.57}(\omega\delta/U_e)^7]}, \tag{2.4}$$

where U_e is the velocity at the boundary-layer edge, τ_w is the wall shear stress, δ is the boundary-layer thickness and $R_T = (\delta/U_e)/(\nu/u_*^2)$ is the ratio of the outer to inner boundary layer time scales with ν the kinematic viscosity and u_* the friction velocity.

The model given by Goody captures well the WPS for a fully developed turbulent boundary layer when the zero pressure gradient flow condition is fulfilled. However, this condition is usually not fulfilled on a real airfoil as an adverse pressure gradient is usually present on the suction side close to the trailing edge, while a favorable pressure gradient may be present on the pressure side. To account for the adverse pressure gradient effect observed, Rozenberg *et al.* [81] proposed a WPS given as:

$$\frac{\Phi_{pp}(\omega)U_e}{\tau_{max}^2\delta^*} = \frac{\mathbf{a}\ \ (\omega\delta^*/U_e)^2}{[4.76(\omega\delta^*/U_e)^{0.75}+d]^e + [8.8R_T^{-0.57}(\omega\delta^*/U_e)]^h}, \tag{2.5}$$

where $\mathbf{a} = [2.82\Delta^2(6.13\Delta^{-0.75}+d)^e][4.2(\Pi/\Delta)+1]$, τ_{max} is the maximum shear stress along the normal distance, $\Delta = \delta/\delta^*$ is the Zagarola and Smits's parameter, $\Pi = 0.8(\beta_c+0.5)^{3/4}$ is the wake strength parameter with β_c the Clauser's parameter, $d = 4.76(1.4/\Delta)^{0.75}[0.375e-1]$, $e = (3.7+1.5\beta_c)$ and h = min(3, $19/sqrtR_T$)+7.

In Ref. [89], the wall pressure fluctuation spectrum Φ_{pp} is calculated using Goody's model for the pressure side and Rozenberg's model for the suction side of the airfoil. However, based on Rozenberg's model Lee recently developed a new empirical model for zero- and nonzero-pressure gradient flows [49, 50]. The model is said to handle higher pressure gradient flows on an airfoil and zero-pressure gradient flows on a flat plate. The non-dimensional form of the WPS of Lee's model is:

$$\frac{\Phi_{pp}(\omega)U_e}{\tau_w^2\delta^*} = \frac{\max(\mathbf{a},(0.25\beta_c-0.52)\mathbf{a})\ \ (\omega\delta^*/U_e)^2}{[4.76(\omega\delta^*/U_e)^{0.75}+d^*]^e + [8.8R_T^{-0.57}(\omega\delta^*/U_e)]^{h^*}}, \tag{2.6}$$

where $\mathbf{a} = [2.82\Delta^2(6.13\Delta^{-0.75}+d)^e][4.2(\Pi/\Delta)+1]$ and the wall shear stress τ_w is calculated by $\tau_w = (1/2)(\rho U_e^2 C_f)$ with C_f the friction coefficient. For this model, the absolute values of the pressure gradient are taken in β_c for favourable pressure gradient flows, which often occur on the pressure side (PS) near the trailing edge. The parameters h^* and d^* are defined as follows:

$$h^* = \min(3,(0.139+3.1043\beta_c))+7 \tag{2.7}$$

$$d^* = \begin{cases} 0 & \text{if } \beta_c < 0.5 \\ d & \text{otherwise} \end{cases} \tag{2.8}$$

It should be noted that Eq. (2.6) is not validated for strong adverse pressure gradients (high values of $\beta_c > 50$) as the flow becomes highly separated after this. For

moderate pressure gradients (β_c between roughly 1 and 6), Lee's model is identical to Rozenberg's model. The results start to deviate only for small pressure gradients and for strong adverse pressure gradients.

It is suggested that the model of Lee can be applied for the suction side and also the pressure side. As Goody's model has been previously used for the zero pressure gradient on the pressure side and Rozenberg's model for adverse pressure gradient on the suction side for a wind turbine model [89], we compare these models to that of Lee to see if there is an improvement in the obtained results. The models for the WPS by Goody [34], Rozenberg [81] and Lee [49] are single-sided and are multiplied by 2π to obtain $\Phi_{pp}(f)$. The obtained WPS and the corresponding far-field noise obtained by these models are compared to the experimental data for the airfoils NACA 0012 and NACA 64-418 at zero angle of attack that have been previously studied in the literature [81, 46]. Due to the symmetry of the NACA 0012 airfoil, the prediction of the WPS for the suction side and pressure side is the same at zero angle of attack. On the other hand, the wall pressure spectra on the suction and pressure sides are different for the NACA 64-418 airfoil that is cambered so each contribution is calculated separately. The relation between the single-sided PSD of the acoustic pressure (S_{pp}) and the far-field sound pressure level (L_p) is given by[46]:

$$L_p(f) = 10 \log_{10} \left[\frac{S_{pp}(f) df}{p_{ref}^2} \right], \tag{2.9}$$

with $p_{ref} = 2 \times 10^{-5}$Pa the reference pressure and df is the frequency spacing of 1 Hz. The far-field SPL is the incoherent sum of the contributions from the suction side and the pressure side of the airfoil. The boundary layer parameters obtained from the literature for the calculation of the WPS are given in Table 2.1. It has to be noted here that in the literature there are only a few cases that have experimental data of the WPS and SPL for the same flow conditions. This is the case for the NACA 0012, but not for the NACA64-418 as will be seen in the following.

For the NACA 0012 airfoil, the boundary layer parameters given in Table 2.1 are used to calculate the WPS and the corresponding far-field SPL. The far-field SPL for this airfoil is calculated by Amiet's theory based on the parameters listed in Table 2.3. The calculated WPS and the predicted far-field SPL are compared to experimental data in Fig. 2.4.

To compare the results for the NACA 64-418 airfoil with the experimental data [46, 50], the boundary layer parameters for the WPS are extracted from XFoil [46] and are given in Table 2.2. Measurements have been performed both with clean

Airfoil type		x/c	Boundary layer parameters						
			U_e (m/s),	δ (m),	δ^* (m),	θ (m),	τ_w (Pa),	β_c	Π
NACA 0012	S/PS C	0.97	64.6	0.0142	0.00236	0.00157	5.43	3.51	2.267
	SS T	0.99	67.5	0.018107	0.005612	0.00294	2.4509	12.91	5.61
NACA	PS T	0.99	67.5	0.014782	0.003019	0.001957	5.7486	2.19	1.68
64-418	SS C	0.99	67.5	0.010097	0.002677	0.001590	3.9680	5.31	3
	PS C	0.99	67.5	0.008841	0.001566	0.001108	7.4908	0.54	0.82

Table 2.1: Boundary layer parameters calculated at x/c of the airfoil at zero incidence which are used for the WPS of NACA-0012 [15, 81] and NACA 64-418 airfoils [46, 45] (C= clean, T=tripped at 0.05).

Airfoil type		x/c	Boundary layer parameters					
			U_e (m/s),	δ (m),	δ^* (m),	θ (m),	β_c	C_f
	SS T	0.99	62.08	0.0204	0.0055	0.0029	15.6240	0.0007
NACA	PS T	0.99	60.32	0.0165	0.0030	0.002	-6.7481	0.0016
64-418	SS C	0.99	61.45	0.0115	0.0026	0.0016	7.9118	0.0013
	PS C	0.99	58.87	0.0097	0.0016	0.0011	-3.316	0.0020

Table 2.2: Boundary layer parameters calculated at x/c with XFoil of NACA 64-418 airfoil at zero incidence that are used for the WPS to predict the far-field SPL (C= clean, T=tripped at 0.05).

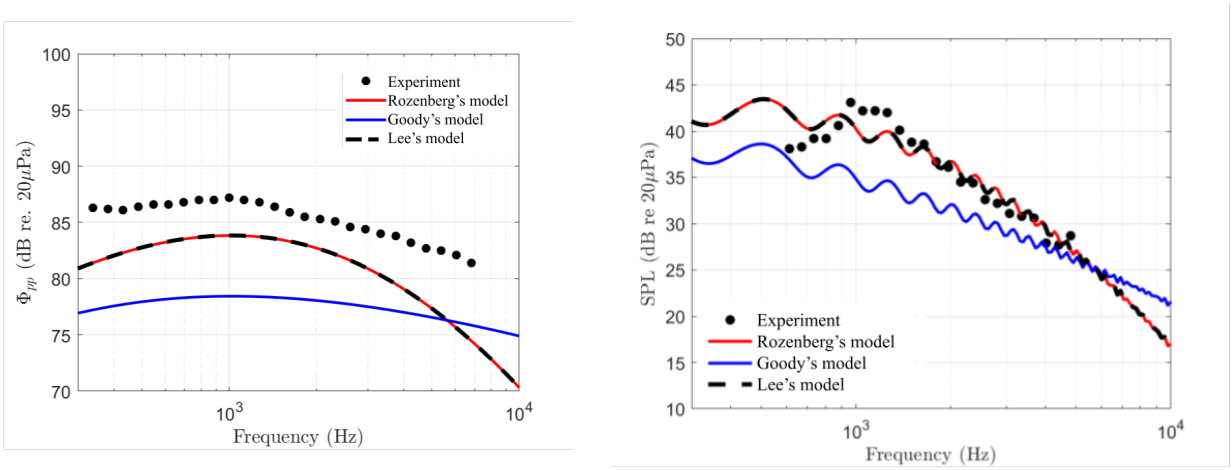

Figure 2.4: Experimental WPS (left) and far-field SPL at 1.2 m upstream(right) compared to Lee's model, Rozenberg's and Goody's model for NACA0012

Airfoil type	Span (m),	Chord (m),	**z** (m),	U_{inflow} (m/s),	ρ_0 (kg/m^3),	$\nu/10^5$ (m^2/s)
NACA 0012	0.46	0.61	1.2	69.5	1.29	1.45
NACA 64-418	1	0.6	1	70	1.2	1.46

Table 2.3: Parameters used for far-field noise prediction of NACA-0012 [15, 81] and NACA 64-418 airfoils [46]. The position of the microphone is perpendicular to the inflow direction at a distance **z** from the mid-span point of the trailing edge.

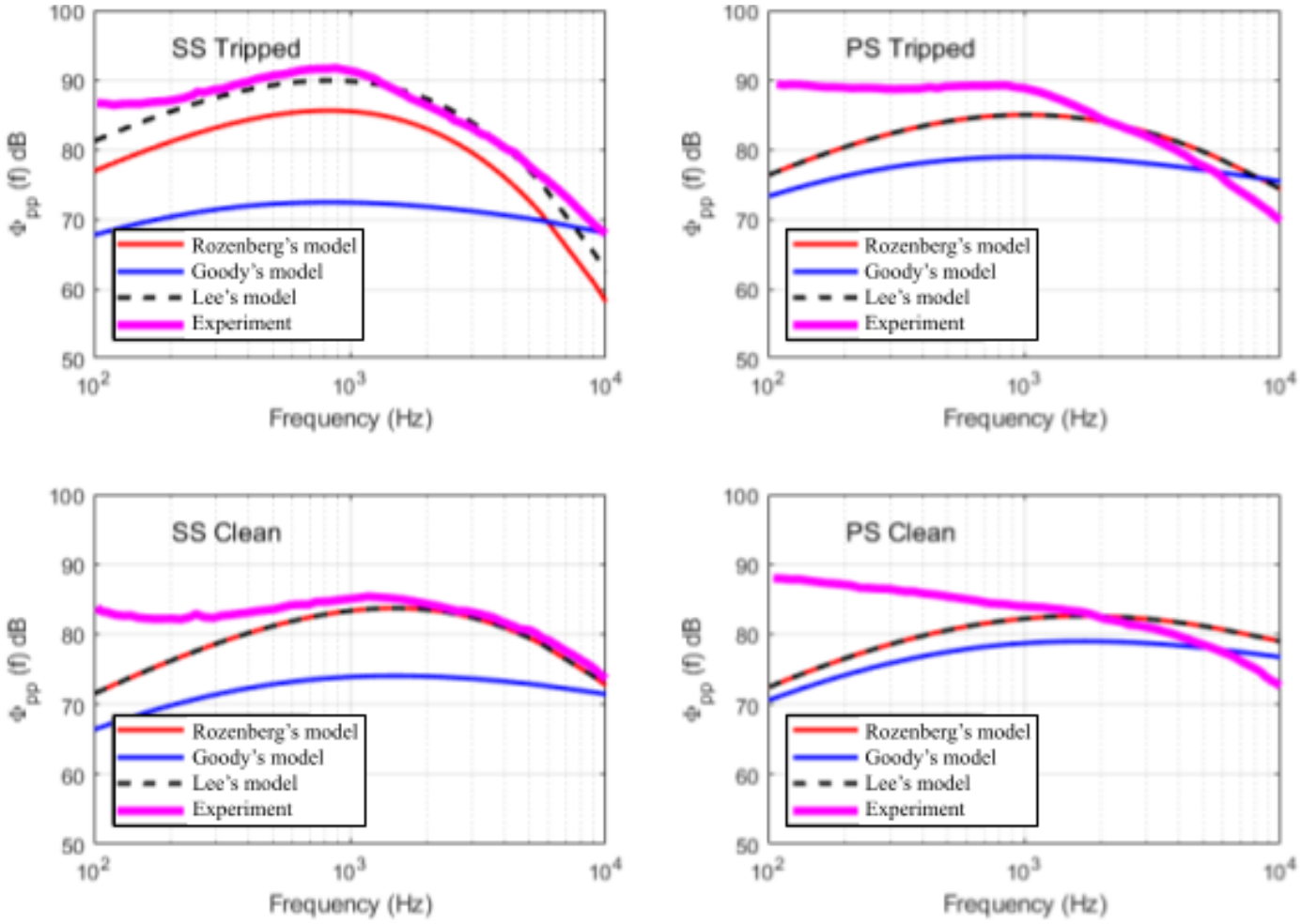

Figure 2.5: Experimental WPS compared to Lee's model, Rozenberg's and Goody's model for a NACA 64-418 airfoil, using the parameters given in Table. 2.1.

and tripped airfoils. The use of a tripping tape at x/c=5% enables one to force the laminar-turbulent transition of the boundary layer, which ensures that the boundary layer is fully turbulent at the trailing edge. The results of the calculated WPS are compared to the experimental data in Fig. 2.5. The parameters given in Table 2.3 are used with the boundary layer parameter listed in Table 2.2 to compute the far-field SPL that is compared to the experimental data in Fig. 2.6. For consistency with the literature in reference the far-field SPL for the NACA 64-418 airfoil is calculated by Howe's theory [46, 50].

It can be seen from Fig. 2.4, that the prediction of the WPS and the predicted far-field SPL for NACA 0012 is the same with Lee's model and Rozenberg's model, since Clauser parameter is equal to 3.51. The predicted far-field SPL using either model is the same and both are close to the experimental data. For the test case with NACA 64-418, the WPS calculated for the suction side and the pressure side

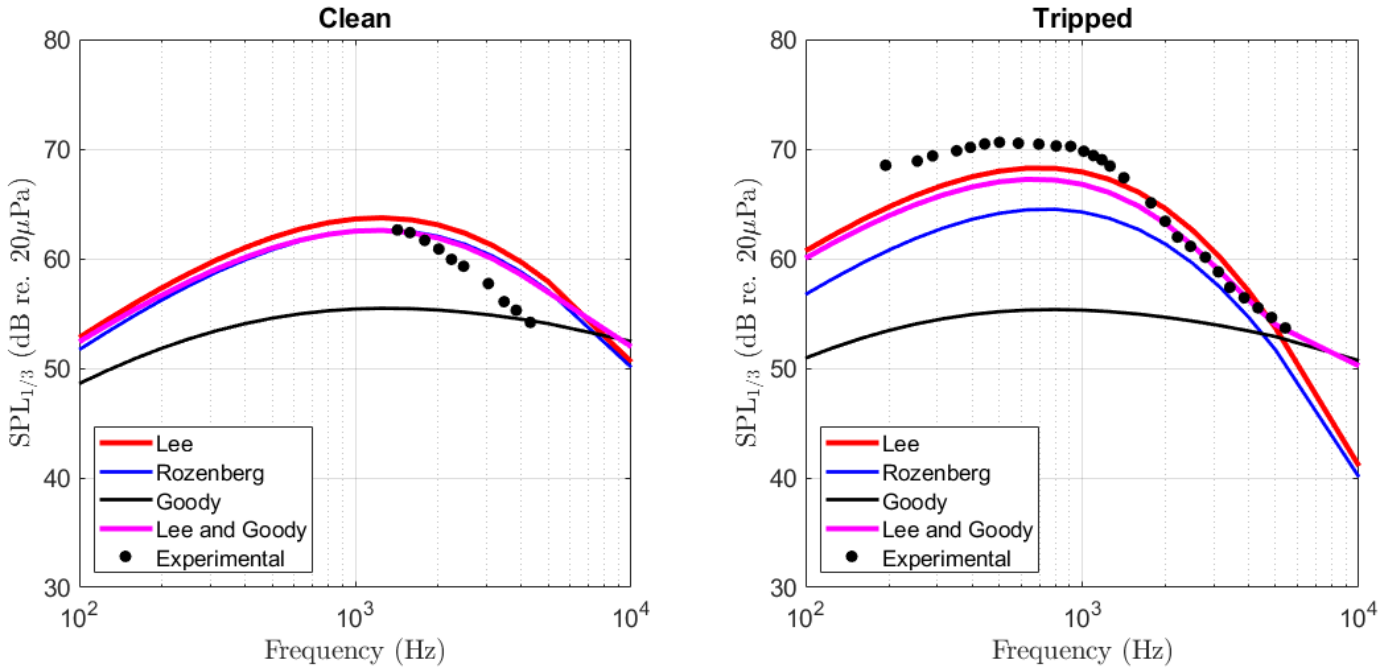

Figure 2.6: Experimental far-field SPL compared to the predicted noise with Lee's model, Rozenberg's and Goody's model of the WPS for NACA64-418

are different for the clean and tripped transitions (Fig 2.5). Here the model of Lee is closer to the experimental data only for the case when the suction side is tripped. This case corresponds to the highest value of the Clauser's parameter β_c, as can be seen in Table 2.1. For the rest of the cases Lee's model is exactly the same as Rozenberg's model within the frequencies of interest. The WPS prediction of Lee's model is better for the suction side than for the pressure side. On the pressure side, none of the models follow the measured spectrum very well. This can be due to the fact that the pressure gradient varies rapidly close to the trailing edge with this airfoil, which means that the boundary layer is not at equilibrium. To our best knowledge, there is no accepted WPS model for favorable pressure gradient flows ($dp/dx < 0$). The far-field SPL is computed with the WPS for the suction side and the pressure side for the respective transitions. The predicted far-field SPL for the tripped airfoil are closer to the experimental data compared to the clean airfoil as can be seen in Fig.2.6. It is known that Rozenberg's model is better at predicting the WPS for the suction side while Goody's model predicts the WPS better for the pressure side. Computing the far-field SPL using Lee's model on both sides does not yield a better result than using Rozenberg's model for the suction side and Goody's model for the pressure side.

2.2.2.2 Rotating airfoil

The model of Lee is applied and validated for a specific range of β_c and Re_θ [49, 50], beyond which this empirical model may not be accurate. For zero pressure gradient flows, the calibrated range for the momentum-thickness-based Reynolds number $Re_\theta = \theta U_e/\nu$ is $1.4 \times 10^3 \leq Re_\theta \leq 2.34 \times 10^4$, and for adverse pressure gradient flows, the calibrated range is $0.5 \times 10^3 \leq Re_\theta \leq 1.65 \times 10^4$. The minimum and maximum values of the Clauser's parameter β_c are -0.343 and 28.57 respectively. To apply Lee's model for the simulation of the full-sized wind turbine [89], the calculated parameters β_c and Re_θ must be within the validated range. Following Tian and Cotté [89], the blade of length 45m is divided into 8 segments, and a NACA 64-415 is used for all segments. The boundary layer parameters for the airfoil NACA 64-415 are calculated using XFoil at x/c = 0.99 for different angles of attack and various inflow speeds. The parameters β_c and Re_θ obtained from this calculation for a complete rotation are obtained with a constant wind speed of 8 m/s and plotted in Fig. 2.7 and Fig. 2.8 for the suction and pressure sides. In these figures, segment 1 is the closest to the hub, with the smallest angular velocity, and segment 8 is the last one with the highest angular velocity.

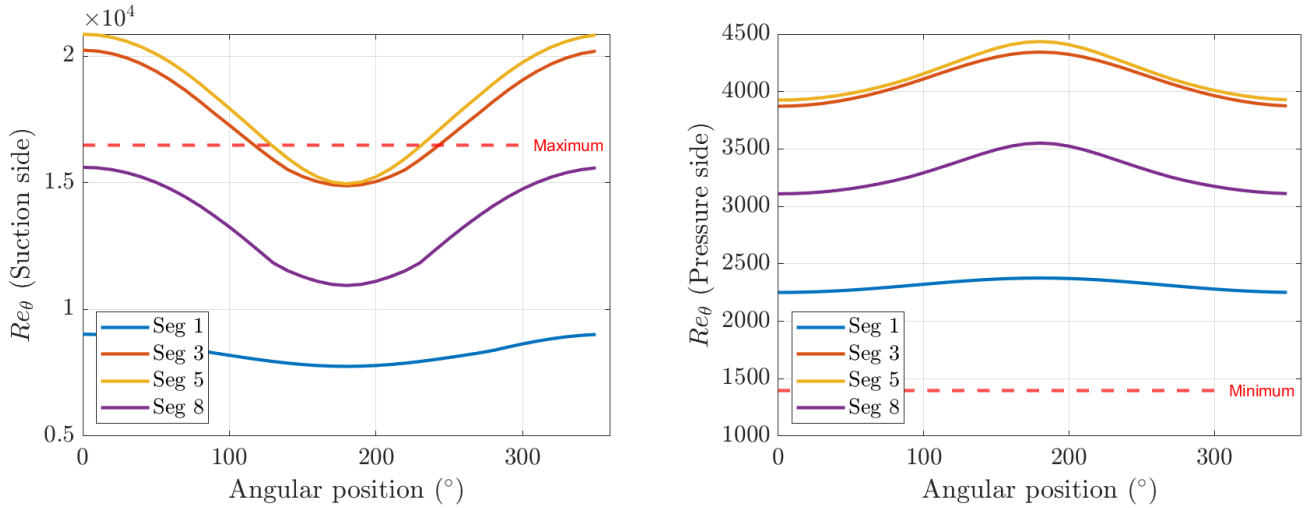

Figure 2.7: The momentum-thickness-based Reynolds number Re_θ for different segments in rotation calculated using XFoil at x/c = 0.99

From Fig. 2.7, it is clear that the condition for Re_θ is not satisfied for certain angular positions of the blade on the suction side, whereas the condition is well satisfied on the pressure side. In Fig. 2.8 it is seen that β_c on the suction side is within the validated range for all angular positions, but a strong favorable pressure gradient is obtained on the pressure side, which is not accounted for in Goody or Lee's models. The literature does not show experimentally validated cases for the

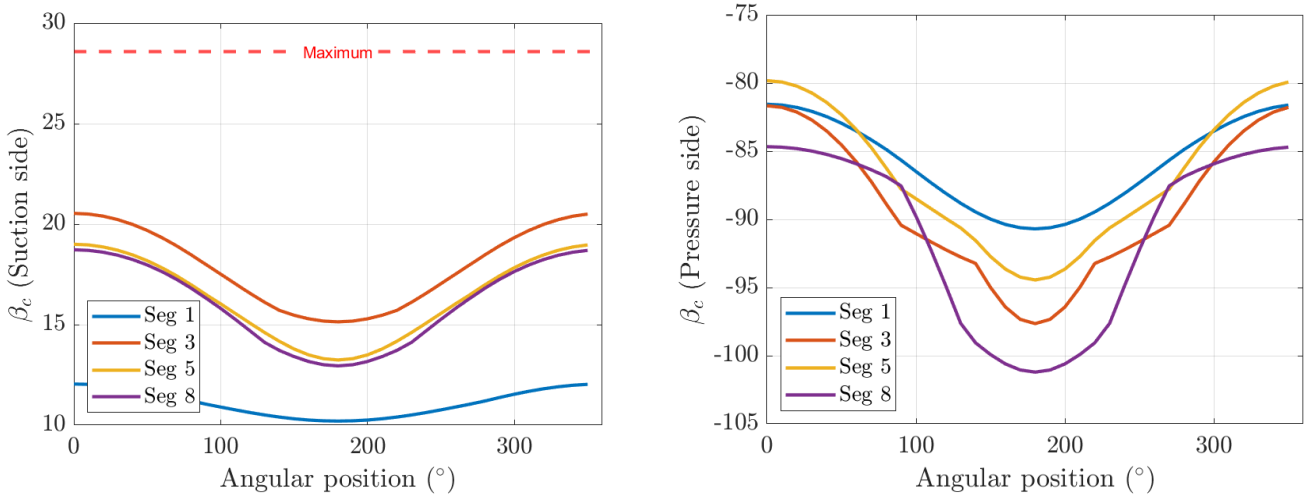

Figure 2.8: The Clauser's parameter β_c for different segments in rotation calculated using Xfoil at x/c=0.99 (Condition: maximum β_c is 28.57)

favourable gradient condition for any model of the WPS. The only validated cases on the pressure side are with a pressure gradient equal to zero or close to zero. Lee's model has been validated on a limited number of configurations on the pressure side, that is why we choose in the following to keep Goody's model as in the original model of Tian and Cotté. On the suction side, Lee's model is used as it provides a better estimate of the WPS for strong adverse pressure gradients, as shown in the previous section. Even though the values of Re_θ for a full-size wind turbine exceed slightly the validation limit, we expect the predictions to remain reasonable as the WPS does not vary drastically when Re_θ increases (Fig. 6 of [49]).

2.2.3 Turbulent inflow noise based on Kolmogorov spectrum

Using Amiet's theory, the radiated acoustic pressure power spectral density (PSD) of a large-aspect-ratio airfoil subject to a turbulent flow with velocity U_0 is given by [2, 80]:

$$S_{pp}^{\mathrm{TIN}}(x,y,z,\omega) = \left(\frac{\rho_0 kcz}{2S_0^2}\right)^2 \pi U_0 \frac{L}{2} \Phi_{ww}\left(\frac{\omega}{U_0}, \frac{ky}{S_0}\right) \left|\mathcal{L}_{\mathcal{TI}}\left(x, \frac{\omega}{U_0}, \frac{ky}{S_0}\right)\right|^2, \qquad (2.10)$$

where ρ_0 is the air density, Φ_{ww} is the 2D energy spectrum of the vertical velocity fluctuations and $\mathcal{L}_{\mathcal{TI}}$ is the aeroacoustic transfer function. Using the von Kármán model for the energy spectrum Φ_{ww}, a homogeneous and isotropic turbulence [2] is given by:

$$\Phi_{ww}(k_1, k_2) = \frac{4}{9\pi} \frac{u'^2}{k_e^2} \frac{k_1^2/k_e^2 + k_2^2/k_e^2}{(1 + k_1^2/k_e^2 + k_2^2/k_e^2)^{7/3}}, \tag{2.11}$$

where u' is the rms axial velocity fluctuations, k_1 and k_2 are the turbulent wavenumbers in the chordwise and spanwise directions and k_e is the wavenumber corresponding to the turbulence outer scale: $k_e = \sqrt{\pi}\Gamma(5/6)/[\Lambda\Gamma(1/3)]$ where Γ is the Gamma function and Λ is the turbulence integral length scale.

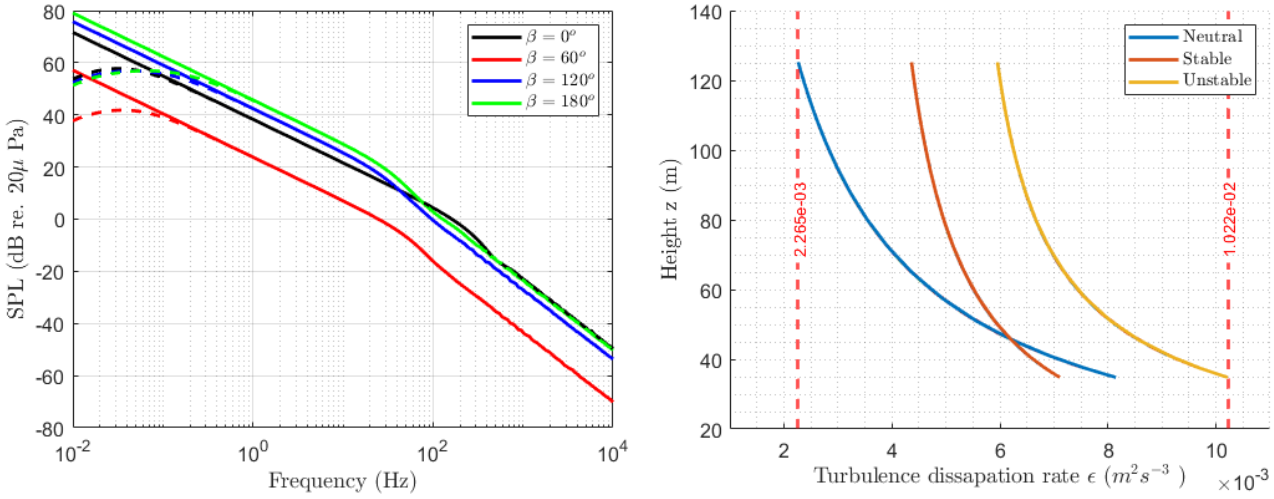

(a) **(b)**

Figure 2.9: (a) The far-field SPL of the TIN computed with the von Kármán spectrum (dashed) and Kolmogorov spectrum (solid) for different angular position of the wind turbine blade. (b) The turbulent dissipation rate ϵ for different atmospheric stability conditions based on Monin-Obukhov Similarity Theory [27]. The vertical lines correspond to the extreme values that have been measured in Ref. [60]

Since the turbulent length scales in the energetic range lie outside the range of interest for acoustic applications, we implement a Kolmogorov spectrum that corresponds to the high frequency asymptote of the von Kármán spectrum:

$$\Phi_{ww}(k_1, k_2) = \frac{4}{9\pi}(k_1^2 + k_2^2)^{-4/3} \quad u'^2 k_e^{2/3}. \tag{2.12}$$

Using the relation given by Buck *et al.* (Eq. 7 of [17]):

$$\Lambda^{-2/3} u'^2 = C_K \epsilon^{2/3} \frac{9\pi^{1/6}}{55} \left(\frac{\Gamma(1/3)}{\Gamma(5/6)}\right)^{5/3},$$

with $C_K \approx 2.0$ is the Kolmogorov constant [68, 17] and ϵ is the turbulence dissipation rate (TDR). The turbulence spectrum is now described as a Kolmogorov spectrum

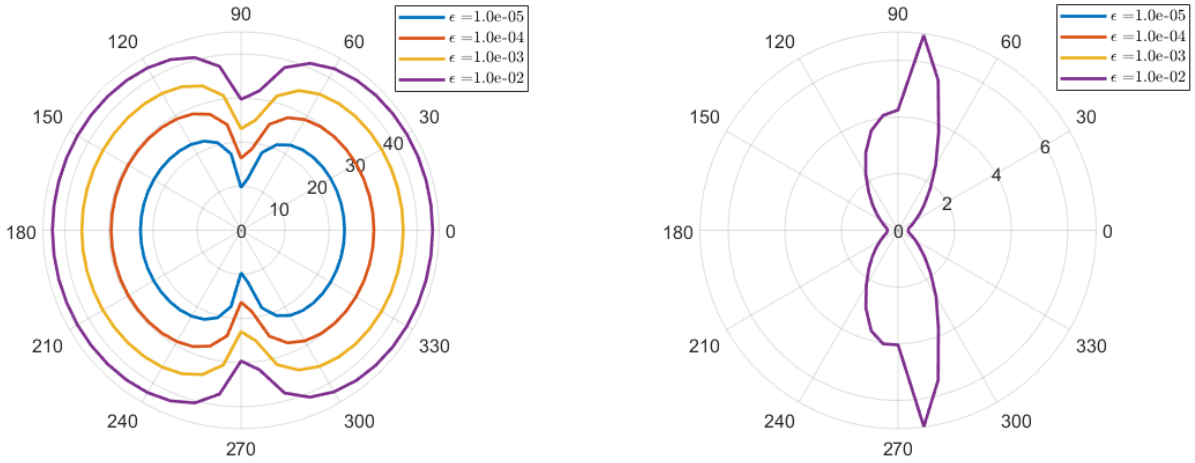

(a) **(b)**

Figure 2.10: Polar plots of (a) OASPL (dB) and the (b) AM strength (dB) of the TIN obtained with constant wind speed of 8 m/s with no wind shear and $\Omega = 14rpm$ for different turbulent dissipation rates. The radial coordinate showing the level in dB and the azimuthal showing the angle with respect to the wind direction i.e. 0° is downwind.

as:

$$\Phi_{ww}(k_1, k_2) = \frac{4}{55\sqrt{\pi}} \frac{\Gamma(1/3)}{\Gamma(5/6)} \; C_K \epsilon^{2/3} \; (k_1^2 + k_2^2)^{-4/3}. \tag{2.13}$$

The main input parameters for the von Kármán spectrum are the rms axial velocity fluctuation u' and the turbulence integral length scale Λ. The integral length scale requires long intervals (30 minutes or more) to be properly estimated from sonic anemometer measurements [17, 67]. On the contrary, the turbulence dissipation rate ϵ can be reliably calculated within a 15 s sonic anemometer measurement [17]. Using the Kolmogorv spectrum in place of the von Kármán spectra also reduces the input parameter from two to one.

For a receiver at the cross-wind position at a distance of 100 m from the base of the wind turbine with hub height of 80 m, the far-field SPL for the TIN is calculated using Eq. (2.9) and Eq. (2.10) for one complete rotation. The turbulence parameters are extracted from the Monin-Obukhov Similarity Theory for a neutral atmosphere using a reference wind speed of 8 m/s at hub height of 80 m. Fig. 2.9a shows the difference between the far-field SPL calculated with the Kolmogorov spectrum (solid lines) and the von Kármán spectrum (dashed lines). It is seen that there is a difference between the two spectra only below 1 Hz. From Fig. 2.9b it can be seen that the calculated turbulence dissipation rate ϵ for various atmospheres based on

the Monin-Obukhov Similarity Theory, lies within the expected range for a turbulent atmosphere taken from Ref. [60] and shown as vertical lines in the figure.

The same system as mentioned above is considered with the receiver at the cross-wind position but now with a constant turbulence dissipation rate for every height. Munoz-Esparza *et al.* have indeed shown that the turbulence dissipation rate is relatively constant above a height of 50m, and the Monin-Obukhov Similarity Theory is known to be only valid close to the ground. The effect of the turbulence dissipation rate ϵ on the prediction of the far-field noise in terms of the OASPL and the amplitude modulation depth (AM) for the TIN can be seen in Fig. 2.10. This effect of ϵ on the TIN is significant with a difference of around 7 dB for the change of one order of magnitude of ϵ. From Eq. (2.10) and Eq. (2.13), we can see that the S_{pp}^{TIN} is proportional to $\epsilon^{2/3}$ and thus the corresponds to $6.67 \log_{10} \epsilon$ (dB). The range of the turbulent dissipation rate values in Fig. 2.10 is chosen as the expected extremities for a stable atmospheric condition [60].

2.2.4 Inverse Strip theory

The equation for PSD of the turbulent inflow noise observed in the far field is based on the large aspect ratio approximation. The general formulation of the PSD from an airfoil with the span L and chord c that is placed in a turbulent flow of mean velocity U_0 in the chordwise direction is given by Amiet's theory as [2]:

$$S_{pp}^{TIN}(x, y, z, \omega) = \left(\frac{\rho_0 \omega c z}{2 c_0 S_0^2}\right)^2 \pi U_0 \frac{L}{2} \int_{-\infty}^{\infty} \frac{\sin^2[L/2(k_y - K_y)]}{\pi L/2(k_y - K_y)^2} |\mathcal{L}_{\mathcal{TI}}(\mathbf{x}, k_x, k_y)|^2 \Phi_{ww}(k_x, k_y) \mathrm{d}k_y, \tag{2.14}$$

where $K_y = (\omega y / c_0 S_0)$ is the radiating spanwise aerodynamic wave number and $k_x = (\omega / U_0)$ is the chordwise aerodynamic wave number. As the semi-span $L/2$ increases, the cardinal sine function tends to a delta function,

$$\lim_{d \to \infty} \left(\frac{sin^2[L/2(k_y - K_y)]}{\pi L/2(k_y - K_y)^2} \right) = \delta(K_y - k_y). \tag{2.15}$$

which reduces Eq. (2.14) the Eq. (2.10).

Christophe *et al.* [18] showed that the PSD calculated directly for a single large aspect-ratio airfoil by Eq. (2.10) is not equivalent to the summed strips of the airfoil calculated by Eq. (2.14). The difference between the PSD calculated directly for a large span airfoil and the PSD of the summed strips is due to the contribution

of Φ_{ww}, $\mathcal{L}_{\mathcal{TI}}$ and the cardinal sine function that is influenced by k_y.

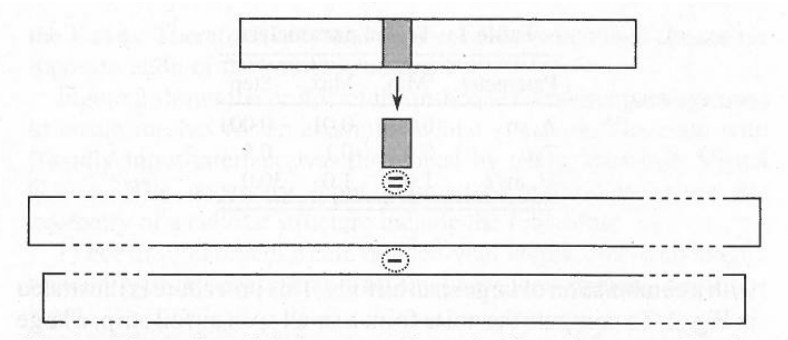

Figure 2.11: Illustration of the inverse method strip showing that the contribution of a small segment can be obtained from the contributions of two large aspect ratio airfoils [18].

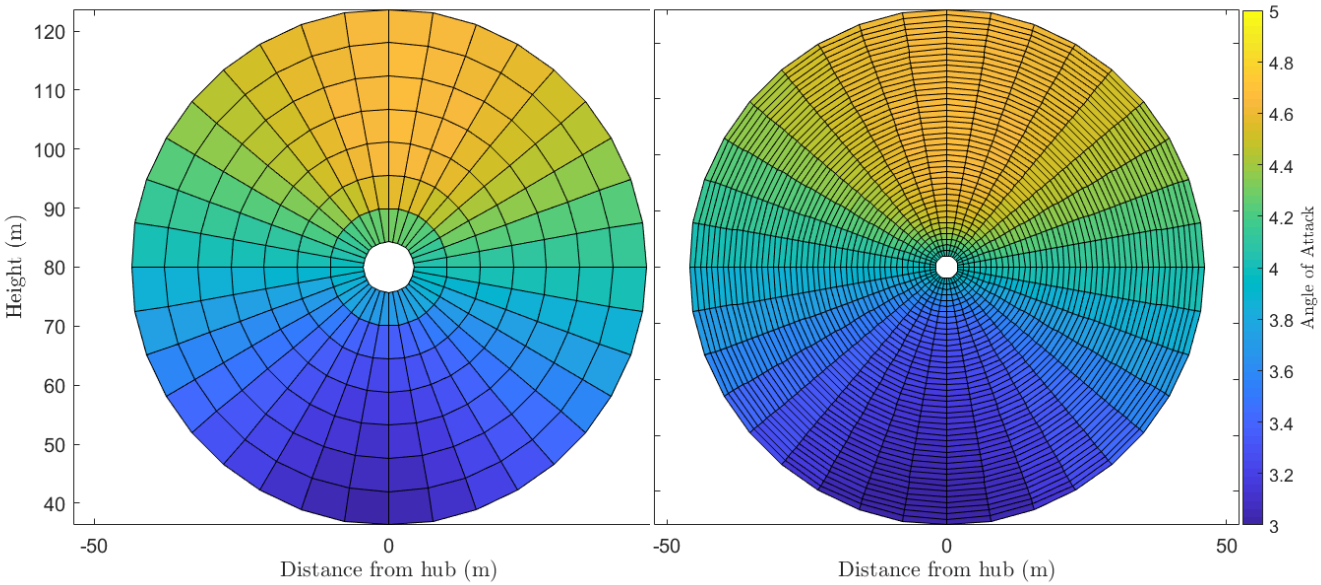

(a) **(b)**

Figure 2.12: The angle of attack experienced for each segment of a full-sized wind turbine. Each blade of the wind turbine is divided into (a) 8 segments, (b) 45 segments.

To capture the influence of the large aerodynamic wavelengths for the small spans, Christophe *et al.* [18] proposed the inverse strip method. The main assumption is that the small-span airfoil is a section of a large aspect airfoil (Fig. 2.11). This procedure is to compute the noise from a large span airfoil from which is subtracted the same large span airfoil truncated by the considered small span strip (viz. $S_{pp}^{(d)} = S_{pp}^{(\infty)} - S_{pp}^{(\infty-d)}$). As the considered airfoil is large, Eq. (2.10) can be used directly for the calculation of the two large airfoils. This method captures the

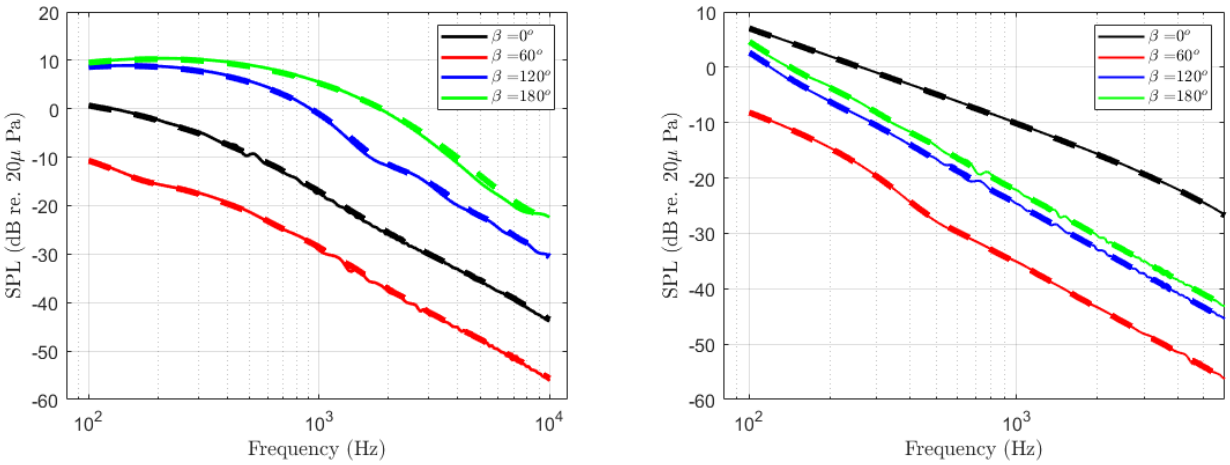

Figure 2.13: The difference between the noise predicted using 8 segments (Solid) and 45 segments (Dashed) for the (a) trailing edge noise and (b) turbulent inflow noise.

influence of the lower frequencies and is computationally efficient, as the PSD is calculated directly from Eq. (2.10) and not from Eq. (2.14).

For the large span, in Eq. (2.10), $\Phi_{ww}(k_x, K_y)$, $\mathcal{L}(\mathbf{x}, k_x, K_y)$ are independent of the span L. The other terms are constant for a single airfoil with span L. The PSD S_{pp} can thus be calculated for an airfoil of unit length span and then scaled to the required chord length L. Similarly, the inverse strip theory can also be applied for the calculation of the trailing edge noise.

The TIN and TEN from the full-sized wind turbine are initially predicted with the blades divided into 8 segments, where each segment observes the large-aspect ratio condition. The inverse strip method is applied to obtain a large number of segments with greater resolution of the flow over each part of the blade. A power law wind profile is applied with shear exponent of 0.2 and reference wind speed U_{ref}= 8 m/s at the hub height of z_{ref}= 80 m. A constant Kolmogorov spectrum with ϵ= $5{\times}10^{-3}m^2s^{-3}$ is applied for all heights. The wind turbine blade of 45 m length is divided into 8 segments and 45 segments for comparison. Fig. 2.12 shows the angles of attack that are experienced by each segment of the wind turbine blade in rotation for 8 segments and 45 segments. The TEN and TIN are calculated for a receiver at the cross-wind condition at a distance of 100 m from the base of the hub. Fig. 2.13 shows the difference between the predicted far-field noise of the full-sized wind turbine by dividing the blade into 8 segments and 45 segments. It can be seen that the difference between the two systems is negligible. This means that dividing

the blade into 8 segments is sufficient. However, if the effect of a complicated wind profile on the noise is to be studied, it could be necessary to increase the number of segments to accurately predict the effect of span-wise varying conditions.

If the correlation length l_y of each segment is smaller than the segment span, we can assume that the predicted far-field noise produced by adjacent segments are uncorrelated. The correlation length for the TEN is calculated using the Corcos model as:

$$l_y^{TEN}(\omega, K_y) = \frac{\omega/(b_c U_c)}{K_y^2 + \omega^2/(b_c U_c)^2} \tag{2.16}$$

where b_c is a constant determined experimentally and K_y is the span-wise turbulence wavenumber. With $K_y = 0$ (mid-span plane), Eq. (2.16) reduces to:

$$l_y^{TEN}(\omega) = \frac{b_c U_c}{\omega}. \tag{2.17}$$

Several values are proposed that relate the convective velocity to the inflow velocity. For our purpose, we take $U_c = 0.7U_0$ and b_c= 1.47 [81]. To calculate the maximum limit of the correlation length for the simulation of the wind turbine noise, we consider the extreme values of the input variables. For the frequency of 50 Hz, rotational speed $\Omega = 2$ rad/s and wind inflow speed U_{inflow}=10m/s, the correlation length is calculated for the entire blade of the wind turbine. The ratio of the correlation length to the respective span length L is plotted in Figure 2.14a for TEN using a 45-m long blade divided into segments of equal length. It can be seen that even with the largest values considered, the segments are always uncorrelated.

For the turbulent inflow noise, the equation for the correlation length with $K_y = 0$ is different and is given by [2]:

$$l_y^{TIN}(\omega) = \frac{8\Lambda}{3}\left[\frac{\Gamma(1/3)}{\Gamma(5/6)}\right]^2 \frac{[\omega/(U_0 K_e)]^2}{(3 + 8[\omega/(U_0 K_e)]^2)\sqrt{1 + [\omega/(U_0 K_e)]^2}} \tag{2.18}$$

where $K_e = (\sqrt{\pi}/\Lambda)(\Gamma(5/6)/\Gamma(1/3))$ is the wavenumber corresponding to the turbulence length scale. Considering only the high frequency asymptote of Eq. (2.18) the correlation length for the TIN is now based on the Kolmogorov spectrum:

$$l_y^{TIN}(\omega) = 1.4\frac{U_0}{\omega}. \tag{2.19}$$

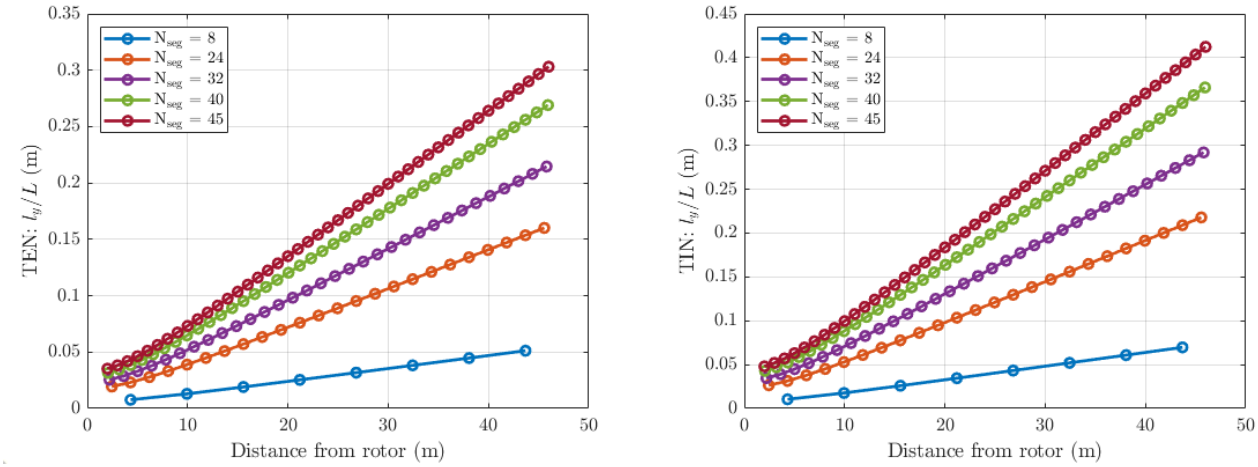

(a) **(b)**

Figure 2.14: The correlation length calculated for a wind turbine blade of $45m$ length, divided into N_{seg} number of segments for (a) TEN and (b) TIN.

The correlation length for the TIN is calculated for the same blade segmentation as for the TEN and the ratio l_y/L is plotted in Figure 2.14b. Similar to the correlation length of the TEN, it can be seen even with the extreme values considered, the segments are always uncorrelated for the prediction of the TIN.

2.2.5 Directivity

The specific directivity of an individual airfoil plays an important role on the level of the noise depending on the orientation of the receiver. Based on Amiet's theory for TEN and TIN (Eqs. 2.3 and 2.10), the directivity $\mathcal{D}$ of the airfoil noise can be regarded to originate from the aeroacoustic transfer function $\mathcal{L}_T$ for either the trailing edge or the turbulent inflow noise and from z/S_0^2. This directivity can thus be given as:

$$\mathcal{D} = \left(\frac{z \ |\mathcal{L}_T|}{S_0^2} \right)^2 . \tag{2.20}$$

Using this directivity it has been observed that for the receiver in the crosswind positions the interference patterns are under-predicted by more than 8 dB [89, 63]. This underprediction is due to the rapid approach of $\mathcal{D}$ to zero using Amiet's theory when the receiver approaches the plane of the airfoil, $z \to 0$ (Fig. 2.3). Oerlemans *et al.* [63] and Gelot *et al.* [30] suggest to apply a directivity smoothing correction for the airfoil noise prediction to obtain a non-zero value of $\mathcal{D}$ at these positions. The calculated value z in terms of the airfoil coordinates is $z = R \ \sin\beta_z$, where R is

the direct distance between the airfoil edge and the observer and β_z is the elevation angle, as can be seen in Fig. 2.3. The directivity smoothing that is applied by Oerlemans is based on the error function for the values approaching the angles $\beta_z = 0°$ and $\beta_z = 180°$ which seem to give results comparable to the experimental data. In this study, we propose a simpler approach that consists in modifying the term z^2 in the directivity Eq. (2.20) as:

$$z^2 = \mathrm{R}^2 \ (\sin^2 \beta_z + \mathcal{A} \ \cos^2 \beta_z), \tag{2.21}$$

where $\mathcal{A}$ is the correction amount required in percentage. The directivity of the airfoil for two frequencies before and after the correction using $\mathcal{A} = 0.2$ can be seen in Fig. 2.15. It can be seen from Fig. 2.16 that a correction $\mathcal{A}$ of 20% gives approximately the expected difference of 6 dB between the crosswind and the downwind position [63]. This directivity correction will be be validated in Chapter 4 where the physical validation of the model is done.

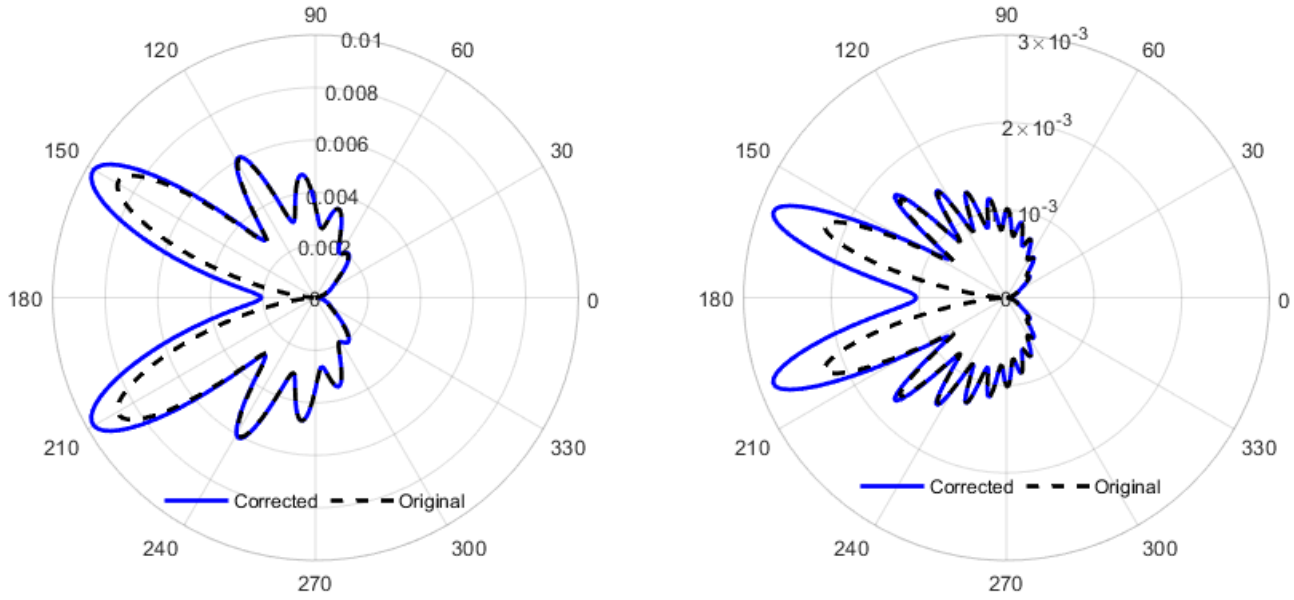

(a) **(b)**

Figure 2.15: The directivity polar plot showing the modified and original directivity of the airfoil for (a) 1000Hz and (b) 2000Hz with $\mathcal{A} = 0.2$.

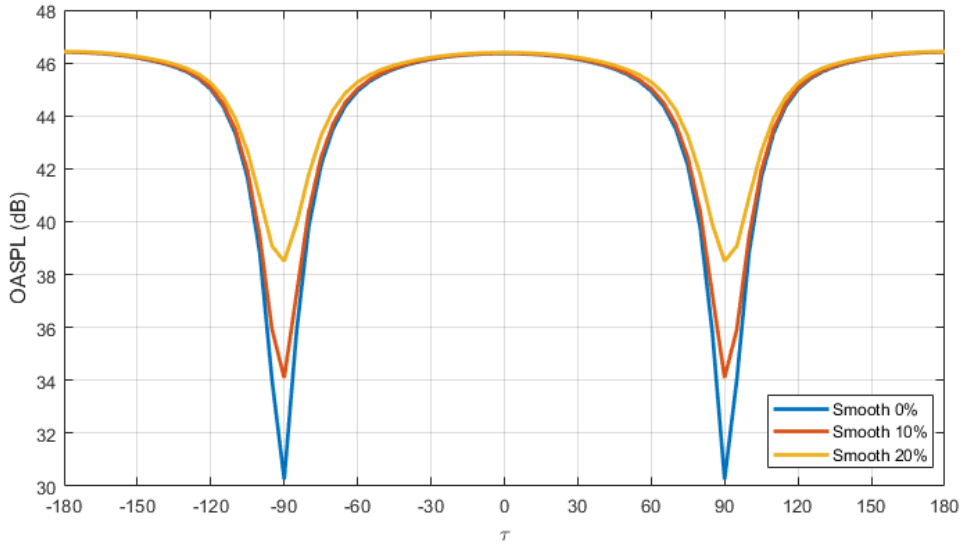

(a)

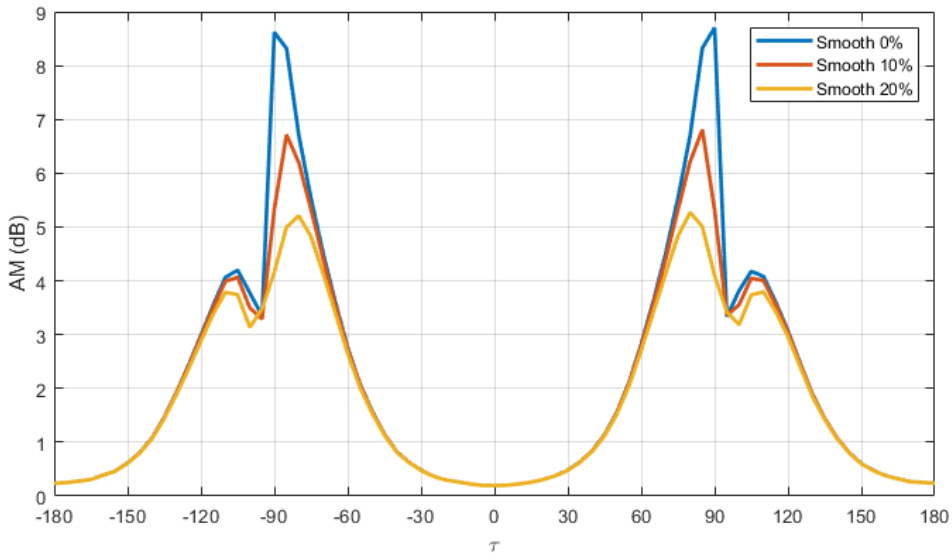

(b)

Figure 2.16: The predicted (a) OASPL and (b) AM for a receiver at $x_R = 100$m for all orientations with different amount of directivity correction $\mathcal{A}$.

2.3 Propagation modelling

2.3.1 Existing models for wind turbine noise propagation

For a simplest case scenario the propagation effects concerning wind turbine noise that exclude the influence of the topography and the effect of the wake of the wind turbine involve refraction due to the wind speed and temperature profiles, ground

reflection off a flat impedance ground, atmospheric absorption and scattering due to turbulence in the atmosphere [84]. The propagation effects can be included in the term $\Delta L - \alpha_{\text{abs}} R$ in Eq. (2.1). The analytical approaches for outdoor sound propagation problems are limited to simple situations such as propagation in a homogeneous and stationary medium or a uniformly moving medium. In realistic scenarios such approaches become insufficient to capture all the effects of propagation. For instance, most ray-based models do not account for the diffraction effects, that are important for instance when an acoustic shadow zone is present. However, the ray-based models have been used for wind turbine noise by McBride *et al.* [56] and Heimann *et al.* [37]. Numerical methods such as Parabolic Equation (PE), linearized Euler equations, Finite and Boundary Element (FEM and BEM) techniques are able to capture most of these effects and have been developed to study the propagation effects in outdoor environments. Finite-Difference Time-Domain solvers have been proposed for the linearized Euler equations but have not yet been implemented to a wind turbine noise system. FEM and BEM techniques are also less common to computer the wind turbine noise propagation effects as they are computationally expensive to solve. The PE approach is particularly favored as it is able to consider both complex topographies as well as meteorological conditions. For the application to wind turbine noise van Renterghem *et al.* [93], Bolin *et al.* [12], Barlas *et al.* [7] as well as Cotté [19, 20] use the PE to compute the propagation effects. However it needs to be noted that van Renterghem *et al.* [93] and Bolin *et al.* [12] model the wind turbine as a point source while Barlas *et al.* [7] and Cotté [19, 20] model the wind turbine as an extended source. Modelling the wind turbine as a point source can be used when only the OASPL is of interest, except for upwind conditions [20]. When the modulation of the noise due to the rotation of the blades is of interest an extended model must be used. The influence of the wake and topography are known to have additional effects on the sound propagation [8, 38] although we neglect these effects here.

The moving monopole approach described by Cotté [20] to study the propagation effects considers multiple source heights and their individual contribution to the receiver in the far field. The model is suggested to work well using the classical parabolic equation (PE) with the influence of the wind speed gradient accounted for using the effective sound speed. However, Ostashev *et al.* [70] shows that this approximation may not be entirely valid for certain conditions and proposes a new formulation that includes the effect of the wind speed gradient directly in the PE model. We study this formulation of Ostashev *et al.* [70] in the context of the moving monopole model [20]. We implement in Section 2.3.2 the parabolic equation

in a moving medium for the effect of the sound refraction and the ground reflection. To account for the effect of scattering due to turbulence we consider an empirical model in Section 2.3.3 to eventually obtain the term ΔL to be used in Eq. (2.1). Finally a few interesting configurations and results are addressed in Section 2.3.4.

2.3.2 Refraction and ground reflection using the parabolic equation in a moving medium

For a sound wave propagating through a medium that is moving with an arbitrary velocity $U_x(z)$, Ostashev *et al.* [70] propose a formulation which can be solved using the Crank-Nicholson (CN) algorithm with a Padé (1,1) approximation. In a two-dimensional vertical plane (x, z), assuming that the air density is a constant equal to ρ_0, Equations (27) and (39) of Ref. [70] for the sound pressure $\hat{p}(x, z)$ and the scaled velocity potential $\hat{\phi}(x, z)$ in the frequency domain reduce to:

$$\hat{p}(x,z) = \left(1 + \frac{iM_x}{k_0}\frac{\partial}{\partial x}\right)\hat{\phi}(x,z), \tag{2.22}$$

$$\left(\frac{\partial}{\partial x} - ik_0\zeta_x^2\sqrt{1+\eta+\hat{\mu}} + ik_0\hat{\tau}\right)\hat{\phi}(x,z) = 0, \tag{2.23}$$

where $M_x = U_x/c_0$ is the Mach number of the moving medium, $k_0 = \omega/c_0$ is the wavenumber associated with the reference sound speed c_0, $\zeta_x^2 = (1 - M_x^2)^{-1}$, $\eta = (c_0/c)^2 - 1$ is the deviation of the refractive index from unity, $\hat{\mu} = \frac{1}{\zeta_x^2 k_0^2}\frac{\partial^2}{\partial z^2}$, and $\hat{\tau} = M_x\zeta_x^2\sqrt{1+\eta}$. Note that some notations are different compared to Ref [70]. For instance η has been used instead of $\hat{x}i$ and ζ_x has been used instead of γ_x. In the absence of flow, $M_x = 0$, $\zeta_x^2 = 1$ and $\hat{\tau} = 0$, thus the classical parabolic equation is retrieved [84]:

$$\left(\frac{\partial}{\partial x} - ik_0\sqrt{1+\eta+\frac{1}{k_0^2}\frac{\partial^2}{\partial z^2}}\right)\hat{p} = 0. \tag{2.24}$$

Using the Padé (1,1) approximation, and introducing the variable $\bar{\phi}$ related to the velocity potential $\hat{\phi}$ by $\hat{\phi}(x,z) = \exp(ik_0x)\bar{\phi}(x,z)$, Eq. (2.23) can be rewritten:

$$\Psi_1(x,z)\frac{\partial\bar{\phi}}{\partial x} = ik_0\Psi_2(x,z)\bar{\phi}, \tag{2.25}$$

where the operators Ψ_1 and Ψ_2 are given by:

$$\Psi_m = h_{m,0} + \frac{h_{m,2}}{k_0^2}\frac{\partial^2}{\partial z^2}, \quad m = 1, 2. \tag{2.26}$$

The coefficients $h_{m,j}$ are written as:

$$h_{1,0} = 1 + b_{1,1}\eta, \qquad h_{1,2} = b_{1,1}/\zeta_x^2,$$
$$h_{2,0} = a_{1,1}\zeta_x^2\eta - (1 + b_{1,1}\eta)\tilde{\tau}, \qquad h_{2,2} = a_{1,1} - b_{1,1}\tilde{\tau}/\zeta_x^2,$$

with $a_{1,1} = 1/2$, $b_{1,1} = 1/4$, and the function $\tilde{\tau}$ is defined as:

$$\tilde{\tau} = M_x\zeta_x^2(\sqrt{1+\eta} - M_x) = \hat{\tau} - M_x^2\zeta_x^2.$$

As in the classical wide-angle parabolic equation, the Crank-Nicholson algorithm can be used to reduce Eq. (2.25) to a matrix system that can be easily solved. The variable $\bar{\phi}$ is discretized using a cartesian mesh of size Δx and Δz: $\phi_m^n = \bar{\phi}(m\Delta x, n\Delta z)$. The domain is bounded by a ground impedance condition at $z = 0$ and by an absorbing layer at the top of the domain. The details are given in Appendix A.

The acoustic pressure $\hat{p}$ can be calculated from ϕ_m^n at $x_m = m\Delta x$ and $z_n = n\Delta z$ using a second-order centered finite difference scheme (Eq. (84) of [70]):

$$\hat{p}(x_m, z_n) = e^{ik_0x_m}\left[(1 - M_x)\phi_m^n + \frac{iM_x}{2k_0\Delta x}\left[\phi_{m+1}^n - \phi_{m-1}^n\right]\right]. \tag{2.27}$$

The two-dimensional sound pressure calculated from this equation is then converted into the three-dimensional relative sound pressure level ΔL_{PE} by dividing by $\sqrt{x}$ and compensating for the direct distance R between the source and the receiver. Thus for a receiver at the position (x_R, z_R) the relative sound pressure level is:

$$\Delta L_{\mathrm{PE}} = 10\log_{10}\left(\frac{|\hat{p}(x_R, z_R)|^2R^2}{x_R}\right), \tag{2.28}$$

where $\hat{p}(x_R, z_R)$ is obtained from Eq. (2.27).

2.3.3 Harmonoise model for turbulence scattering

To consider the effect of scattering due to turbulence, the Harmonoise engineering model [83] is implemented. Note that the Harmonoise model is a complete outdoor sound propagation method, but we only consider the part dedicated to turbulence scattering here. In this model, the total relative sound pressure level is written as:

$$\Delta L = 10\log_{10}(10^{\Delta L_{\mathrm{PE}}/10} + 10^{\Delta L_{\mathrm{scat}}/10}), \tag{2.29}$$

where ΔL_{PE} is the relative sound pressure due to the propagation effects obtained by the WAPE in moving medium in Sec. 2.3.2, and ΔL_{scat} is the sound level that reaches the receiver by scattering due to the turbulent fluctuations of wind speed and temperature in the atmosphere. This term is given by:

$$\Delta L_{\mathrm{scat}} = 25 + 10\log_{10}(\gamma_T) + 3\log_{10}(f/1000) + 10\log_{10}(R/100), \tag{2.30}$$

where f is the frequency of the sound, and γ_T is the turbulence dependent parameter given by:

$$\gamma_T = \left(\frac{C_T}{T_0}\right)^2 + \frac{22}{3}\left(\frac{C_v}{c_0}\right)^2. \tag{2.31}$$

Here, C_v and C_T are the turbulent structure parameters for wind speed and temperature fluctuations respectively and T_0 is the temperature in Kelvin. As shown by Ostashev and Wilson (see Figure 1 of Ref. [69]), the contribution from wind speed fluctuations is at least one order of magnitude higher than the contribution from temperature fluctuations, except in light wind conditions and close to the ground. As a result, the effect of turbulent temperature fluctuations is neglected in the following, and the structure parameter C_v is calculated from the Kolmogorov spectral model for consistency with the source model. Based on the expressions for structure function given in Refs. [68, 60], we obtain:

$$C_v^2 = C_K\ \epsilon^{2/3}. \tag{2.32}$$

Thus the term ΔL_{scat} that accounts for turbulence scattering in the Harmonoise model becomes:

$$\Delta L_{\mathrm{scat}} = 25 + 10\log_{10}\left(\frac{22}{3}\frac{C_K\epsilon^{2/3}}{c_0^2}\right) + 3\log_{10}\frac{f}{1000} + 10\log_{10}\frac{R}{100}. \tag{2.33}$$

2.3.4 Propagation effects in various conditions

2.3.4.1 Configurations studied

In this section, we focus on the propagation effects for the same conditions which are to be tested later in the wind turbine noise synthesis of Section 3.9. To this aim, the WAPE-MM method implemented in this study is calculated for a few source heights z_S between 35 m and 125 m that span the entire rotor height of the wind turbine considered. The wind speed $U_x(z)$ follows a power law profile given by:

$$U_x(z) = U_{ref} \left(\frac{z}{z_{ref}} \right)^{\alpha}, \tag{2.34}$$

where U_{ref} is the reference wind speed at the height z_{ref}. Since the plane of propagation is rotated by an angle θ with respect to the x-z plane (Oxz) as shown in Fig. 2.1a, the effective wind speed profile used in the simulations is $U(z) = U_x(z) \cos\theta$. Different values of the shear exponent α are used between 0.2 (near-neutral atmosphere) and 0.5 (very stable atmosphere) [91].

The ground impedance is calculated via the Miki model [59] for a rigidly-backed layer of thickness e and flow resistivity σ. These ground impedance parameters can be estimated using the method suggested by Guillaume *et al.* [35]. Based on Table 2 of Ref. [35] the parameters for different grounds are summarized in Table 2.4. The two types of grounds are characterized at two different seasons. The difference between summer and winter values reflect the seasonal variations, that are particularly strong for the "Grass" ground. To account for the turbulence in the source model as well as scattering effect, we consider three turbulence levels as shown in Table 2.5. The considered levels correspond to the range of values found in the literature [68, 60].

All calculations of the WAPE-MM model are done with a grid resolution of $\Delta x{=}\Delta z < \lambda/20$, where λ is the wavelength of the propagated sound. The max-

Ground	σ (kNs/m^4)	e(m)
Grass-summer	354	0.0157
Grass-winter	631	0.006
Natural Ground-summer	212	0.0154
Natural Ground-winter	256	0.015

Table 2.4: Different types of grounds in the study

imum height of the grid taken here as 320 m with the absorption layer beginning at 80% of the grid height. A second-order Salomons initial starter at $x_S = 0$ is used at the required source height z_S [84]. A constant temperature profile is set to the reference temperature of 10°C. The same reference temperature is used to calculate the absorption coefficient with the relative humidity of 80%. The number of frequencies equally distributed per third octave band used in the computation is given in Table 2.6.

Level	TDR $\epsilon(m^2/s^3)$	$(C_v/c_0)^2(m^{-2/3})$
Low	0.00054	1.15×10^{-7}
Medium	0.0115	8.81×10^{-7}
Strong	0.177	5.45×10^{-6}

Table 2.5: Parameters of the Miki impedance model for the different types of grounds used in the study.

f_c **(Hz)**	50	100	125	160	200	250	315	400	500	630
N_f	1	1	1	1	2	2	3	4	4	4
f_c **(Hz)**	800	1000	1250	1600	2000	2500	3150	4000	5000	
N_f	5	5	5	6	6	6	7	7	10	

Table 2.6: Number of frequencies N_f per third octave band of center frequency f_c used in the calculations.

2.3.4.2 Results

Fig. 2.17 shows the relative sound pressure level ΔL at 500Hz influenced by the wind flowing in the positive x direction for a receiver upwind ($x < 0$) and downwind ($x > 0$) As the WAPE-MM has an angular validity of 30° [70], the shaded area in Fig. 2.17 shows where the calculation of ΔL is not valid. ΔL is plotted for different wind shear coefficients α, source heights and ground impedance parameter with the effect of turbulence scattering. It can be seen from Fig. 2.17a that the wind shear α increases, the interference dips tend to move closer to the source, and the shadow zone starts generally earlier. For $\alpha = 0$, there is also a good agreement with the analytic solution obtained for a sound in a uniformly moving medium [84, 71]. In Fig. 2.17b the influence of the height of the source can be seen clearly in which the shadow zone for sources closer to the ground starts earlier. Finally in Fig. 2.17c, the change in the ground parameters are more significant upwind rather than downwind. Using the highest turbulence level the relative sound pressure level ΔL is also increased in the interference dips downwind.

Figures 2.18 and 2.19 show the spectrum of ΔL obtained between 100 Hz to 2000 Hz for the source at different heights and a receiver downwind and upwind at a distance of x_R=500m. The results for a grass ground in summer are compared to the results for a grass ground in winter. It can be seen from Fig. 2.18 that the ground impedance parameters modify the level of ΔL and the positioning of the interference patterns. However, this change is more pronounced in the upwind condition as seen from Fig. 2.19. It can be seen that the shadow zone produced is frequency-dependent and the levels in the shadow zone depends on the turbulence levels obtained from the Harmonoise model. The start of the shadow zone calculated for different source heights can be seen in Fig. 2.19 for a receiver at a distance of 500m, in Fig. 2.20a for a receiver at 800m and in Fig. 2.20b at a receiver distance of 1000m. At 500m, the shadow zone appears only for $z_S = 35m$, while it is present for the two lowest source heights at 800m, and for all source heights at 1000m. Fig. 2.20a and 2.20b show that the sound from sources that are higher, which corresponds to the top of the rotor plane, propagate over larger distances. The difference of $\Delta L(f)$ on the basis of the source height is what is experienced by the rotating blade of the wind turbine. It is clear from Fig. 2.17b and Fig. 2.18 to 2.20b that $\Delta L(f)$ cannot be modelled using a single source height and hence requires multiple heights to appropriately account for the propagation effects.

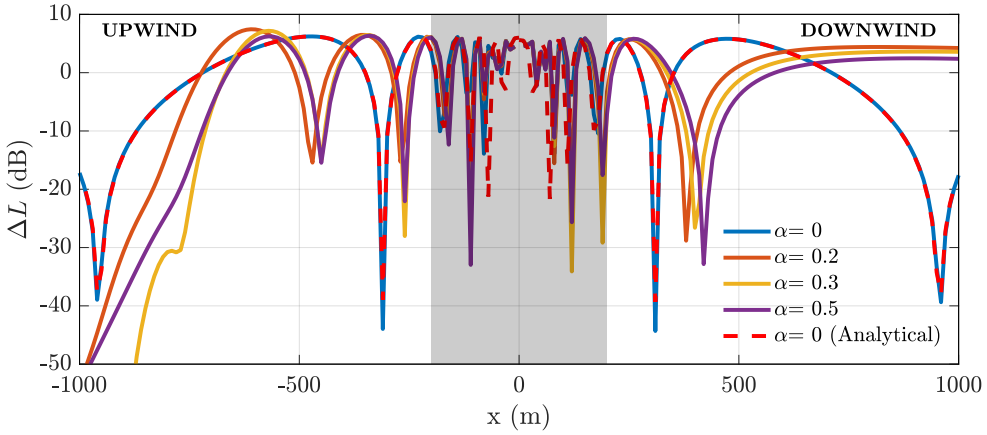

(a)

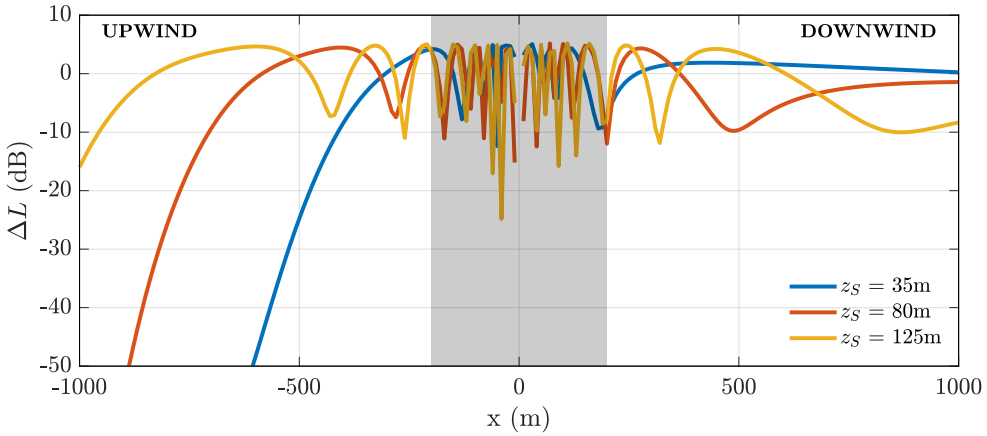

(b)

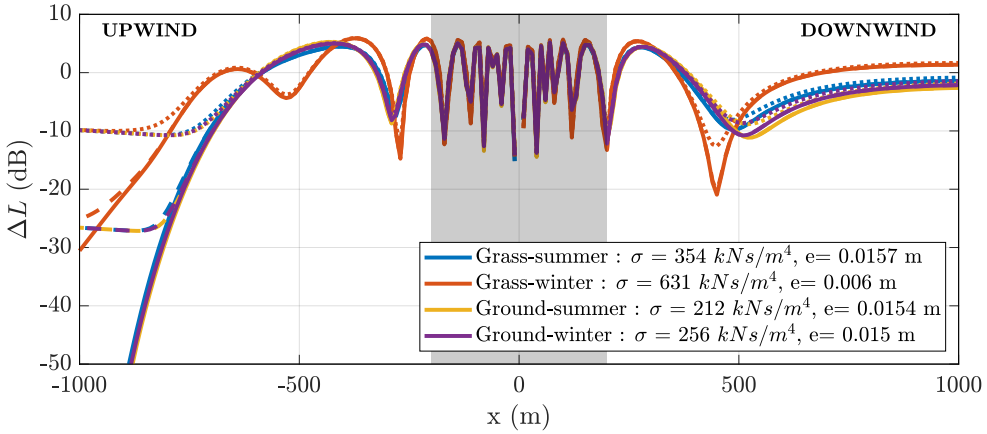

(c)

Figure 2.17: ΔL calculated with f= 500Hz for the receiver at height z_R=2m and x_R upwind (-x) and downwind (+x) with U_{ref}=8m/s at z_{ref}=80m for (a) different wind shear exponents α with the source at z_S=80m and a hard ground with no turbulence in the atmosphere. (b) α=0.3 and with the grass ground in the summer and different source heights with no turbulence in the atmosphere. (c) α=0.3 with the source at z_S=80m and different ground conditions and including turbulence in the atmosphere. (Solid line with no turbulence, dashed line with low turbulence and dotted line with strong turbulence. The shaded area shows where the implemented WAPE-MM is not validated.)

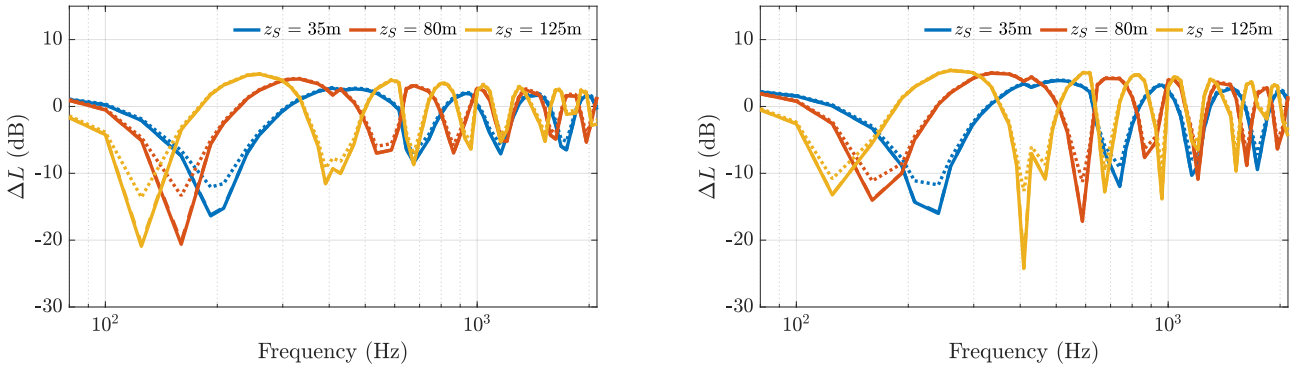

(a) **(b)**

Figure 2.18: ΔL calculated for three different source heights and for a receiver downwind at x_R=500m and z_R=2m with (a) a grass ground in the summer and (b) grass ground in the winter.

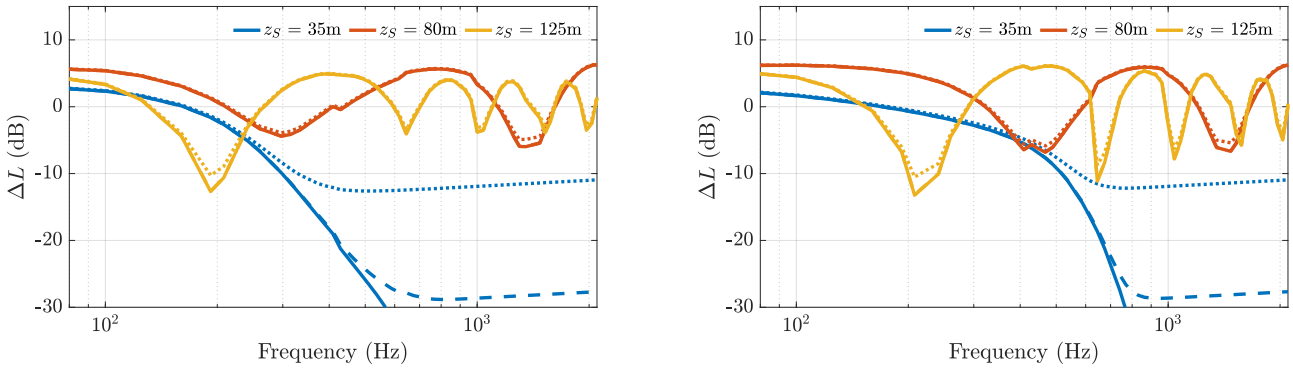

(a) **(b)**

Figure 2.19: ΔL calculated for three different source heights and for a receiver upwind at x_R=500m and z_R=2m with (a) a grass ground in the summer and (b) grass ground in the winter.

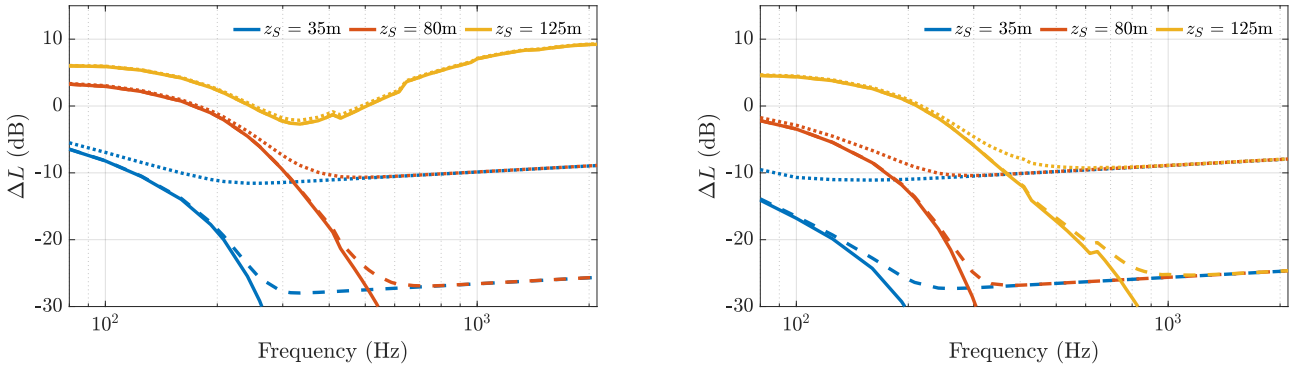

(a) **(b)**

Figure 2.20: ΔL calculated for a grass ground in the summer with various source heights and with a receiver upwind at a height of 2m and distances of (a)x_R=800m (b)x_R=1000m.

2.4 Conclusion

We have achieved a frequency-domain wind turbine noise model that is based on physical models and is also inclusive of the propagation effects such as refraction due to the wind speed gradient, ground reflection and scattering due to the atmospheric turbulence. The source part of the model which depends on Amiet's theory [2, 3], includes a few improvements compared to the original wind turbine noise model of Tian and Cotté [89]. First, the wall pressure spectrum used for the TEN calculation now uses Lee's model for the suction side and Goody's model for the pressure side. Second, the calculation of the TIN is now based on the Kolmogorov turbulence spectrum rather than the von Kármán turbulence spectrum. The Kolmogorov spectrum is favoured for our model as it is dependent only on the turbulence dissipation rate ϵ that is easier to compute from experimental data, as opposed to the von Kármán spectrum which is dependent on two parameters (u', Λ) that are relatively difficult to compute from experimental data. The inverse strip theory is studied to show that eight segments are sufficient to capture the spanwise inflow variations in the noise predictions. The directivity function in Amiet's theory is corrected to avoid an underestimation of the noise levels crosswind.

Compared to previous works by Cotté [19, 20], the effective sound speed approximation is not used and the parabolic equation in moving medium is implemented to accurately capture the refraction effects due to the wind speed profiles. Nevertheless, it is shown by Kayser *et al.* [47] that the difference with the effective sound speed approximation is small for the case of wind turbine noise. The ground impedance is calculated using Miki model for a rigidly backed layer. The ground parameters can be estimated from in situ measurements using a loudspeaker and a pair of microphones. To consider the effect of scattering due to turbulence an empirical model is implemented using the Kolmogorov spectra.

The outcome of the frequency-domain model is the prediction of the TEN and TIN from all the segments of the blade at each angular position. With the help of this frequency-domain model we proceed to synthesize a time-signal of the wind turbine noise. For this we develop a synthesis tool that is detailed in the next chapter.

3

Synthesis tool

Contents

3.1 Introduction

The outcome of the developed wind turbine noise model described in Chapter 2 is a frequency-domain spectrum for a fixed number of segments N_{seg} that move through discrete angular positions γ. We aim to synthesize sounds from this physical model that reflect the change in the input parameters associated with the source and propagation mechanisms. We address the synthesis techniques used by others for wind turbine noise and other outdoor sound sources and describe the synthesis tool that is developed for our model.

3.2 State of the art

The synthesis of outdoor sound propagation can be broadly classified into sample-based synthesis or physics-based synthesis. The sample-based synthesis derives the data from previously recorded signals which are further processed as per the requirement using various filters. Multiple sample-based techniques have been used for the synthesis of outdoor sound sources mostly for road traffic noise [74, 32, 31, 43, 54]. Synthesis of other outdoor noise sources such as railway noise [76, 55] and airplane noise [4, 79] is based on physical parameters which are used to control the synthesis through a series of filters. A few studies have been done for the synthesis of wind turbine noise which are either sample-based or physics-based.

The sample-based auralization done for wind turbine noise by Reto Pieren covers a few characteristics parameters [77, 73] such as the blade passing frequency and broadband noise. The method described by Reto Pieren also includes a characteristic of realistic recordings known as 'stochastic amplitude modulation'. This includes the variation in the signal which may be related to unexpected parameters that can be due to turbulent fluctuations. However, the method does not have any control over the physical parameters of the simulation such as the geometry of the wind turbine, the wind speed, wind direction, orientation of the receiver etc. The method also does not provide insight on the mechanism of the produced sound. A restriction of sample-based wind turbine noise synthesis is that the method is directly dependent on the noise recordings. These recordings are known to be often contaminated with background noise and wind noise [13, 92]. This contamination of the recorded signals makes the analysis difficult and the derived information unreliable.

A similar method proposed by Thorsson [88] is to extract relevant characteristics of the wind turbine noise from a recording and filter pink noise based on the obtained parameters to have a signal. The method is straightforward and is said

to be capable of synthesizing signals with the equivalent spectrum level and desired amplitude modulation which can be tailored to perform subjective listening tests or sleep studies. However, even though this approach is seen to have control over the signal-based parameters such as the spectrum levels and modulation amounts, the method does not connect directly to the physical parameters such as wind turbine geometry, atmospheric conditions etc.

The physics-based synthesis model of Lee *et al.*[51] accounts for the trailing edge noise from the blades directly in the time domain using the Ffocws Williams and Hawkings analogy. The model uses Amiet model to calculate the pressure jump on the airfoil surface and then uses the Ffocws Williams and Hawkings analogy to account for the rotation effects. This model does not include the effects of propagation and is computationally expensive to simulate. Recently, a physics-based approach has been proposed by Bresciani *et al.* [14] for the synthesis of wind turbine noise using a RANS-based Amiet's theory to calculate simulate the leading edge and trailing edge noise contributions. To account for the propagation effects, the Harmonoise ray-based method is used [83]. Julien Maillard [53] describes the implementation of the Doppler effect in this method by an elongation and contraction of the time signal.

3.3 Overview of the synthesis tool

We consider each blade segment as a source which moves along a fixed circle relative to a particular stationary receiver. Our task is to synthesize the wind turbine noise obtained from the model described in Chapter 2, which gives the response of the blade segments at each angular position. We start by showing in Section.3.4 a straightforward method to obtain a time signal from a frequency-domain spectrum for the synthesis of one segment through one single angular transition, as shown in Figure 3.1. The frequency response of each segment for each γ position is synthesized individually and the obtained time signal is termed as a "grain". As the correlation length of the individual auralized grains is assumed to be smaller than the span of the segments, each grain are considered to be uncorrelated and contributes individually to the complete synthesized signal. The grains of all the blade segments are then summed together accounting for the emission time and the appropriate time delay due to the propagation from the segment to the observer.

As the transition between two γ positions are discrete, the synthesized grains placed successively produce artifacts in the form of phase and amplitude discontinuities that can be heard as clicks. Designing a window function for the transitions

between grains with a certain amount of overlap resolves the problem of the generated artifacts. However, the window function has to be designed specifically so as to avoid a change in the overall power which may be caused by the designed window function. As the propagation time is directly dependent on the distance between the source and the receiver, it is different for each grain. This important component is necessary for the reproduction of a realistic auralization and is discussed further in Section 3.5. The influence of the designed window function and the number of grains on the synthesized signals is investigated in Section 3.6. We discuss a signal processing method in Section 3.7 that we use for extrapolating the data beyond the simulated frequency range. Using these elements, the complete synthesis of the wind turbine noise is demonstrated in Section 3.8 and a few test cases of the synthesized signal with different conditions are given in Section 3.9. Finally in Section 3.10, the discussions of the advancements and possibilities of the development of the auralization techniques are presented.

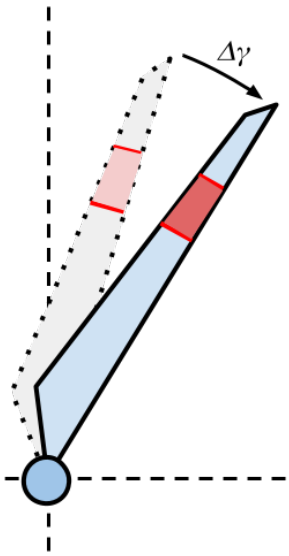

Figure 3.1: Schematic showing a segment passing through one discrete angular transition $\Delta\gamma$. The corresponding synthesized time signal for the transition is called a "grain".

3.4 Conversion from frequency spectra to time-domain signal

To accurately synthesize the frequency response obtained by the model at the correct power level of each individual grain, it is first important to correctly convert

an arbitrary PSD into a time signal. This can be done with the help of the inverse discrete Fourier Transform. The PSD of the acoustic pressure obtained from the frequency-domain model of the airfoil noise is calculated for a set of frequencies between f_{min} and f_{max}. The pressure amplitude corresponding to a particular frequency can be directly calculated as:

$$p(f) = \sqrt{1 \text{ Hz} \cdot S_{pp}(f)} \qquad \text{(Pa)}. \tag{3.1}$$

The spectrum obtained from this equation provides information over a limited number of frequency bins between f_{min} and f_{max}. As the Inverse Discrete Fourier transform (IDFT) converts a frequency-domain spectrum into a time-domain signal while conserving the same number of data points, the number of frequency bins may be insufficient to obtain a time signal of desired length with a typical sampling frequency of 44.1 kHz. To obtain the desired duration of the signal, the amplitude spectrum is interpolated within the frequency range $[f_{min}, f_{max}]$ of the input PSD, while the pressure amplitudes for the other frequencies outside the limits are taken as zero. The number of points of the one-sided spectrum corresponds to the total number of frequency bins that include the interpolated amplitude spectrum and the frequencies with zero amplitude. As the noise is assumed to be stochastic, a random phase with normal distribution between 0 and 2π is assigned to each of the complex amplitudes in this one-sided frequency spectrum. The one-sided frequency spectrum is converted to a symmetric double-sided frequency spectrum, where the spectrum at negative frequencies is the complex conjugate of the spectrum at positive frequencies. Then the IDFT is taken, thus obtaining a real-valued time signal.

Note that considering only the frequencies between [f_{min} and f_{max} is equivalent to a multiplication of the spectrum by a rectangular window. If the phase were constant, this would mean that the inverse Fourier transform of the windowed spectrum involves a sinc function. However, since a random phase is applied to the spectral components, this problem is minimized in our method.

The signal is synthesized for a large time duration (2 seconds) and then truncated as desired. This synthesized signal obtained from the PSD corresponding to one segment is the grain under consideration. A grain synthesized between f_{min}= 100 Hz and f_{max}= 5000 Hz with 18 frequency points that correspond to the center frequencies of the third octave bands shows a good replication of the desired input PSD as seen in Fig. 3.2b. The schematic algorithm of the method is shown in Fig. 3.2a. This method efficiently and accurately synthesises the desired PSD. To avoid edge effects at the start or the end of the signal, it is best to trun-

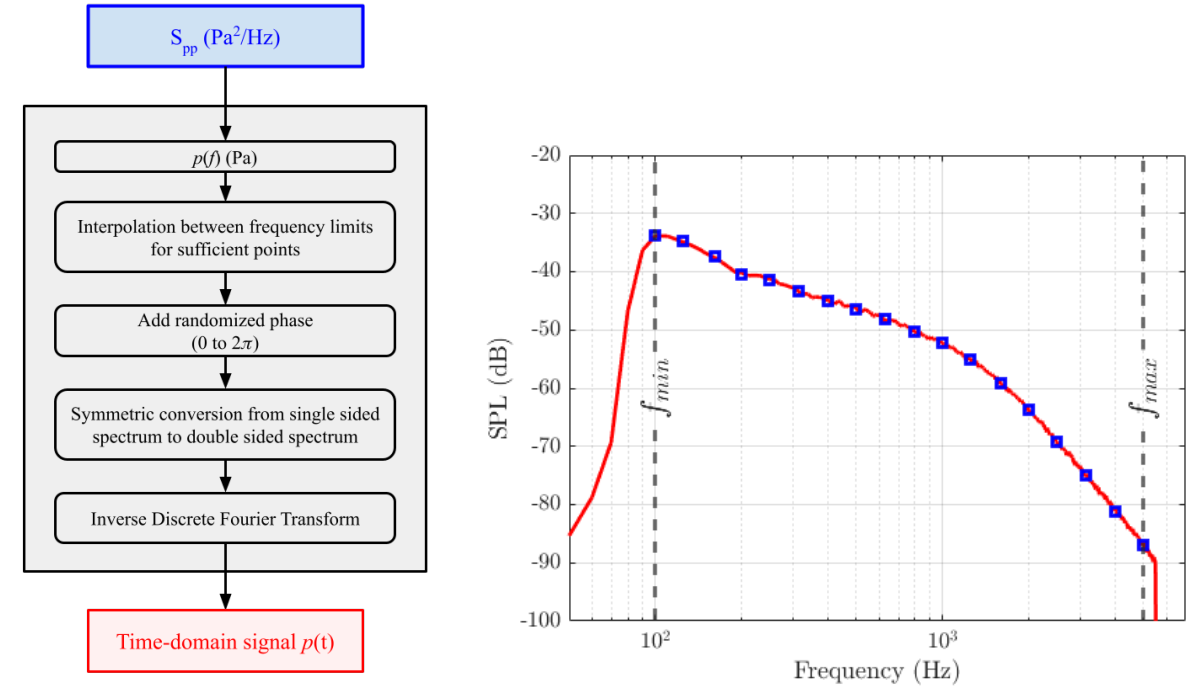

(a) (b)

Figure 3.2: (a) Schematic approach of the method for the conversion of the frequency-domain PSD (blue) to the time-domain signal (red). (b) Plot of the desired input PSD (blue squares) compared to the PSD of the resulting grain with a frequency resolution of 10 Hz (red).

cate certain amount of the signal to the desired length. This method of conversion is applied to each segment at each angular transition and the obtained grains are arranged dependent on their respective propagation time.

3.5 Window function

With the successive allocation of the synthesised grains of the correct size the complete auralization of one blade is thus obtained. However, with the strict successive allocation of the auralized grains it is observed that artifacts are produced in the form of audible clicks during the transition from one grain to another (Fig. 3.3a). This originates from the discontinuity in the pressure from the transition from one grain to another. To avoid this form of artifact, the transition between grains has to be done with a certain amount of overlap to replicate the continuity in the motion of the blade segment. This is achieved by using a windowing function with the desired amount of overlap, while still maintaining the absolute time length and power of each grain.

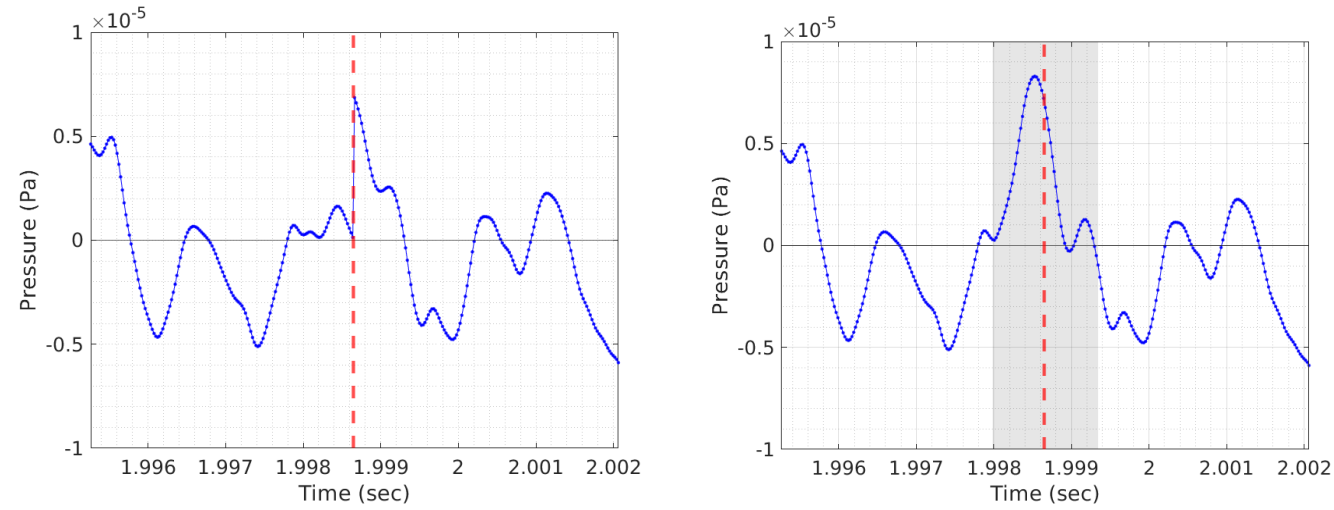

Figure 3.3: (a) Signal without an overlapping window function. Artifacts in the form of clicks are observed at the transition between grains. (b) Signal with an overlapping window function and the artifacts are avoided. The grey shaded area shows the overlap region.

3.5.1 Propagation time and length of the window function

For a segment rotating at a constant speed, the noise emitted through each angular transition has the same duration. However, due to the propagation distance the size of the grains observed at the receiver is different for each grain which needs to be accounted for.

Beginning with the simplest case, a sound emitted at the source at time t_s in a homogeneous medium at rest is observed by the receiver at time t_r following the relation:

$$t_r = t_s + t_p, \tag{3.2}$$

where t_p is the propagation time. For the source in free field $t_p = R/c_0$. As each segment of the blade is considered as a source, each of them will correspondingly have a different propagation distance R. This propagation distance R will change during one complete rotation and is also dependent on the orientation of the turbine and position of the observer. The segment at the tip of the blade will have greater variation of R as compared to those closest to the hub, as can be seen in Fig.3.4 The variation in the propagation distance R, for each segment changes the duration of each grain at different angular positions. However, the total time taken for one complete rotation is the same for all segments. If the duration for one complete

rotation is $T_{Rotation}$ and N_γ is the number of discrete angular position, the time duration for each grain at the source end can be written as:

$$\Delta t_s = \frac{T_{Rotation}}{N_\gamma}. \tag{3.3}$$

The time duration for one complete rotation can be calculated from the rotational speed Ω (rad/sec) as $T_{Rotation} = 2\pi/\Omega$, and the discrete angular resolution is given by $\Delta\gamma = 2\pi/N_\gamma$. The corresponding time duration of each grain as observed at the receiver, from Eqs. (3.2) and (3.3), can be written as:

$$\begin{aligned} T_{\Delta\gamma} &= \Delta t_s + \Delta t_p \\ &= \frac{\Delta\gamma}{\Omega} + \frac{\Delta R}{c_0}, \end{aligned} \tag{3.4}$$

where $\Delta t_p = \Delta R/c_0$ is the difference in the propagation time between two successive grains and ΔR is the difference between the propagation distance corresponding to two successive angular positions γ. ΔR can be positive or negative, thus changing the size of the observed grains. The grain of duration $T_{\Delta\gamma}$ contains $N_{\Delta\gamma}$ samples which depends on the sampling frequency.

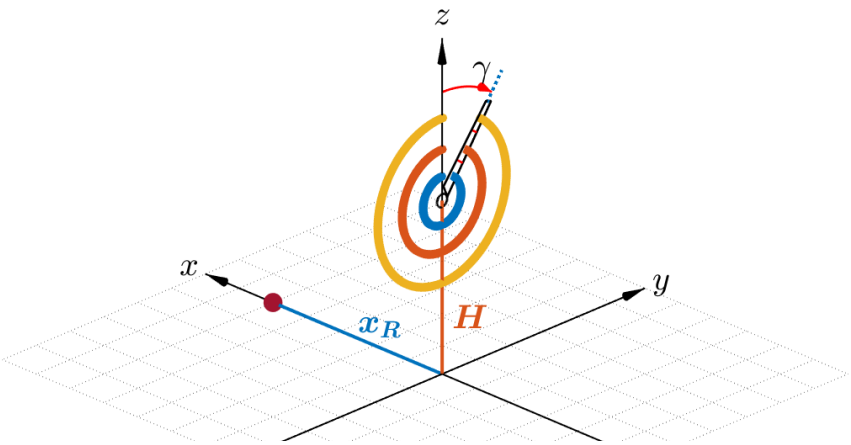

Figure 3.4: Schematic of the blade with three segments observed as sources in rotation by a receiver downwind. The receiver is shown as a sphere. The largest variation for the propagation distance is by the segment near the tip while the smallest variation is for the segment near the hub.

Consider a receiver positioned at a distance $x_R = 100$m from the origin at the angle $\theta = 0°$ (downwind direction) with respect to the x-axis and a single blade of

length 45m rotating in the $y-z$ plane with a hub height of $H = 80\ m$ (Fig. 3.4). If the angular velocity of the rotation is set to 2π rad/sec with only 3 segments on the blade, the receiver time t_r calculated for $c_0 = 340\ m/s$ can be plotted with respect to the source time t_s as in Fig. 3.5b for each segment. Thus a sound emitted at the source at time t_s is observed at the receiver at time t_r. In Fig. 3.5b it can be seen that the time delay is correspondingly shifted for each segment. Fig. 3.5a shows the receiver time t_r excluding the initial propagation time dependent on the initial propagation distance R_1. It can be seen from Fig. 3.5a, even with the exclusion of the initial time delay of the propagation that the variation in the individual grain sizes depends on the absolute position of the segments. This implies that the grain sizes cannot be taken as a constant for all segments of the blade at all positions and so must be calculated for each segment at each angular position.

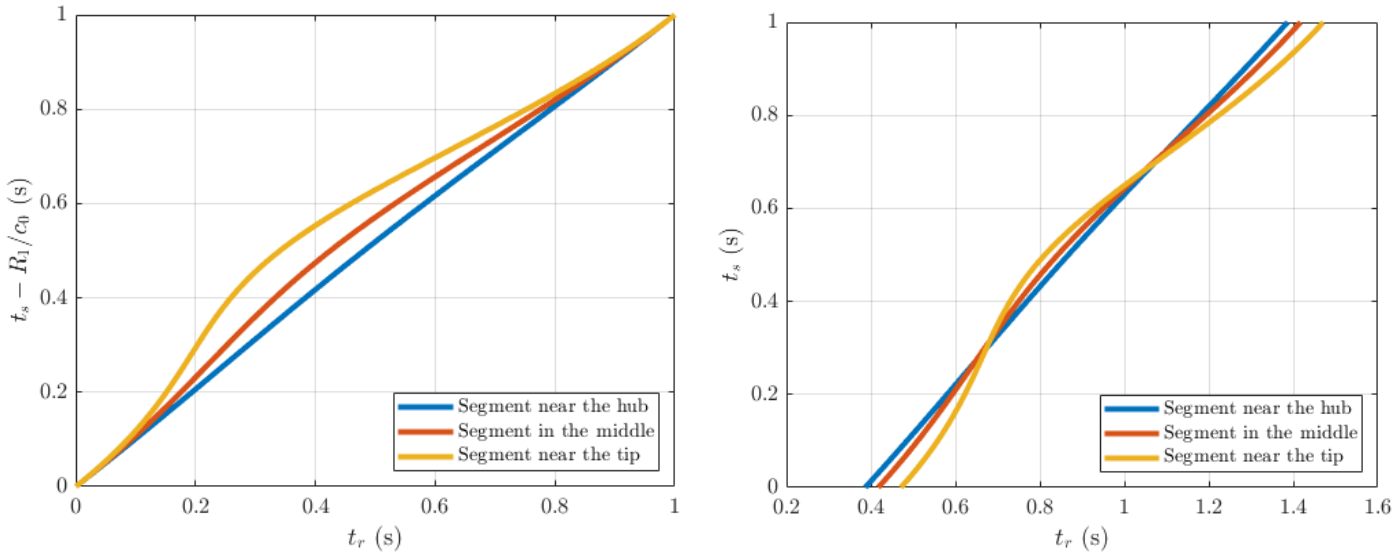

(a) **(b)**

Figure 3.5: For a receiver downwind at $x_R = 100$m (a) The receiver time with respect to the source time excluding initial propagation delay of R_1/c_0, (b) the receiver time with respect to the source time including initial propagation delay for three segments as individual sources in rotation.

The duration of each grain in the system is different which is an important point to consider while designing the window function. This suggests that designing a window function of an absolute length would not be justified as it would change the required length of the grains. Let the functions $f[k]$ and $g[k]$ be defined to serve for the purpose of overlapping between two grains or signals, such that the original power is conserved. Thus, an overlapped section of the grain $p[k]$ is defined as $(p[k])^2 = (p[k]f[k] + p[k]g[k])^2$. The entire window function $W[k]$ of N samples is composed of the overlapping functions $f[k]$ and $g[k]$, with a unit response between

them that can be defined as:

$$W[k] = \begin{cases} f[k] & \text{for} \quad 1 \leq k < w_l \\ 1 & \text{for} \quad w_l \leq k \leq N - w_l \\ g[k] & \text{for} \quad N - w_l < k \leq N, \end{cases} \tag{3.5}$$

where w_l is the desired length of the overlap function that is to be set (Fig. 3.6). As mentioned above, designing a window function of a fixed length would not be favourable. However, it is necessary to set the desired length w_l for the overlapping function as a constant so that all the grains have the same amount of overlap that does not change for each grain. The variability of the grain lengths are then obtained through the length of the unit response between the overlap functions which is $N_{unit} = N - 2w_l$.

As the overlap functions are set to have the same length w_l, the total length of the window N consists of the length of the grain $N_{\Delta\gamma}$ and length $w_l/2$ for the preceding overlap and length $w_l/2$ for the successive overlap (Fig. 3.6). The relation between the length of the window N and the desired length of the overlap function w_l is thus obtained as:

$$\begin{aligned} N &= w_l/2 + N_{\Delta\gamma} + w_l/2 = N_{unit} + 2w_l \\ \rightarrow N_{\Delta\gamma} + w_l &= N_{unit} + 2w_l \\ \rightarrow N_{unit} &= N_{\Delta\gamma} - w_l. \end{aligned} \tag{3.6}$$

This gives us a limit to define the length of the overlap function w_l. For the smallest grain length in the system, $N_{unit} = 0$, which gives us, $\min(N_{\Delta\gamma}) = w_l$. The length of the overlap function w_l is thus restricted to $0 \leq w_l \leq \min(N_{\Delta\gamma})$ allowing us to choose the amount of overlap that is necessary without affecting the length of each grain. The required amount of overlap can be defined as a percentage of the length of the smallest grain as:

$$\Psi = \frac{w_l}{\min(N_{\Delta\gamma})}, \tag{3.7}$$

with $0 \leq \Psi \leq 1$. Thus for $\Psi = 100\%$, the overlap length w_l corresponds to the size of the smallest grain $\min(N_{\Delta\gamma})$, which means that 50% is overlapped by the

preceding grain and the other 50% by the next grain (Fig. 3.7a). Fig. 3.7 shows the window function with $\Psi = 40\%$ and $\Psi = 100\%$.

It has been verified with the help of the ray-tracing model that with the inclusion of the propagation effect on the grain size, $T_{\Delta\gamma}$ changes with a maximum difference of 30 ms which is inaudible (See Appendix B). As a result, the calculation of the grain duration can be safely calculated assuming a constant sound speed c_0, as done in Equation 3.4.

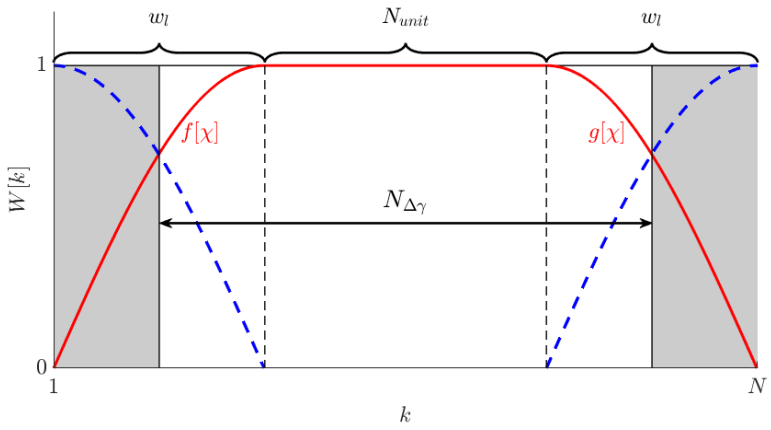

Figure 3.6: The window function $W[k]$ of length N with the overlapping window functions $f[\chi]$ and $g[\chi]$. The white area indicates the grain in consideration and the grey shaded area indicates the previous and next grains. The blue dashed lines represent the overlap functions of the adjacent grains.

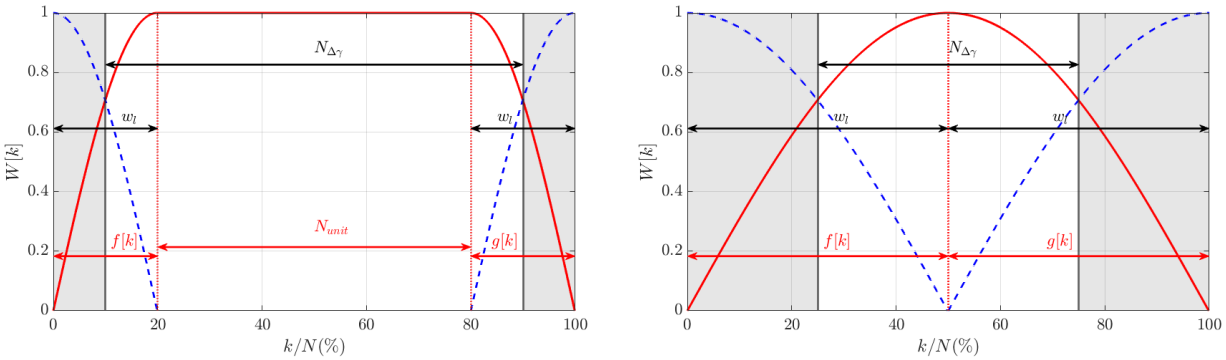

(a) **(b)**

Figure 3.7: The window function $W[k]$ (red solid line) of length N $=N_{\Delta\beta}+w_l$ with the overlapping window functions $f[k]$ and $g[k]$ using (a) Ψ=40% and (b) Ψ=100% of overlap. The white area indicates the grain in consideration and the grey shaded area indicates the previous and next grains. The blue dashed lines represent the overlap functions of the adjacent grains.

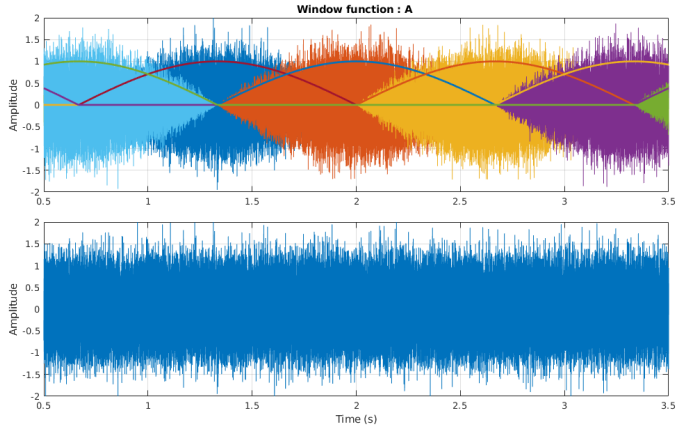

(a) A: $f[k] = sin[k]$, $g[k] = cos[k]$

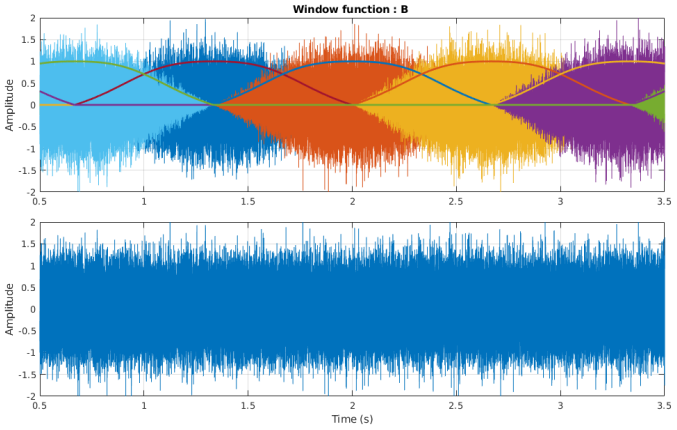

(b) B: $f[k] = \frac{k}{\sqrt{1-2k(1-k)}}$, $g[k] = \frac{1-k}{\sqrt{1-2k(1-k)}}$

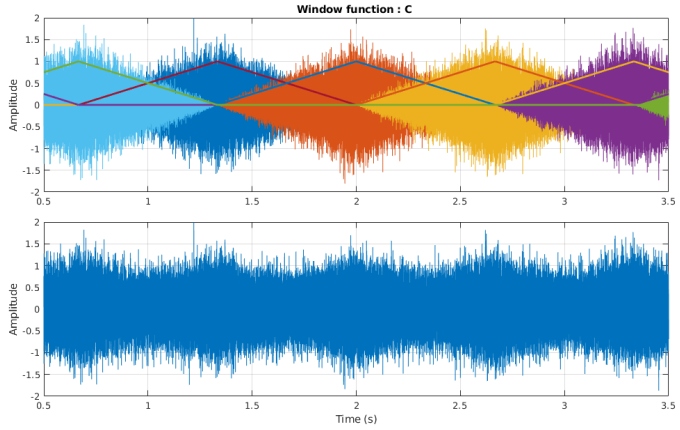

(c) C: $f[k] = k$, $g[k] = 1 - k$

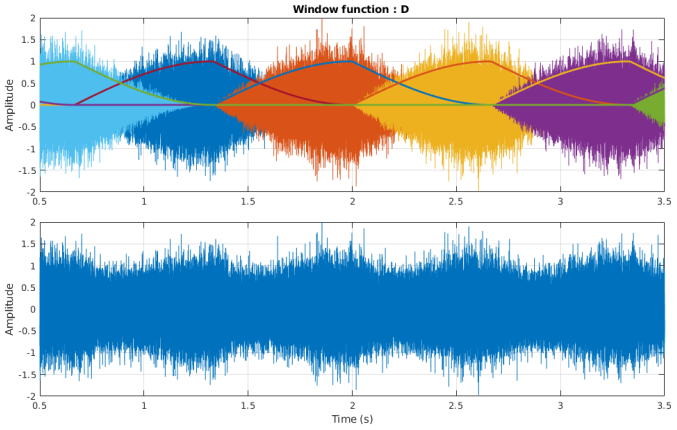

(d) D: $f[k] = sin[k]$, $g[k] = 1 - sin(k)$

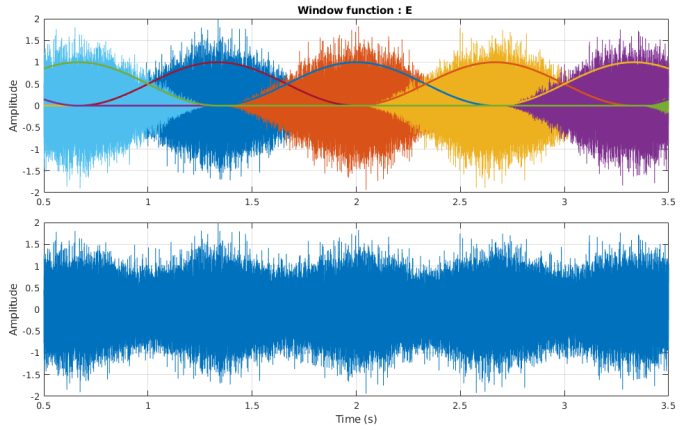

(e) E: $f[k] = sin^2(k)$, $g[k] = cos^2(k)$

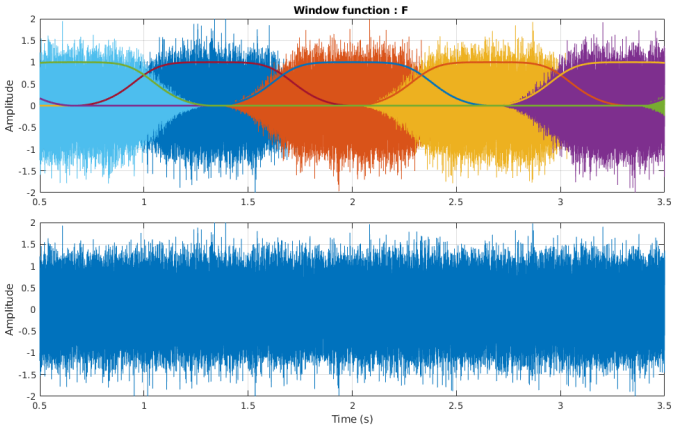

(f) F: $f[k] = \frac{sin^2(k)}{\sqrt{cos^4(k)+sin^4(k)}}$, $g[k] = \frac{cos^2(k)}{\sqrt{cos^4(k)+sin^4(k)}}$

Figure 3.8: White noise synthesized using different overlap functions for the window function applied to the normalized time $k \in [0, \frac{\pi}{2}]$ with 100% overlap.

3.5.2 Overlap function

With the length of the window accurately defined, the overlap functions $f[k]$ and $g[k]$ are to be described appropriately so as to ensure that the overall power of

the overlapping grains is conserved. Such transitions of audio signals are known as cross-fading. During the cross-fade of two successive grains, $g[k]$ of the signal is used to overlap along with the $f[k]$ of the next signal. Hence, if g corresponds to the fade-out of the signal then f is the fade-in of the next signal.

For two signals to cross-fade while maintaining the required power level during the transition, the cross-fading functions g and f, must satisfy the equation given by [25]:

$$f^2 + 2\ f\ g\ r_{(p_1,p_2)}\ + g^2 = 1, \tag{3.8}$$

where $r_{(p_1,p_2)}$ is the correlation coefficient between the two overlapping signals p_1 and p_2, which is zero for uncorrelated signals and one for completely correlated signals. As we assume that two consecutive grains are uncorrelated, $r_{(p_1,p_2)} = 0$ so Eq. (3.8) satisfies the Princen-Bradley criterion [6]. For a normalized time index χ, defining the function $S(\chi) = f(\chi)/g(\chi)$ and assuming Eq. (3.8) holds:

$$g(\chi) = \frac{1}{\sqrt{1\ + S(\chi)^2}}. \tag{3.9}$$

The function $S(\chi)$ is restricted by $S(0) = 0$, $S(1) = \infty$ and $S(0.5) = 1$, which narrows the selection of the cross-fading functions f and g. Several functions satisfy these conditions for $S(\chi)$. The cross-fading functions can also be selected directly from Eq. (3.9), by choosing f and deriving for g, or vice-versa. The function $S(\chi) = \tan(\frac{\pi\chi}{2})$ leads to the window functions $f(\chi) = \sin(\frac{\pi\chi}{2})$ and $g\ =\ \cos(\frac{\pi\chi}{2})$.

Cases	f[k]	g[k]
A	sin[k]	cos[k]
B	$\frac{k}{\sqrt{1-2k(1-k)}}$	$\frac{1-k}{\sqrt{1-2k(1-k)}}$
C	k	1-k
D	sin[k]	1-sin[k]
E	$sin^2[k]$	$cos^2[k]$
F	$\frac{sin^2(k)}{\sqrt{cos^4(k)+sin^4(k)}}$	$\frac{cos^2(k)}{\sqrt{cos^4(k)+sin^4(k)}}$

Table 3.1: Cases of the overlap function tested.

A few cross-fading functions that are tested are given in Table 3.1. To compare functions that are classical along with those derived using Eq. (3.8), white noise of an arbitrary level is windowed and reproduced while attempting to maintain the original constant power during the overlap. Fig. 3.8 shows the reproduced signal using different window functions and the $L_{eq,125ms}$ defined as $\mathrm{SPL_{FAST}}$ of the final

windowed signals are shown in Fig. 3.9. It can be seen that for cases A, B and F for which the power is conserved during the overlap, functions f and g are derived from Eq. (3.9). However, the power is not conserved for cases C, D, E where classical functions are used as the overlap functions f and g.

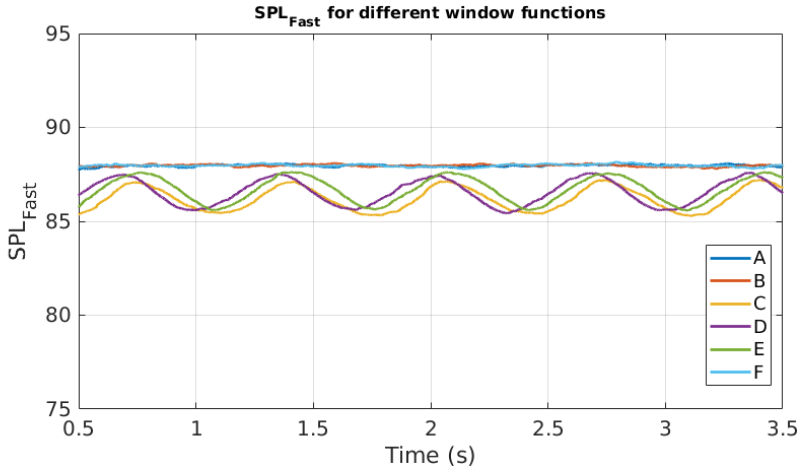

Figure 3.9: SPL_{Fast} calculated for the overlapping window functions of Fig. 3.8.

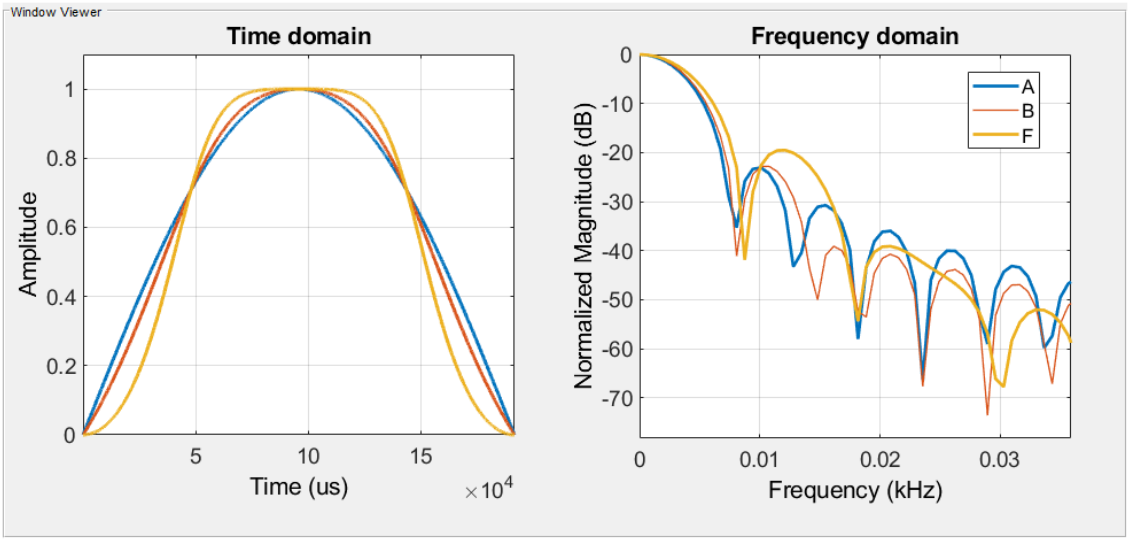

Figure 3.10: The frequency response of the window functions A, B and F given in Table 3.1.

From studying the above cross-fading functions A, B and F are seen to have no loss in power during the cross fading of two grain segments. On investigating the frequency response of these cross-fading functions it is seen that there is greater spectral leakage for window F compared to windows A and B from Fig 3.10. The cross-fading functions A and B show comparable responses and so either can be used for the cross fading of the audio segments with minimum audible noticeable

difference between the two. Since functions defined in case A are easier they will be used in the following. We thus obtain the cross-fading functions which are $f(\chi) = \sin(\frac{\pi\chi}{2})$ and $g(\chi) = \cos(\frac{\pi\chi}{2})$, where $\chi \in [0, 1]$ is the normalized time index.

Figure 3.11 shows a tip segment synthesized without a window function for receiver at downwind and crosswind positions. The change in the level of the pressure between each grains can be seen clearly for the crosswind position. Figure. 3.12 shows a tip segment synthesized with the described window function and $\Psi = 100\%$ for receiver at downwind and crosswind positions. It can be seen that the transition between the each grains is smoother.

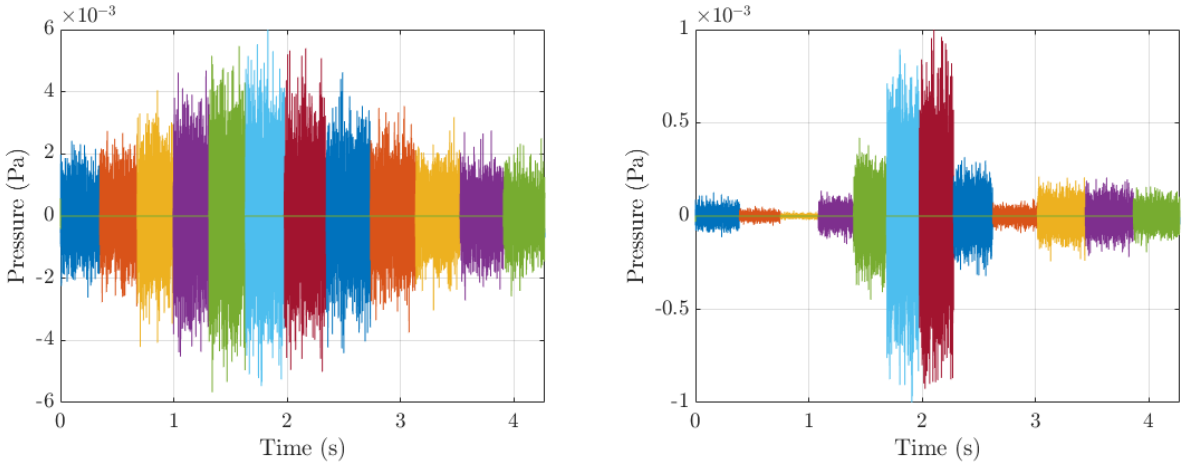

(a) **(b)**

Figure 3.11: Signal from one blade segment made up of the successive allocation of the 12 grains ($\Delta\gamma = 30°$) without windowing observed for a receiver at $x_R = 100m$ (a) downwind $\theta = 0°$ and (b) crosswind $\theta = 90°$

3.6 Influence of overlap amount and number of discrete angular positions

Now with the window function clearly defined along with the method of grain synthesis, we can stitch together the multiple grains to synthesize a segment in complete rotation. However, the quality of the synthesized signals depends on two parameters that need to be chosen carefully. The first parameter is the number of discrete angular positions N_γ which relates to the number of grains in the system and the other is the amount of overlap Ψ. We investigate the quantitative influence of these parameters on the synthesized signals in this section.

To understand the influence of the parameters Ψ and N_γ, a single segment is

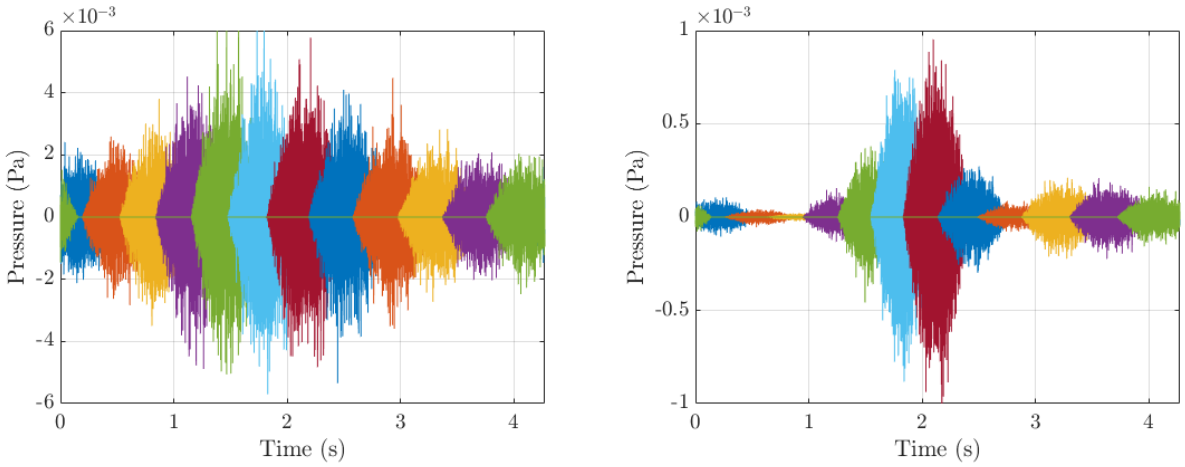

Figure 3.12: (a) Signal from one segment of one blade made up of a composite of 12 windowed grains ($\Delta\gamma = 30°$) observed for a receiver at $x_R = 100m$ (a) downwind $\theta = 0°$ and (b) crosswind $\theta = 90°$.

auralized. For this test case we synthesize trailing edge noise in free field emitted by the tip segment of one blade at a radial distance of 45 m using a rotational speed Ω= 1.47 rad/sec and hub height of $H_0 = 80$ m. This corresponds to the case for which the discontinuities in the time signal are easily heard. The wind velocity for all position is taken to be 8 m/s (no wind shear). The distance of the receiver is $R_0 = 100$ m from the base of the hub. To clearly observe the change in amplitude, the receiver is placed where the maximum change in amplitude of the noise is expected which is for a receiver at the crosswind position ($\theta = 90°$). The number of grains N_γ and the overlap amount of Ψ are separately varied and investigated individually.

A moving RMS over 50 ms is used as an envelope function to detect the changes in the synthesized signal that relate to the contribution of individual grains. The time duration of the moving window is well adapted to detect the structural differences in the signal as the minimum grain duration for this system is larger than 50 ms. The change in the amplitude of the grains is quantified by taking the sound pressure level (SPL) of the time derivative of the moving RMS which is defined as:

$$L_{dp}(t) = 10 \ \log_{10}\left(\frac{(dp_{\mathrm{rms,50ms}}/dt)^2}{(p_{\mathrm{ref}}/1\ \mathrm{s})^2}\right) \quad , \tag{3.10}$$

where $p_{rms,50\mathrm{ms}}$ is the moving RMS over 50 ms.

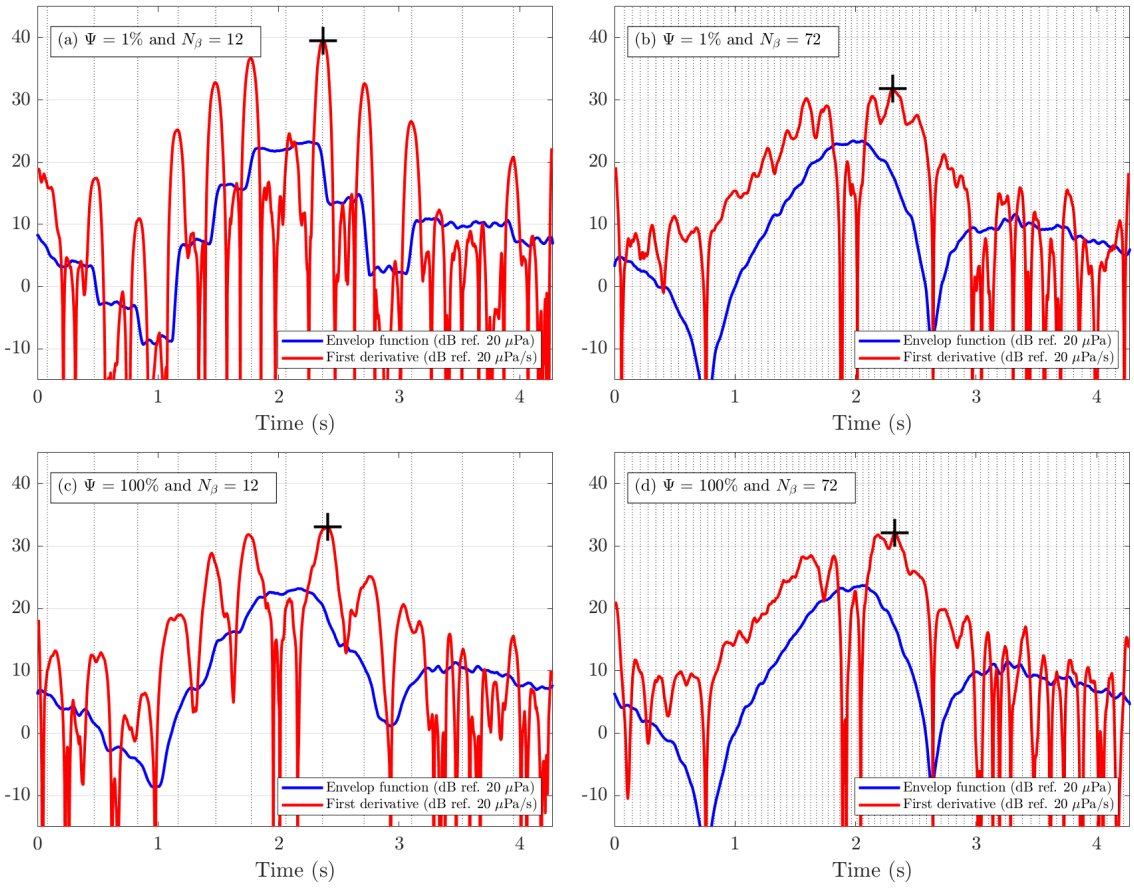

Figure 3.13: The SPL of the envelope function (blue) and the SPL of the corresponding time derivative $L_{dp}(t)$ (red) for different values of N_γ and Ψ. The vertical lines indicate the transitions in time between the grains and the black cross shows the peak of the derivative.

3.6.1 Overlap amount in the cross-fading between grains

The amplitude variations between successive grains are captured as peaks in the level L_{dp} as seen in Fig. 3.13. The test case: "Single segment" is auralized for different values of Ψ, between 1% and 100% with N_γ=12 (Fig. 3.13). This difference between the change in the amplitudes of each grain for different values of Ψ is clearly audible[1]. The larger the amount of the overlap between two grains, the smoother is the audible transition. A difference of ~ 6 dB of the rate of amplitude change is seen between the maximum and minimum values of the overlap (Fig. 3.13a and c). The maximum rate of change in the amplitude in the synthesized signal, represented as crosses in Fig. 3.13 is used to quantify the quality of the transitions for different overlap amounts and number of discrete angular positions. For different values of Ψ, the maximum rate of amplitude change between grains is seen in Fig. 3.14a.

[1]Audio signals available on `https://doi.org/10.5281/zenodo.7220843`

During each realization of the synthesis the phase is randomized which produces the variations in the level peaks. Over 50 iterations, the standard deviation and mean value of the level peaks converge with a maximum difference of less than 0.5dB. As the computational cost is the same for any value of Ψ, choosing the optimal amount of $\Psi = 100\%$ is beneficial for the synthesis of the signal.

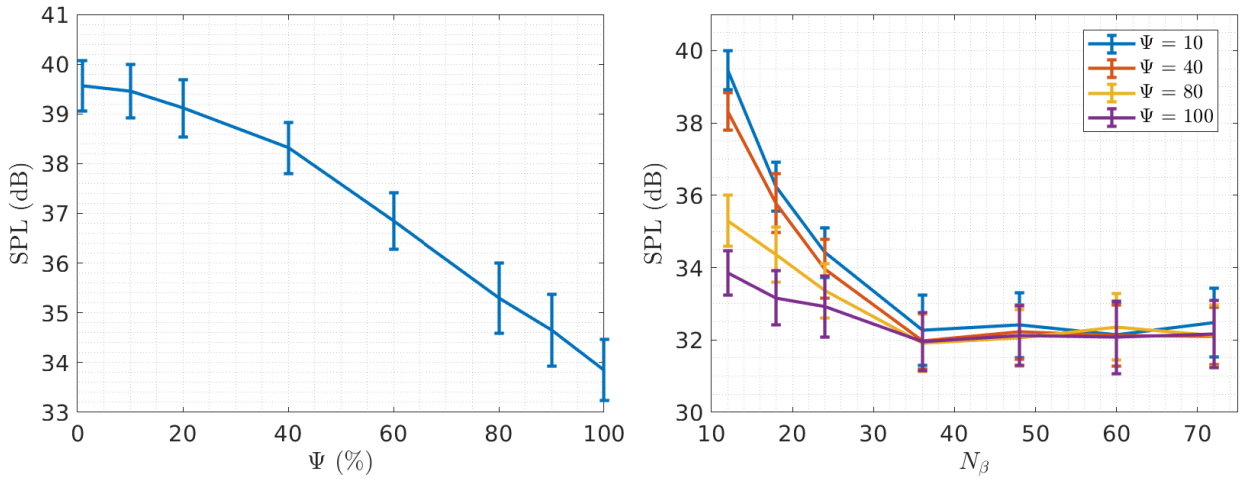

(a) **(b)**

Figure 3.14: Maximum of the calculated SPL L_{dp} for (a) different values of Ψ with $N_\gamma = 12$, (b) different values of N_γ. The error bars show the standard deviation calculated over 50 realizations.

3.6.2 Influence of the number of grains

The number of grains in the auralized signal is equal to the number of discrete angular positions N_γ set for the rotation of the blade. It is apparent that the larger the number of angular positions, the closer the system approaches the continuous rotational motion of the blade. The difference in the amplitude between two adjacent grains changes with the number of discretized angular positions in a single rotation. For a larger number of discretized angular positions, the amplitude change between adjacent grains is less, resulting in a smoother transition between grains in the auralized signal. The influence of N_γ on the quality of the auralized signal can be related to the rate of the amplitude change between grains. To understand how the quality of the auralized signal is influenced by N_γ, the "Single segment" test case is considered as in the previous section (Section 3.6.1) using different values of N_γ with Ψ=10%. The influence of the N_γ and Ψ on the synthesized signal can be seen in Fig. 3.13.

Following the same analysis as done previously, the rate of amplitude change

in the level of L_{dp} is captured by taking the SPL of the moving RMS which is defined by Eq. (3.10). For different values of N_γ, the maximum rate of amplitude change between grains is seen in Fig. 3.14b. It is clear from Fig. 3.13 and 3.14b that the quality of the transitions in the auralized signal is influenced by the number of discrete angular positions, N_γ. The value of the maximum rate of change converges for N_γ greater than 36. This difference of the quality of the transitions is also audibly distinct[1], with the largest value of N_γ approaching the smoothest signal. Increasing N_γ comes with an increase of the computational cost. To resolve this particular trade-off between the realism and computational cost, a lower value of N_γ can be used with the largest possible value of Ψ. Using $N_\gamma = 36$ and $\Psi = 100\%$ the signal can be auralized approaching the quality that is attained using $N_\gamma = 72$ and $\Psi = 10\%$ [1].

The auralization done for this analysis concerns a single blade segment in rotation. Accounting all the segments of the wind turbine blades will induce less audible artifacts and noticeable differences, as the transitions of each grain occur at a slightly different time for each segment at each position. Thus the transitions between grains are not noticeable when a complete wind turbine is synthesized with $N_\gamma = 36$ and $\Psi = 100\%$ (See Section 3.8).

3.7 Colored noise tail

A physics-based synthesis for a wind turbine in free field is achieved between the frequencies f_{min} and f_{max}. However, a sharp drop of the frequencies above f_{max} in the synthesized signals makes the sound appear artificial. To avoid this artificial perception, a tail of colored noise is added in the frequency domain before the IDFT for the frequencies above f_{max} for each grain following the structure,

$$SPL \propto 10 \log_{10}[f^{-n}] \tag{3.11}$$

The investigated noise colors are given in Table 3.2. The SPL corresponding to the smallest frequency in the added noise tail is equal to the level at f_{max}. In other terms it can be said that the first third octave band level of the colored noise corresponds to the last third octave band of the synthesis containing f_{max}. Fig. 3.15 shows the frequency response of each of the investigated added noise tails. It can be seen that for the cases A and B, which correspond to white noise and pink noise respectively, there is an excess of high frequency noise. This gives the synthesized signals a high

[1] Audio signals available on `https://doi.org/10.5281/zenodo.7220843`

frequency hiss which is audible. The cases C and D are acceptable choices and also are audibly similar. For our synthesis we select the brown noise (case C) to be added for the tail at each grain as it serves our purpose and is also a known colored noise. In free-field, the addition of the brown noise tail is justified as the expected noise level at higher frequencies are very low and the spectra is close to the slope of brown noise as can be seen in Fig. 3.15.

Cases	n
A	0 (White noise)
B	1 (Pink noise)
C	2 (Brown noise)
D	4

Table 3.2: Cases of the different colored noise investigated.

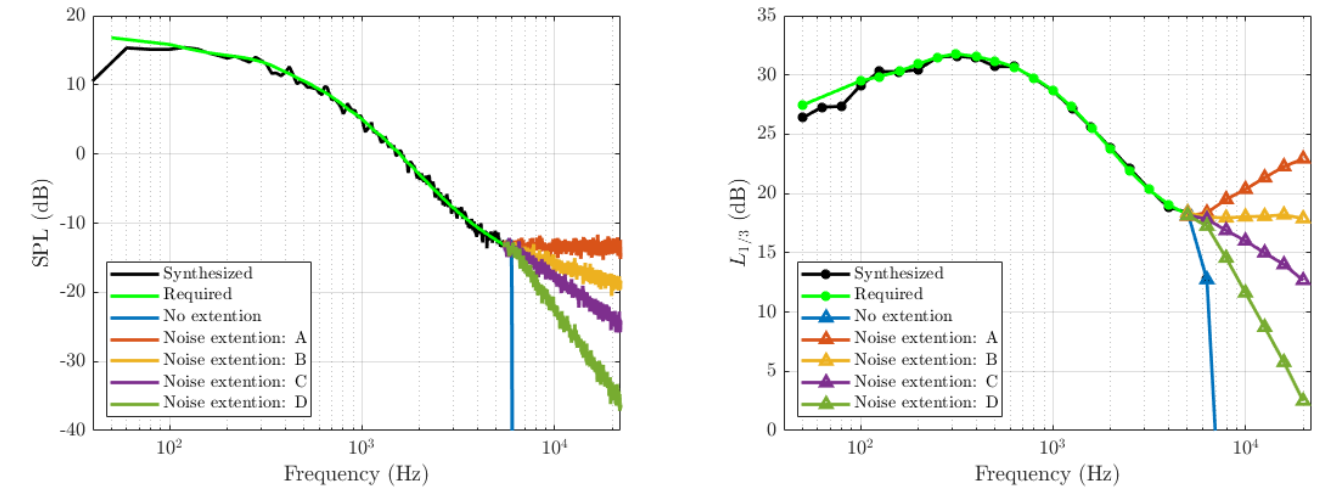

(a) **(b)**

Figure 3.15: (a) Narrow band spectrum and (b) Third octave band spectrum of the synthesised signal with the added colored noise.

With the addition of the propagation effects due to atmospheric absorption, the level of the higher frequencies is reduced further and close to inaudible. The inclusion of the brown noise at the higher frequencies is thus not mandatory with the addition of propagation effects for the purpose of auralistic reality but preferable to obtain high-quality audio signals with a smooth frequency response.

3.8 Synthesis of the complete wind turbine

With the required elements described, the synthesis of the complete wind turbine is now possible. As an example, we consider the blade with $N_{seg} = 8$ segments. The

rotational speed of the blade is set to $\Omega = 1.47$ rad/s with 36 discrete angular positions γ. The hub height of the wind turbine is taken as $H_0 = 80\ m$. The observer at the downwind direction ($\theta = 0°$) on the ground at the distance of $x_R = 100\ m$ from the base of the hub receives the signal from each segment with the corresponding delay. The received signals for the 8 segments in free field, including the propagation time delay for each segment of one blade over one complete rotation are plotted on top of each other in Fig 3.16.

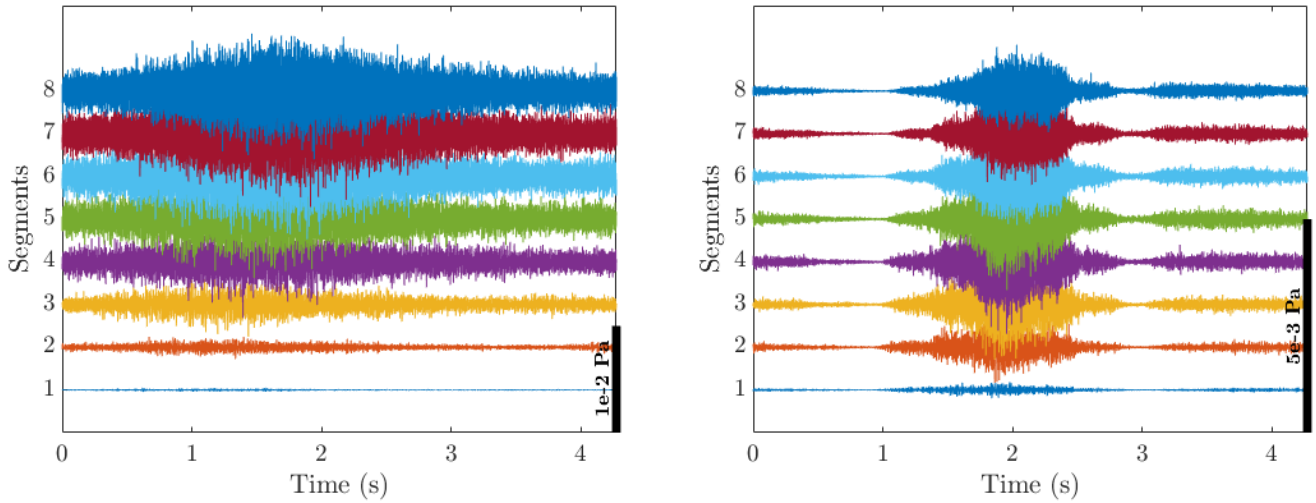

(a) **(b)**

Figure 3.16: Signal from the 8 segments in free field for a receiver position at $x_R = 100m$ (a) Downwind and (b) Crosswind. The signals for each segment are offset for comparison.

As mentioned in Section 3.5.1, the time duration for one complete rotation is the same for all segments: $T_{Rotation} = 2\pi/\Omega$. But including the propagation time per segment, the composite signal that is received from each segment is slightly different due to delay of the closest and furthest segment which is as expected. However, as the synthesized signal is aimed to replicate a recording of wind turbine noise, it can be safely assumed that the blade is in continuous motion. This can be easily achieved by applying a circular shift on each of the segments' signals received by their respective initial propagation times before summing them. The total duration of the signal is maintained to be $T_{Rotation}$.

The signal from the second and third blades is similarly obtained by shifting the composite signal of one blade by 1/3 $T_{Rotation}$ and 2/3 $T_{Rotation}$. Adding the response from the three individual blades gives the complete auralization of the wind turbine for one rotation. For the multiple rotations, the complete auralized

signal can be simply added in succession. The composite signal for four rotations and the corresponding spectrogram for the complete wind turbine with the arrangement as described above is shown in Fig. 3.17.

Comparing the input PSD obtained from the frequency-domain model to the time averaged PSD of the resultant auralized signal shows that the complete auralized signal is reproduced fairly well (Fig. 3.18). The short-term overall SPL of the frequency-domain model and of the auralized signal are also close as seen in Fig. 3.19. With the synthesis method defined, the auralization can be extended further for other settings. The entire synthesis method described is independent of the noise producing mechanisms. In other words, the method described is an efficient tool to convert frequency-domain wind turbine noise predictions into a time signal. In this section, we have synthesized TEN in free field for illustration purposes, but the tool can be extended to include TIN and also outdoor propagation effects. We include the propagation effects in the frequency-domain model as per Chapter 2 and discuss a few test cases in the next section.

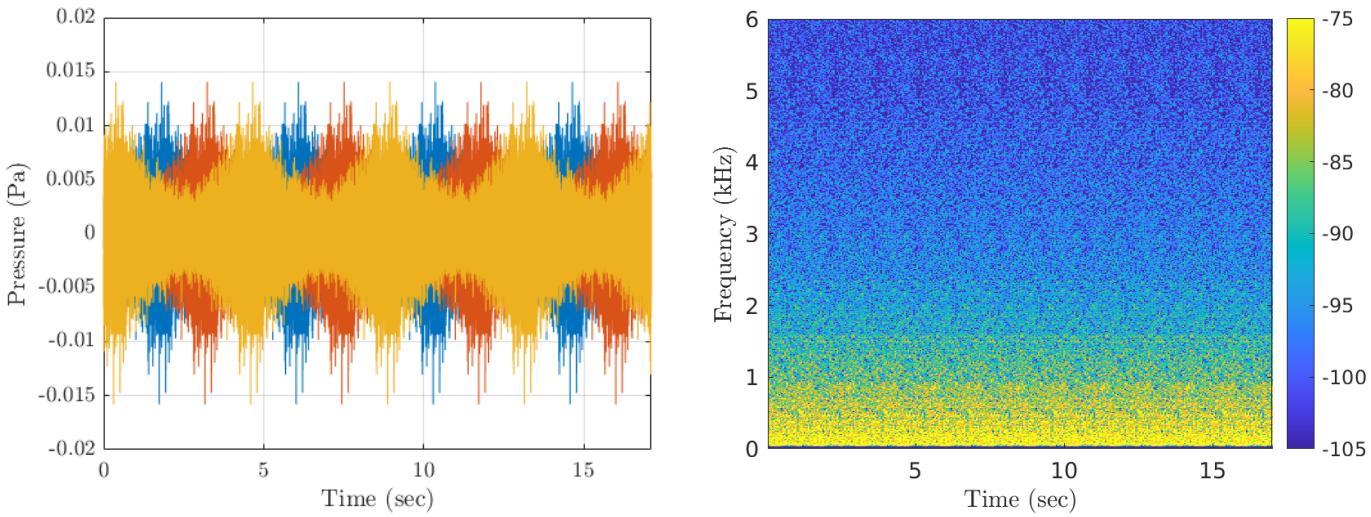

(a) **(b)**

Figure 3.17: (a) Composite signal of three blades in free field represented with different colors and 4 rotations as observed for the receiver at $x_R = 100$m, $z_R = 0$m and $\tau = 0°$ (b) Spectrogram of the composite signal of three blades and 4 rotations. (Sampling frequency fs= 44.1kHz, Window resolution df = 20Hz with a Hanning window. Frequency plotted in the log-scale.)

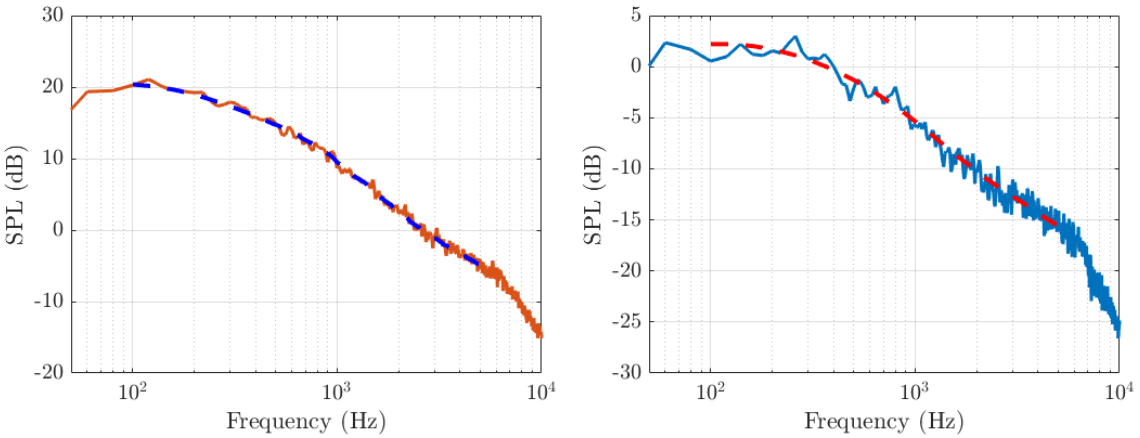

(a) (b)

Figure 3.18: PSD of the synthesized signal (solid line) and the input data (dashed line) for the receiver x_R=100 m (a) downwind and (b) crosswind in free field.

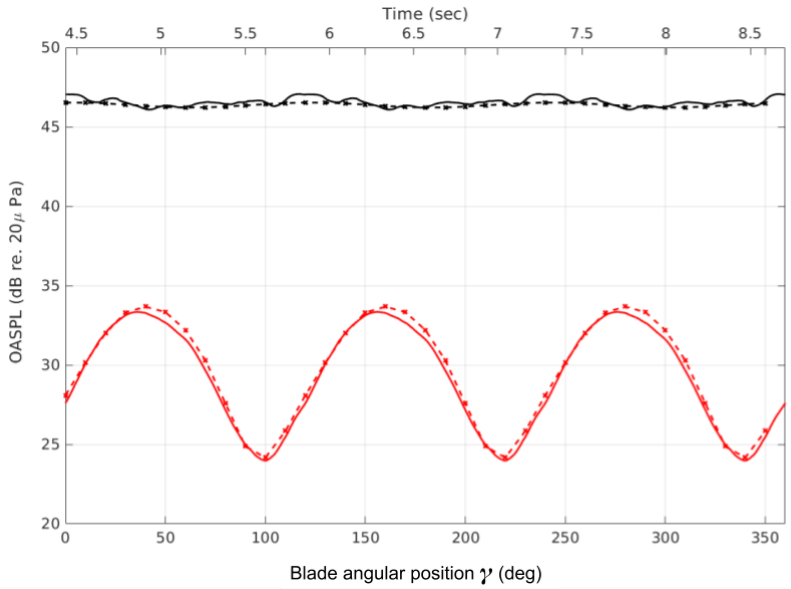

Figure 3.19: The OASPL ($L_{eq,125ms}$) from the auralized signal (solid line) and from the frequency-domain model (dashed line) for downwind (black) and for crosswind (red)

3.9 Test cases

As in the article of Tian and Cotté [89], we model a wind turbine with a hub height of $H = 80$ m and a blade span of 45 m divided into 8 segments. The rotational speed $\Omega = 1.47$ rad/s is set and one rotation is divided into $N_\gamma = 36$ discrete angular blade positions as in the previous section. The receiver is placed at various distances x_R between 500m to 1000m and a constant height of $z_R = 2$ m and at an angle θ

with respect to the wind direction (Fig. 2.1a). The wind speed profile implemented follows the power-law profile of Eq. (2.34) with the wind speed U_{ref} = 8m/s at the reference height z_{ref}= 80 m and different wind shear exponents α between 0.2 to 0.5. The SPL in free field is computed for TEN and TIN for the set of frequencies between 100 Hz and 6000 Hz that are given in Table 2.6. In the propagation model, the influence of the scattering due to the turbulence ΔL_{scat} and the atmospheric absorption $\alpha_{\text{abs}}R$ are calculated for the same frequencies and all the segments at each height.

As it is very time consuming to calculate ΔL_{PE} above 2kHz and wind turbine noise levels are very low at frequencies beyond it, ΔL_{PE} is calculated only from 100 Hz until 2300 Hz using 7 heights equally distributed between 35m to 125m as per the moving monopole model. Cotté (2019) has shown that 7 seven heights are sufficient to calculate the amplitude modulations of wind turbine noise with a sufficient accuracy. The average value of ΔL_{PE} for the third octave band at center frequency 2000 Hz is taken as the value of ΔL_{PE} for the frequencies between 2300 Hz and 6000 Hz in order to have a continuous decay of the noise level. We synthesize the signals of the wind turbine noise at the sampling frequency of f_s=44.1kHz between the frequencies f_{min}=100 Hz and f_{max}=6000 Hz for two complete rotations of the blades for various test cases which are described below. In the signals provided in the wav format, 0 dBFS corresponds to 0.1Pa. All the sound files associated to each individual case can be found in the respective table so that the reader can assess

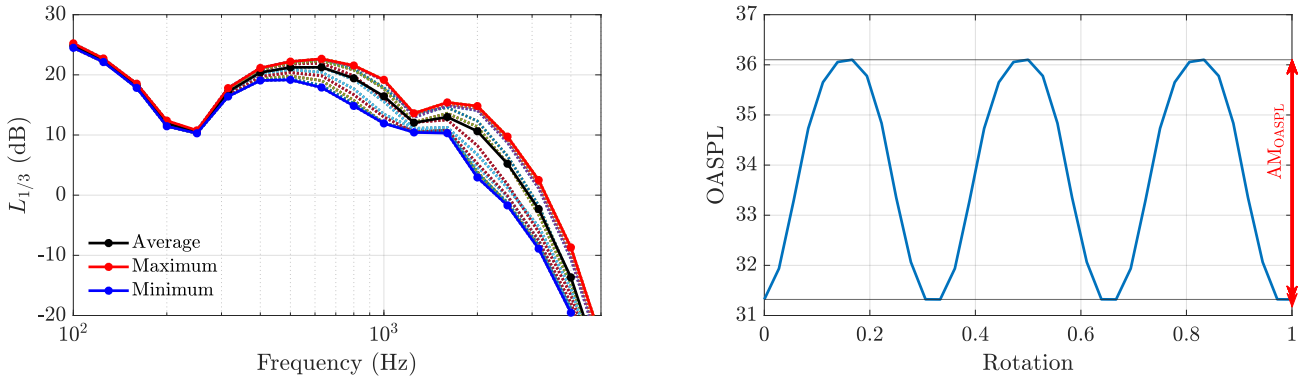

(a) **(b)**

Figure 3.20: (a) Example of the maximum and minimum levels experienced by the receiver at $x_R = 500m$, $z_R = 2m$ and $\theta = 80°$ with a grass ground (Test case A2-2). The dashed lines represent the sound level experienced due to rotation of the blades. (b) OASPL experienced by the receiver over one rotation of the wind turbine blades.

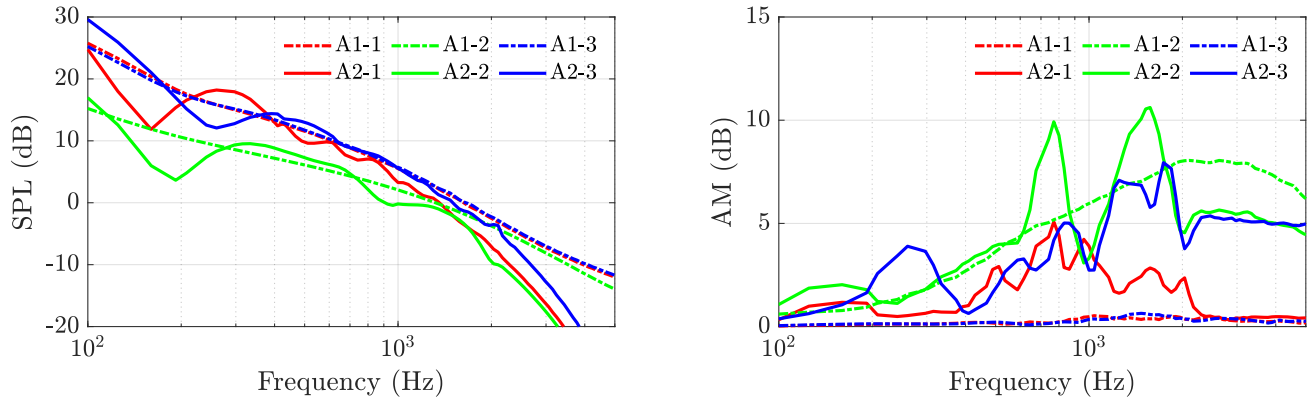

(a) **(b)**

Figure 3.21: Spectra of the (a) time-averaged SPL and (b) AM of the test cases A which are given in Table 3.3

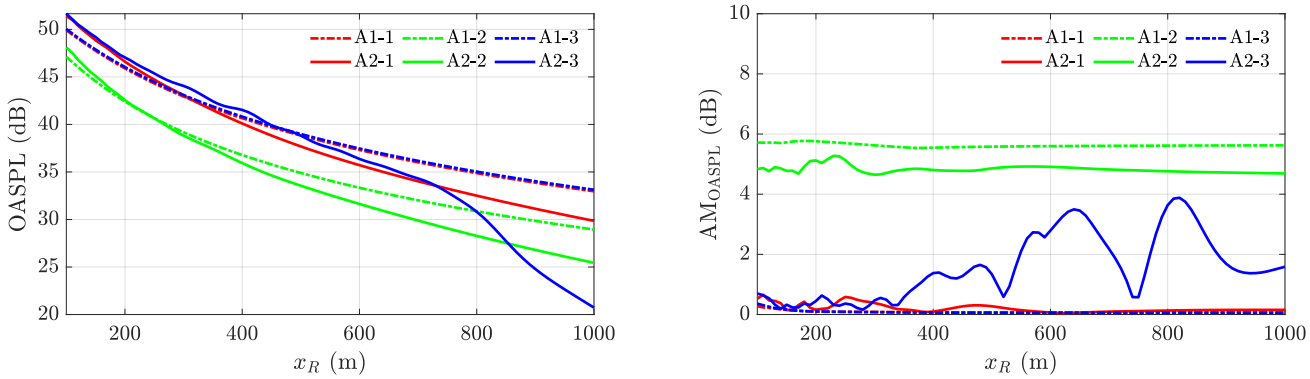

(a) **(b)**

Figure 3.22: (a) OASPL and (b) the modulation of the OASPL of the test cases A given in Table 3.3. The curves of AM_{OASPL} for cases A1-1 and A1-3 are not seen clearly as they are very close to 0.

the differences as mentioned.

3.9.1 A: Free-field vs Propagation effects

We begin by comparing the synthesis done in free field with the synthesis inclusive of the propagation effects. The signals are obtained for a receiver at distance x_R= 500 m downwind $\theta = 0°$, close to crosswind $\theta = 80°$ and upwind $\theta = 180°$. For the wind speed profile, the shear exponent is taken as α =0.3. For this test case, a grass ground in summer [35] is implemented via the Miki-model. The turbulence considered in the TIN (Eq. 2.13) and also in ΔL_{scat} for the scattering due to the

Cases	θ(deg)	System	Signal [1] (.wav file)
A1-1	0	Free field	A1-1
A1-2	80	Free field	A1-2
A1-3	180	Free field	A1-3
A2-1	0	Grass-summer	A2-1
A2-2	80	Grass-summer	A2-2
A2-3	180	Grass-summer	A2-3

Table 3.3: Test cases A: x_R= 500 m, Wind shear exponent α =0.3, medium turbulence and grass ground in summer.

atmospheric turbulence (Eq. 2.30) corresponds to the medium level in Table 2.5. The different parameters for the cases A are shown in Table 3.3. For a quantitative comparison between the test cases, we plot the spectra of the time-averaged SPL in Fig. 3.21a. The maximum difference in the amplitude spectra of the SPL observed by the receiver during the rotation of the blades known as the amplitude modulation (AM) of the noise is plotted in Fig. 3.21b. We also plot in Fig. 3.22a the OASPL averaged over one rotation with respect to distance x_R from the base of the wind turbine which is obtained from the averaged $L_{1/3}$ level (Fig. 3.20a). The difference in the maximum and minimum OASPL observed during one rotation (Fig. 3.20a) termed as the amplitude modulation of the OASPL: $\mathrm{AM_{OASPL}}$ is plotted in Fig. 3.22b.

From the time-averaged SPL in Fig. 3.21a, it is seen that noise received in free field does not contain the interference patterns due the ground reflection. The interference dips vary from 150Hz to 250Hz depending on the orientation of the receiver. The decrease in the SPL level for cases A2 at higher frequencies starting from 1500Hz is due to the atmospheric absorption. It can also be seen that the lower SPL at the cross-wind orientation in comparison to upwind and downwind is maintained as expected [63] even with the addition of propagation effects. This difference between the synthesized signals with and without propagation effects is clearly audible.

During the rotation of each blade, each frequency component of the spectrum is modulated at the blade passing frequency. The maximum difference between the amplitude of the SPL in one rotation varies for each case as can be seen in Fig. 3.21b. The level of modulation for the upwind and downwind condition is nearly the same and almost zero in free field conditions (Cases A1-1,3), which was expected as no propagation effect is considered and the propagation distance is almost the same for all grains. The AM for the case of A1-2 originates mainly from the orientation of the receiver which is close to the rotational plane of the blade. The AM is significantly

changed for most frequencies with the addition of the propagation effects with the maximum change in the AM observed upwind (A2-3) for all frequencies. For the downwind (A2-1) and crosswind (A2-2) condition, the increase in the AM is related to the ground effect that varies with the source heights during the movement of the blade as seen in Fig. 2.18. The influence of the propagation effect is clearer in the case of the upwind condition (A2-3) where there is an increase of around 4 dB in AM between 200-300Hz with the maximum increase of close to 8 dB around 1000-2000Hz. This high increase in the AM is understood using Fig. 2.19(a) where the relative SPL is plotted for three different source heights. Due to upward refraction effects, the receiver is already in the shadow zone for most frequencies at the lowest source height z_S=35m, while the receiver is outside the shadow zone at the highest source height z_S=125m. Thus the receiver moves inside and outside the shadow zone as the blade segments close to the tip fluctuate rotate. This inclusion of the propagation effects increases the level of the AM which becomes comparable to the level in crosswind condition. It is interesting to observe that as the AM for the crosswind case A2-2 originates mainly from the rotation of the blades, which is also observed in free field, the difference in the AM is attributed mainly to the ground reflection. Close to the crosswind condition ($\theta = 80°$, A2-2), the AM appears to slightly decrease at higher frequencies compared to that observed in free-field.

It can be seen from Fig. 3.22a that the OASPL decreases as the receiver is further away from the wind turbine which is expected. With the inclusion of the propagation, the start of the shadow zone around $x_R = 800$m can be seen from the upwind condition. Fig. 3.22b shows that with the inclusion of the propagation effect, the $\mathrm{AM_{OASPL}}$ increases significantly for most orientations of the receiver except close to cross-wind. However for the cross-wind condition, the difference is not much. The largest change in $\mathrm{AM_{OASPL}}$ due to the inclusion of the propagation modulation is seen in the upwind condition, with the level comparable to the near crosswind condition near the beginning of the shadow zone at $x_R = 800m$.

3.9.2 B: Natural ground or grass ground in summer vs winter

We synthesize a few cases similar to A2 with either the grass ground or a natural ground in summer or winter (Table 2.4) while keeping all other parameters the same. The test cases are described in Table 3.4.

The comparative influence of the two types of grounds can be observed in Fig. 3.23. From the direct comparison it can be seen that except for the case of the

Cases	θ(deg)	System	Signal [1] (.wav file)
B1-1	0	Grass-winter	B1-1
B1-2	80	Grass-winter	B1-2
B1-3	180	Grass-winter	B1-3
B2-1	0	Ground-summer	B1-1
B2-2	80	Ground-summer	B1-2
B2-3	180	Ground-summer	B1-3
B3-1	0	Ground-winter	B1-1
B3-2	80	Ground-winter	B1-2
B3-3	180	Ground-winter	B1-3

Table 3.4: Test cases B: x_R= 500 m, wind shear exponent α =0.3, medium turbulence and grass ground in winter.

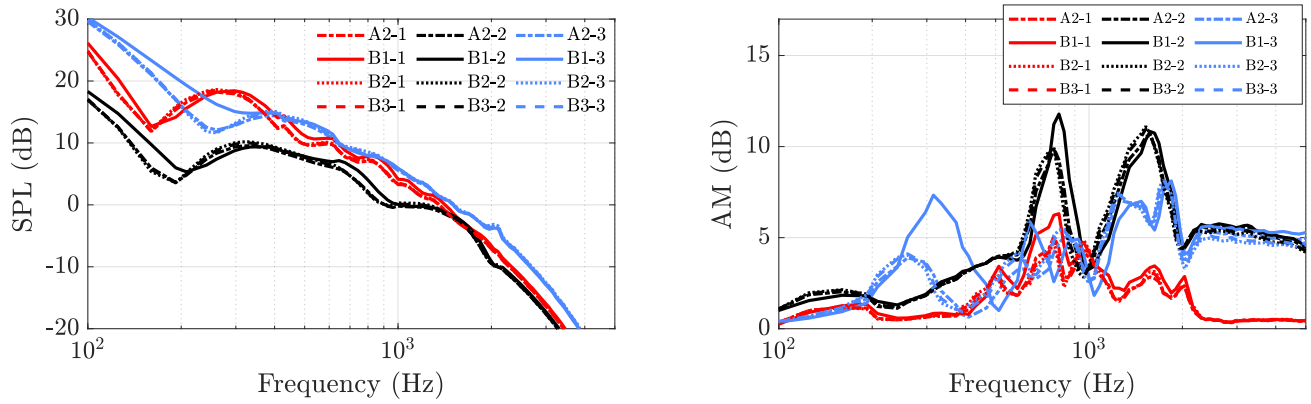

(a) **(b)**

Figure 3.23: Spectra of the (a) Time-averaged SPL and (b) AM of the test cases B which are given in Table 3.4

grass ground in winter, all the other studied grounds give approximately the same response. This makes the comparison possible between two types of grounds: grass ground in winter (B1) and the rest (A2, B2, B3). From Fig. 3.23a, it can be seen that the difference of the SPL between the two types of grounds for the downwind direction ($\theta = 0°$, B1-1) and close to crosswind direction ($\theta = 80°$, B1-2) is small. This difference is more clearly seen between the two types of grounds for the upwind condition at the lower frequencies but the audible difference is not very noticeable. Similarly, the difference is small for the AM as seen in Fig. 3.23b for cases B1-1 and B1-2. The AM is increased by around 3dB for the downwind case B1-3 between the frequencies 250-450Hz. The difference observed in the propagation effects due to the two grounds can be clearly seen in Figs. 2.18 and 2.19. However, the relatively small change in the SPL and AM seen in Fig. 3.23a and Fig. 3.23b in the two

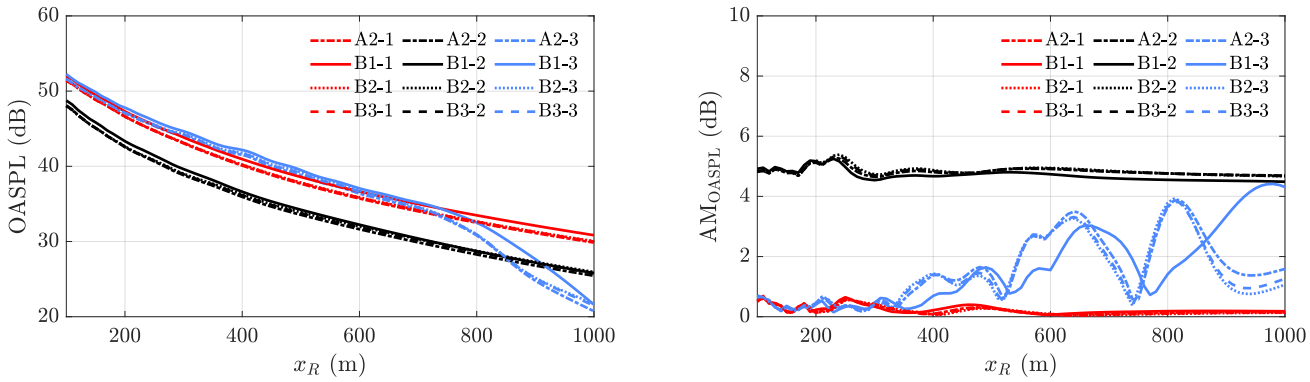

(a) **(b)**

Figure 3.24: (a) OASPL and (b) the modulation of the OASPL of the test cases B given in Table 3.4

types of grounds can be explained by the fact that the synthesized noise inclusive of propagation effect is the sum of the contributions from all segments passing through different source heights. The outcome of this synthesis is an averaged out effect of the influence of the ground reflection. Again it can be seen through Fig. 2.19 that this ground reflection effect is apparent in the upwind conditions (B1-3) due to the receiver fluctuating from inside to outside the shadow zone during one blade rotation. Fig. 2.19 also shows that the start of the shadow zone is not the same for the two grounds used which also contributes to the difference observed in the SPL and AM for the particular case of B1-3.

Fig. 3.24a shows the decrease in the OASPL as expected for the respective orientations. The OASPL for the case of grass ground in winter (B1-3) shows that the shadow zone starts at a larger distance compared to all the other studied grounds. From Fig. 3.24b it can be seen that the AM_{OASPL} for the grass ground in winter is different from the rest of the grounds. The maximum AM_{OASPL} for the upwind condition is seen to be close to the start of the shadow zone around $x_R = 800m$ for the grass and natural grounds in summer, while the maximum for the grass ground in winter is shifted further to $x_R = 1000m$. The reason for this difference between the two types of grounds is due to the cumulative response of ΔL observed by different source heights of the moving monopole model as shown in Fig. 2.18 and 2.19. Another parameter which is known to influence the limits of the shadow zone is the considered wind profile. We again synthesize the noise with the parameters described in the test cases A2 while varying the wind shear exponent α for the next set of test cases.

3.9.3 C: Wind shear

A few test cases are synthesized similar to A2 but using different wind shear exponents while keeping all other parameters the same. The test cases are shown in Table 3.5.

Cases	θ(deg)	Wind shear exponent α	Signal [1] (.wav file)
C1-1	0	0.2	C1-1
C1-2	80	0.2	C1-2
C1-3	180	0.2	C1-3
C2-1	0	0.5	C2-1
C2-2	80	0.5	C2-2
C2-3	180	0.5	C2-3

Table 3.5: Test cases C: x_R= 500 m, medium turbulence and grass ground in summer.

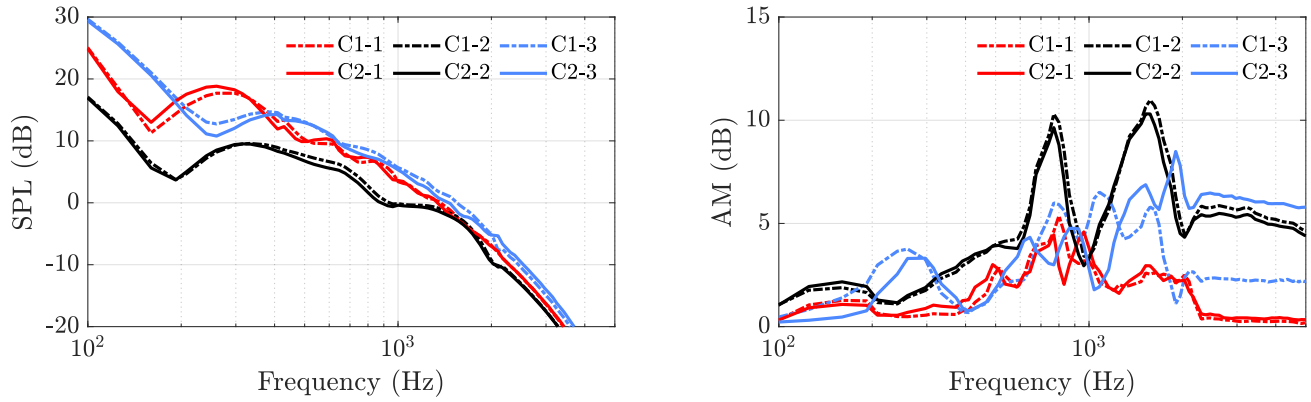

(a) **(b)**

Figure 3.25: Spectra of the (a) Time-averaged SPL and (b) AM of the test cases C which are given in Table 3.5

From Fig. 3.25, it can be seen that the influence of the wind shear on the observed SPL is small and the audible difference is subtle. The cases close to crosswind conditions (θ = 80°, C1-2 and C2-2) show nearly the same response for the SPL as well as the AM for all frequencies, which is expected as the effect of refraction due to the wind shear is low for this orientation. The effect of the different wind shear exponents in the upwind condition (C1-3 and C2-3) is significant in the AM above 1 kHz (Fig. 3.25b). The high AM generated upwind, as explained above, is the fluctuation of the received noise from inside to outside the limits of the shadow zone. This difference can also be heard clearly in the respective signals of this case.

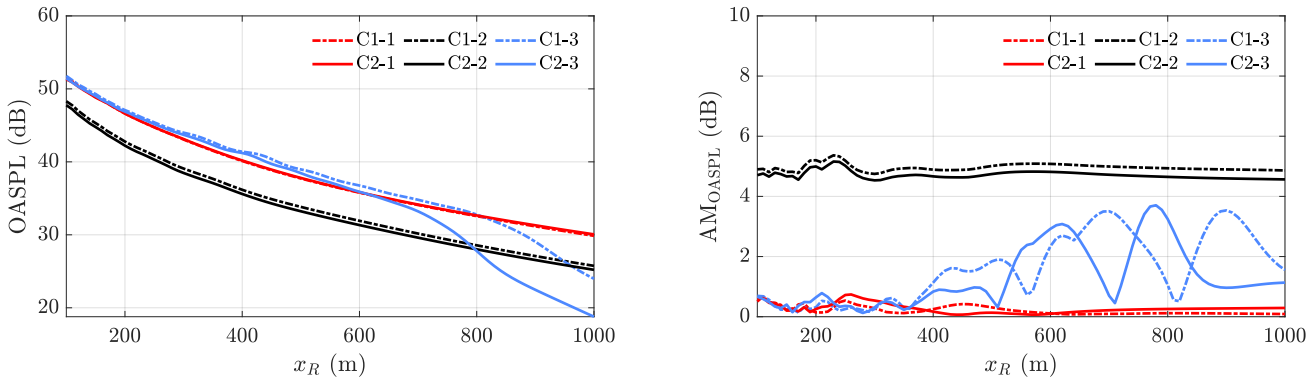

(a) **(b)**

Figure 3.26: (a) OASPL and (b) the modulation of the OASPL of the test cases C given in Table 3.5

As it is known that the wind shear effectively modifies the limits of the shadow zone, the difference between the AM upwind for cases C1-3 and C2-3 is explained. For the downwind cases C1-1 and C2-1, the relatively equal AM is explained by the fact that the maximum difference in the level of the refracted noise observed by each segment is almost the same for the different wind shear exponents and also there is no shadow zone for any source height observed.

As expected the wind shear influences the beginning of the shadow zone upwind, while there is not much influence in the other orientations (Fig. 3.26a). In the downwind condition a slight decrease in the OASPL and AM_{OASPL} is observed. For the upwind case with the higher wind shear (C2-3) it can be seen that the start of the shadow zone is closer to the wind turbine, while for a lower wind shear (C1-3) the start of the shadow zone is further away. Subsequently for the same orientation, the AM_{OASPL} for a higher wind shear seems to be moved towards the wind turbine while AM_{OASPL} for a lower wind shear seems to be moved further away. The OASPL and AM_{OASPL} are plotted in Fig. 3.27 for a few more cases upwind similar to C1-3, C2-3 with different wind shear exponents. From Fig. 3.27 it can be seen that calculated AM_{OASPL} seems to be shifted based on the value of the wind shear exponent α. However, this shift is not linear but also not logarithmic and more investigation is required. Figs. 3.28 and 3.29 show the spectra of time-averaged SPL and AM obtained for different receiver distances and wind shear exponents. By decreasing the receiver range xR when the wind shear exponent alpha increases, an overlap of all spectra can be obtained with less than 2 dB difference. Obtaining an empirical relation of this dependence of the wind shear on the upwind receiver distance and spectra will be beneficial in saving computational resources.

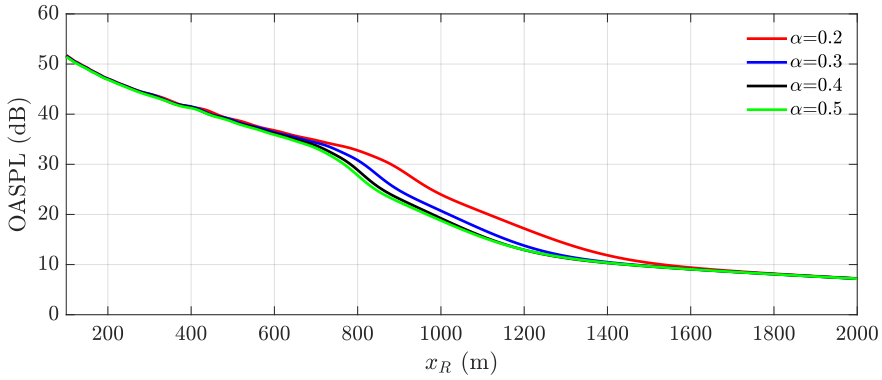

(a)

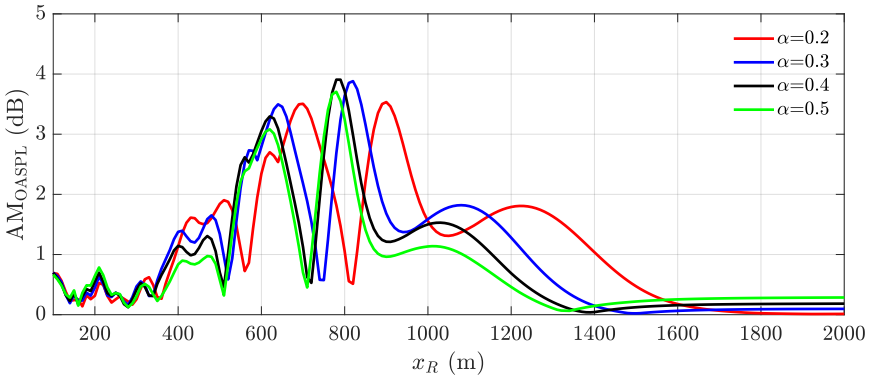

(b)

Figure 3.27: (a) OASPL and (b) the modulation of the OASPL for multiple wind shear exponents α over upwind distance.

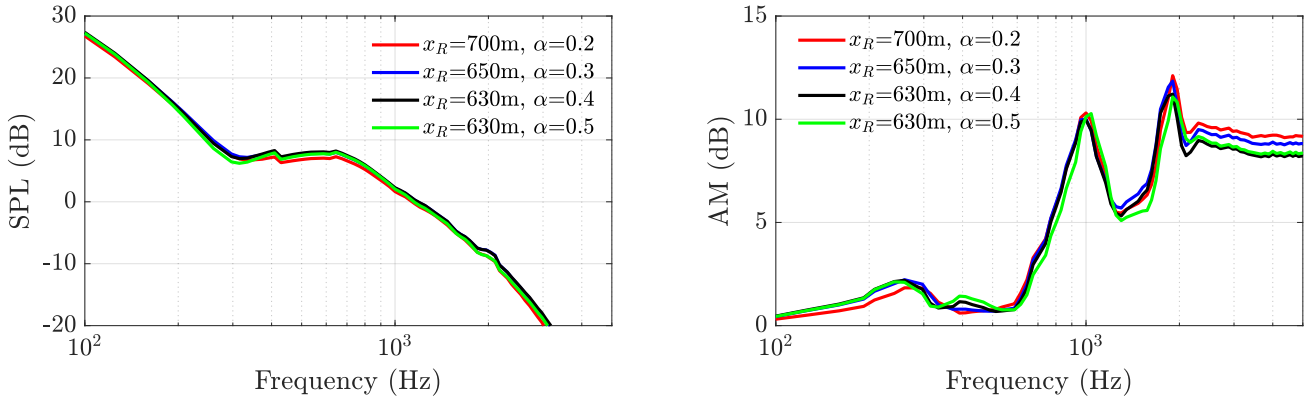

(a) **(b)**

Figure 3.28: Spectra of the (a) Time-averaged SPL and (b) AM obtained for receivers at different upwind distances and wind shear exponents.

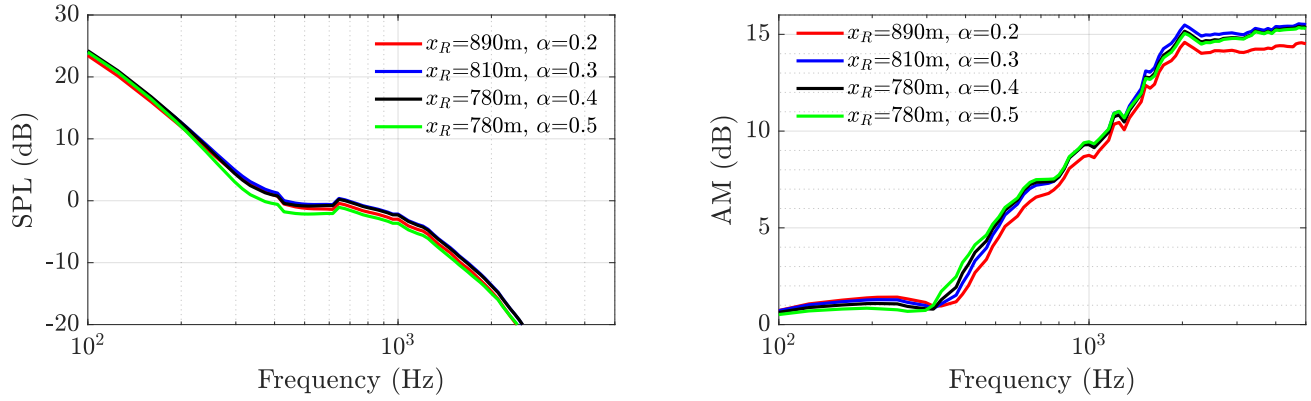

(a) **(b)**

Figure 3.29: Spectra of the (a) Time-averaged SPL and (b) AM obtained for receivers at different upwind distances and wind shear exponents.

3.9.4 D: Scattering due to turbulence

Here, we synthesize a few cases similar to the case A2-3, but with two levels of turbulence while the other parameters remain the same. To study the influence of the scattering due to turbulence, we apply the turbulence to the source (TIN) as well as the scattering (ΔL_{scat}) in the cases D1 (Source and scattering) and compare it to the cases where we apply the turbulence only to the source in D2 (Source only). The test cases are shown in Table 3.6. The turbulence dissipation rate ϵ is modified and corresponds to the low and high levels of turbulence in Tab.2.5.

Cases	TDR $\epsilon(m^2/s^3)$	System	Signal [1](.wav file)
D1-1	0.177	Source and scattering	D1-1
D1-2	0.00054	Source and scattering	D1-2
D2-1	0.177	Source only	D2-1
D2-2	0.00054	Source only	D2-2

Table 3.6: Test cases D: x_R= 500 m, downwind (θ = 180°) and grass ground in summer.

It can be seen directly from Fig. 3.30 that the influence of the scattering due to the turbulence is almost negligible for the SPL as well as the AM. This inaudible difference is also observed in the signals provided. For a high turbulence level it can be seen that SPL is higher due to TIN source model but provides almost the same AM as compared to the case with low turbulence. An explanation of this low scattering level seen in Fig. 2.19 can be attributed to the fact that the receiver is not inside the shadow zone for all the segments of the rotating blade and thus their

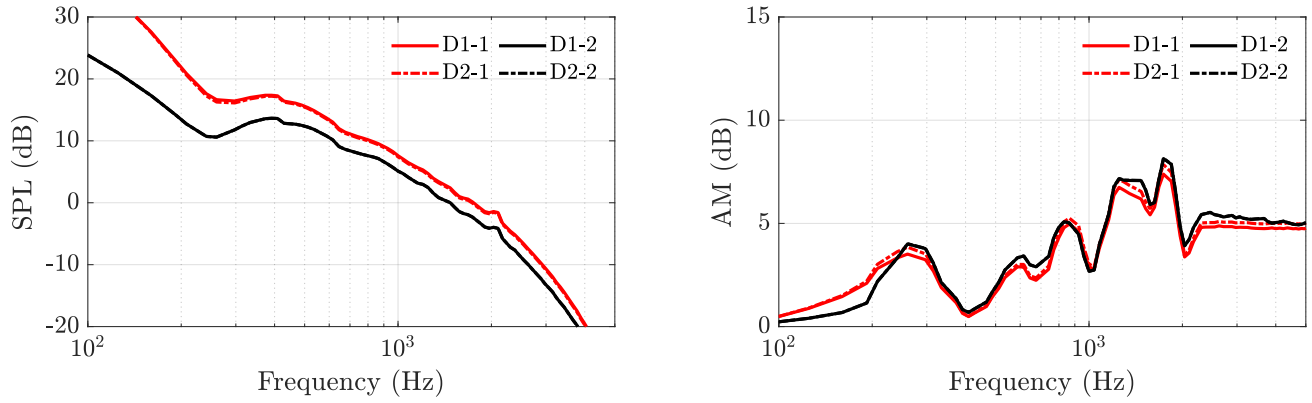

(a) **(b)**

Figure 3.30: Spectra of the (a) Time-averaged SPL and (b) AM of the test cases D which are given in Table 3.6

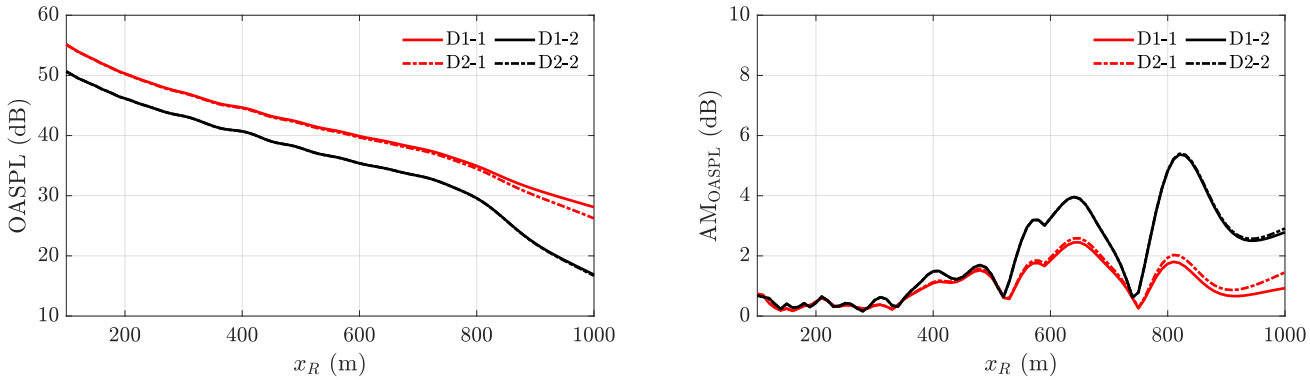

(a) **(b)**

Figure 3.31: (a) OASPL and (b) the modulation of the OASPL of the test cases D given in Table 3.6

contribution is barely modified by the presence of turbulence scattering. The noise from the segments that are outside the shadow zone dominate the generated noise and thus the influence of scattering due to turbulence is low. Correspondingly, the higher OASPL for Cases D1-1 and D2-1 (Fig. 3.31a) is attributed solely due to the turbulence at the source. However, the cases with the higher turbulence D1-1 and D2-1 show lower AM_{OASPL}. This is because for a high level of turbulence, the TIN dominates the overall spectra of the observed noise and so there is less contribution of the modulation of the TEN. As observed until now, the limits of the shadow zone are crucial for the level of AM upwind. We finally investigate this influence by extending the distance x_R away from the wind turbine in the next set of test cases.

3.9.5 E: Shadow zone

We synthesize again two cases similar to case A2-3 with a moderate turbulence but at different distances x_R while the rest of the parameters remain the same. These test cases are described in Table 3.7.

Cases	x_R(m)	Signal [1] (.wav file)
E1-1	800	E1-1
E1-2	1000	E1-2

Table 3.7: Test cases E: downwind ($\theta = 180°$), wind shear exponent α=0.3, medium turbulence and grass ground in summer.

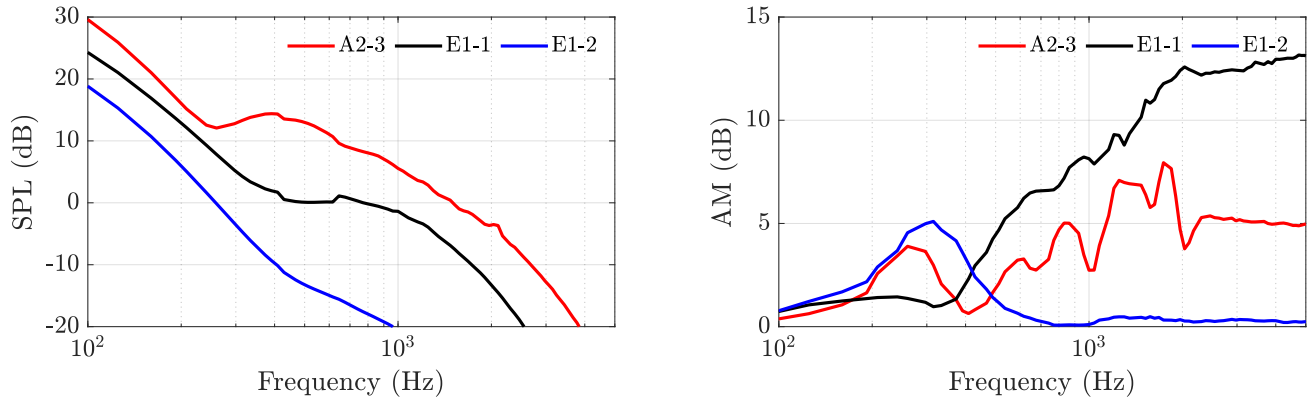

(a) **(b)**

Figure 3.32: Spectra of the (a) Time-averaged SPL and (b) AM of the test cases E which are given in Table 3.7

The influence of the distance on the SPL is clearly seen in Fig. 3.32a. The level of the SPL is seen to decrease as the distance from the wind turbine is increased, as is expected. However, the level of the AM as in Fig. 3.32b does not have the same relation with respect to the distance. The level of the AM for the receiver with the shortest distance (A2-3) is seen to be intermediate between the cases E1-1,2. This is because for the case A2-3, the receiver is outside the shadow zone for most of the sources above the height of 80m as can be seen in Fig. 2.19. On the other hand it can be seen that for the case E1-1 (Fig. 2.20a), the receiver is already in the shadow zone for a source height of 80 m, so the moving blade produces AM even in the higher frequencies. For the case E1-2, the receiver remains in the shadow zone for of frequencies above 300Hz (Fig. 2.20b), while the lower frequencies have a certain contribution to the overall AM. For these cases, the decrease in the level can

be heard along with the corresponding change in the AM as mentioned above. The decrease in the SPL as the receiver position is further away from the wind turbine is obvious while the evolution of AM is more complex and can be understood only if the evolution of the shadow zone limit with segment height is known.

3.10 Conclusion

The synthesis tool presented here converts the frequency-domain model into a time signal for wind turbine noise. The response from each segment of the blade at every angular transition is synthesized individually as grains and arranged according to their corresponding propagation time. The window function developed for the cross fading between two successive grains enables us to obtain a smoother signal. The window function is investigated to find its optimal parameters. A few test cases presented show the final outcome of the wind turbine noise prediction model. From the comparison of the individual test cases, the influence of the propagation effect and the individual parameters on the wind turbine noise can be assessed through the synthesized sounds that are provided. Even with the inclusion of the propagation effect, the characteristic large amplitude modulation of the wind turbine noise crosswind is observed throughout all the studied cases. Among the test cases studied, the effect of the implemented ground parameters and the wind shear seems to produce a significant difference only in the upwind condition. This is attributed to the influence of the parameters on the limits of the shadow zones that are observed due to the different source heights during the blade rotation. The limits of the shadow zone as observed by the receiver upwind for each source height is seen to greatly influence the amount of the amplitude modulation. It is clear that the receiver distance influences the level of amplitude modulation in the upwind direction as it relates to the shadow zones observed from each source height. The effect of the scattering due to turbulence is seen to have a small effect on the synthesized noise. With the inclusion of pre-attained background noise at the correct level, the scattering due to turbulence may possibly be negligible. However, the turbulence effect on the phase and amplitude fluctuation may be important components to be added to the model [75, 4].

Other extraneous sources of noise such as vegetation and background noise can also be added to the synthesized sounds to simulate a realistic environment for a given scenario [13, 92]. The procedure of the auralization for the 3 blades of the wind turbine includes delaying the signal of one blade by the appropriate time. This means that the delayed signals have the identical phase that is repeated and could

be heard as repetitive and artificial. It is possible to add a minimum amount of white noise to the entire signal or to distort the phase of the repeated signal entirely and avoiding correlation.

From an overview of the studied test cases it can be seen that the model predictions are influenced by certain parameters in the propagation modelling. In test cases it can be seen that except for the grass ground in winter, the outcome is nearly the same for the grass ground in summer or the natural ground in summer or winter. The wind shear effectively shifts the spectral content closer or further away from the wind turbine only for orientations close to the upwind direction. The scattering due to turbulence is seen to be small and negligible. Thus a competent wind turbine model is attained with considering the correct orientation of the receiver and the wind shear profile and while approximating the ground parameter to one of two types and justifiably however scintillations associated with time varying turbulence might be audible. This approximation in the wind turbine noise model is necessary to calculate with efficiency the combined effect of multiple wind turbine in a study of a wind farm. We use this approximations for the same reason to compare and validate the developed wind turbine noise model against field measurements in the next chapter.

4

Physical validation

Contents

4.1 Introduction

To understand the validity limits of the wind turbine noise model, calculations need to be compared against field measurements. We avail of the data collected in the framework of the PIBE project (Prévoir l'impact du bruit des éoliennes) [22, 23, 1] and compare them to the predictions of the wind turbine noise model presented in Chapter 2. As the model can be viewed as a combination two parts: the source and the propagation, we compare the individual predictions separately. The measured noise levels averaged over 10 minutes are compared to the model spectra. In order to isolate the influence of the aerodynamic noise source, the comparison of the source model is done at a reference position as defined by the standard IEC 61400-11 (IEC point). The IEC point is located on a rigid platform on the ground, at a distance equal to the sum of the hub height and of the tip radius. The outcome of the wind turbine noise while considering the propagation effects are compared at various acoustic points recorded at various heights between 1.5 m and 2.6m. This chapter begins by mentioning the state of the art in Section 4.2 for similar field measurement comparisons done for wind turbine noise. The experimental campaign of PIBE and

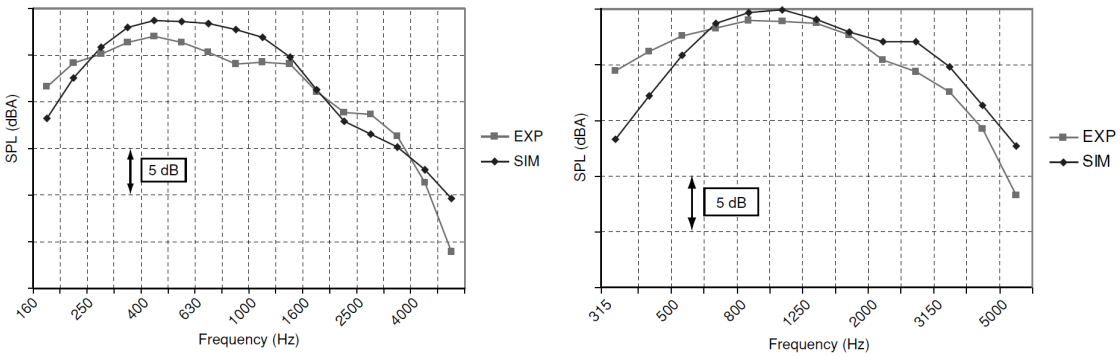

Figure 4.1: The comparison of the predicted noise levels (noted "SIM") and the measurements (noted "EXP") for two different wind turbines [63].

the obtained data [22, 23] are briefly described in Section 4.3. The processing of some of the data obtained during the campaign is explained in Section 4.4. The comparison with the source model is done is Section 4.5 and the comparison of the model inclusive of the propagation effects is shown in Section 4.6.

4.2 State of the art

The literature shows only a few studies that compare predictions models of wind turbine noise to the field measurements. Oerlemans *et al.* [63] compares the prediction done for the trailing edge noise with the measurements taken at the IEC point for two different wind turbines. The prediction of the trailing edge noise is based on the BPM model [16]. The study shows that a good agreement is found between the measured and predicted spectra, in terms of levels and spectral shape (Fig. 4.1).

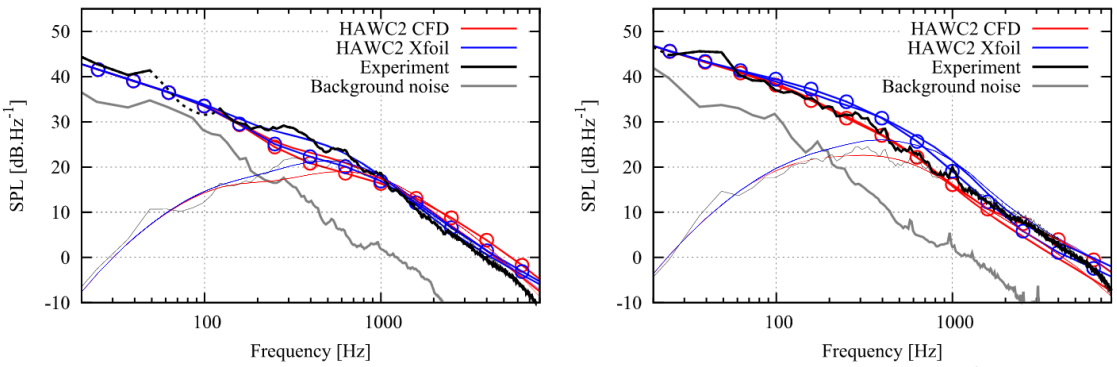

Figure 4.2: The comparison of the predicted noise levels and the experimental observation for the wind speed 5m/s (left) and 10 m/s (right). The red and blue curves correspond to two different prediction methods described by Bertagnolio *et al.* [9].

A study by Bertagnolio *et al.* [9] also compares the source model for trailing edge noise, turbulent inflow noise as well as stall noise to measurements taken at the IEC point for a single wind turbine. The study concludes that the measured levels are well predicted by the source model for two different wind speeds at the hub height (Fig. 4.2). However, both of the studies done consider only one wind turbine at a time and are done close to the wind turbine to minimize the propagation effects.

For the validation of the propagation effects of wind turbine noise, a recent study by Nyborg *et al.* [61] compares three standard propagation models namely the ISO 9613-2 model, the Nord2000 ray tracing model and the WindSTAR-Pro. The prediction is done considering one wind turbine, modelling it as a point source as well as an extended source over 3 heights. The study shows that the models WindSTAR-Pro model based on the Generalized Terrain Parabolic Equation (GTPE) model[7] and the Nord2000 model that is based on a ray tracing method [78] provide good agreement to the measurements for certain cases.

A few studies can be found in the literature that investigates the relationship between the meteorological conditions and the wind turbine noise produced. The studies of van den Berg [91, 90] analyze the stability of the atmosphere with respect to the wind shear and its impact on the propagated wind turbine noise. The categorized atmospheric stability classes corresponding to different ranges of wind shear exponents are given in Table 4.1. It is observed that the increase in wind shear due to atmospheric stability also has a significant effect on the sound emission, resulting in a higher noise impact on neighbouring residences. Oerlemans [62] shows an increase in the wind shear exponent that gives stall noise for high angles of attack which leads to a high level of amplitude modulation, as can be seen in Figure 4.3.

Stability class	Shear exponent range
(very–slightly) unstable	$\alpha \leq 0.1$
(near) neutral	$0.1 < \alpha \leq 0.2$
slightly stable	$0.2 < \alpha \leq 0.4$
(moderately–very) stable	$0.4 < \alpha$

Table 4.1: Stability classes and wind shear exponent α (Taken from [91]).

The scattering due to the turbulence [83] is another factor that influences the level of the noise inside the shadow zone. The level of the scattering depends on the amount of turbulence in the atmosphere (See Section 2.3.3). Muñoz-Esparza *et al.* [60] show that the turbulence dissipation rate ϵ nearer to the ground is around 10 times the turbulence at a height near the hub (Fig. 4.4). This difference in the turbulence may influence the level of the scattering in the shadow zone.

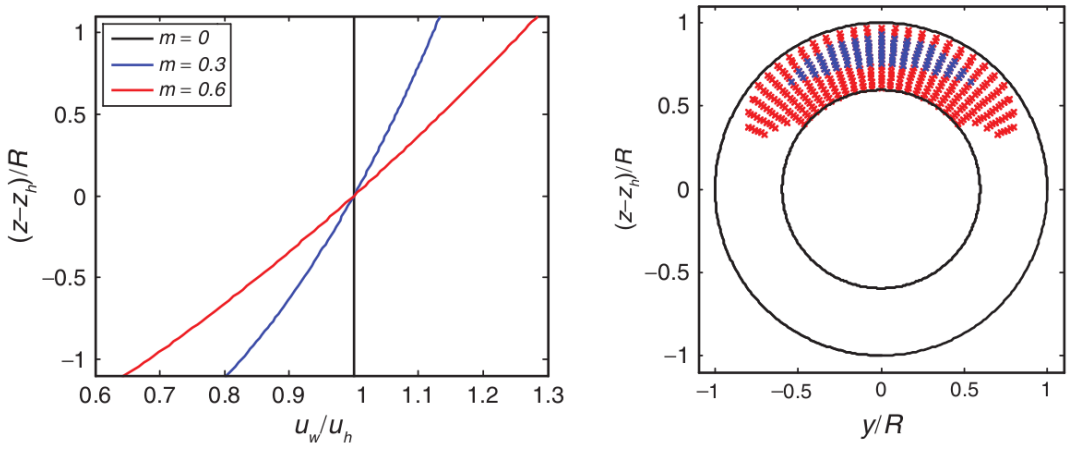

Figure 4.3: The studied wind shear exponent as m (left) and the positions on the rotor plane here stall noise occurs (right) [62].

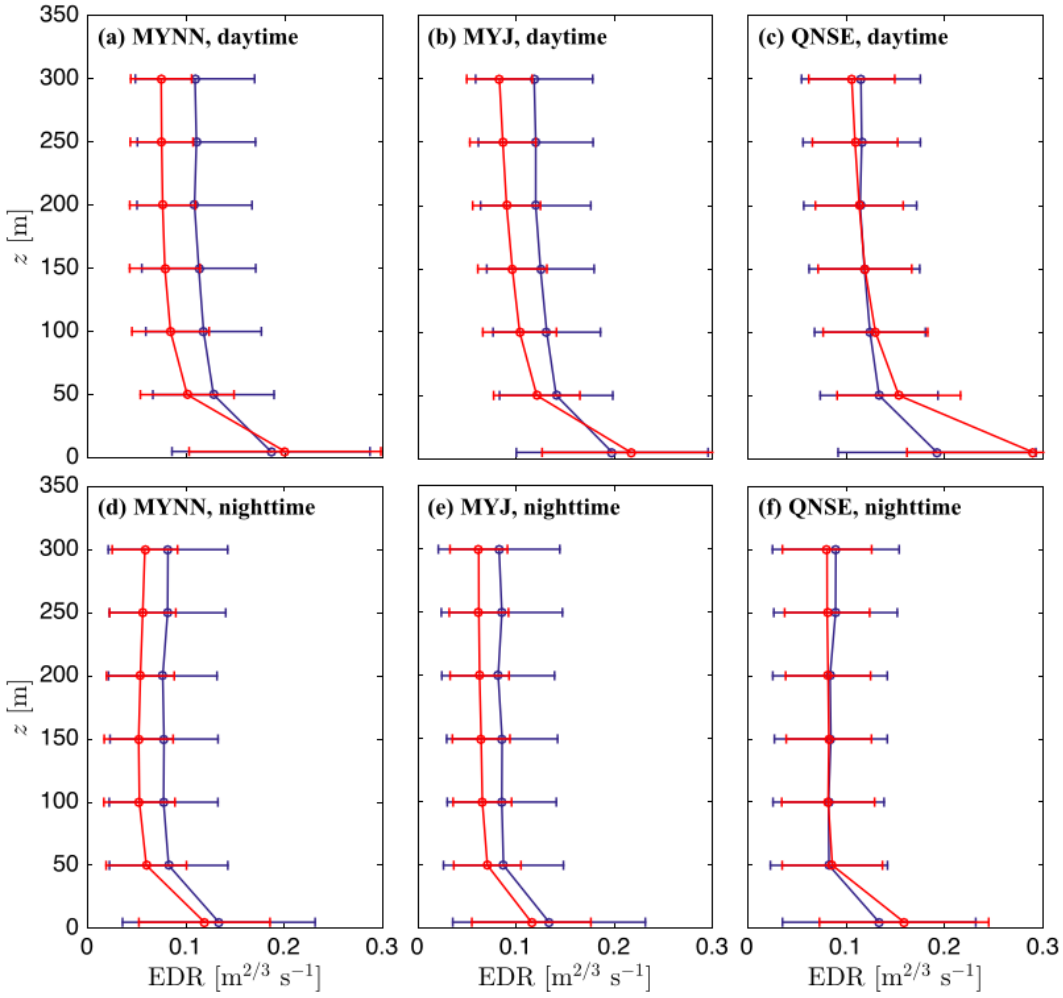

Figure 4.4: Evolution of the energy dissipation rate (EDR = $\epsilon^{1/3}$) with respect to height measured at various locations (noted MYNN, MYJ, QNSE) during the day or the night [60].

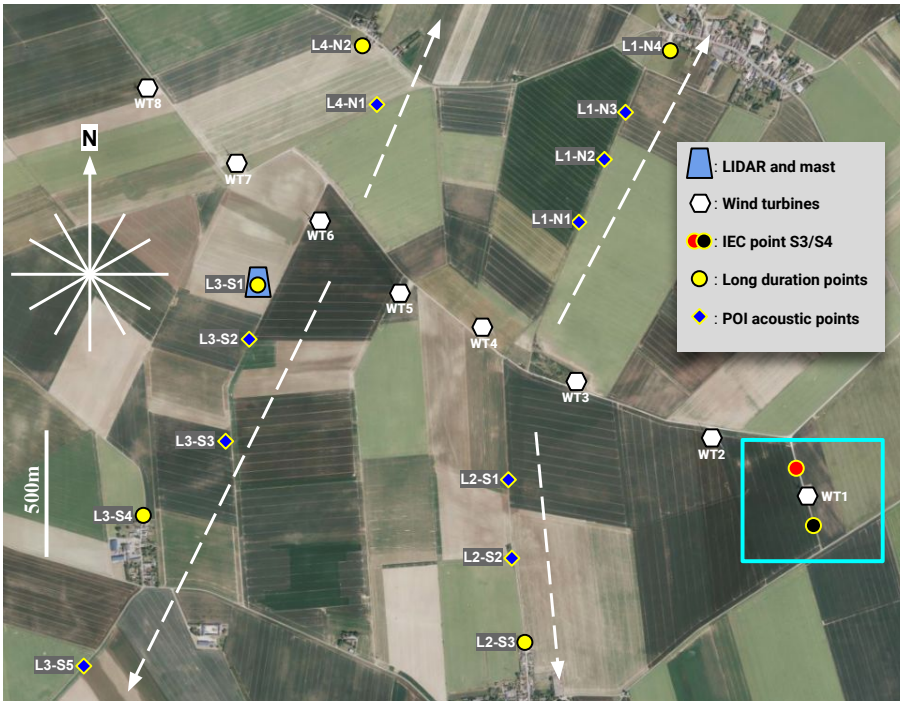

Figure 4.5: Site map of the studied wind farm. The wind turbine WT1 and IEC points in the highlighted section can be more clearly seen in Fig. 4.6.

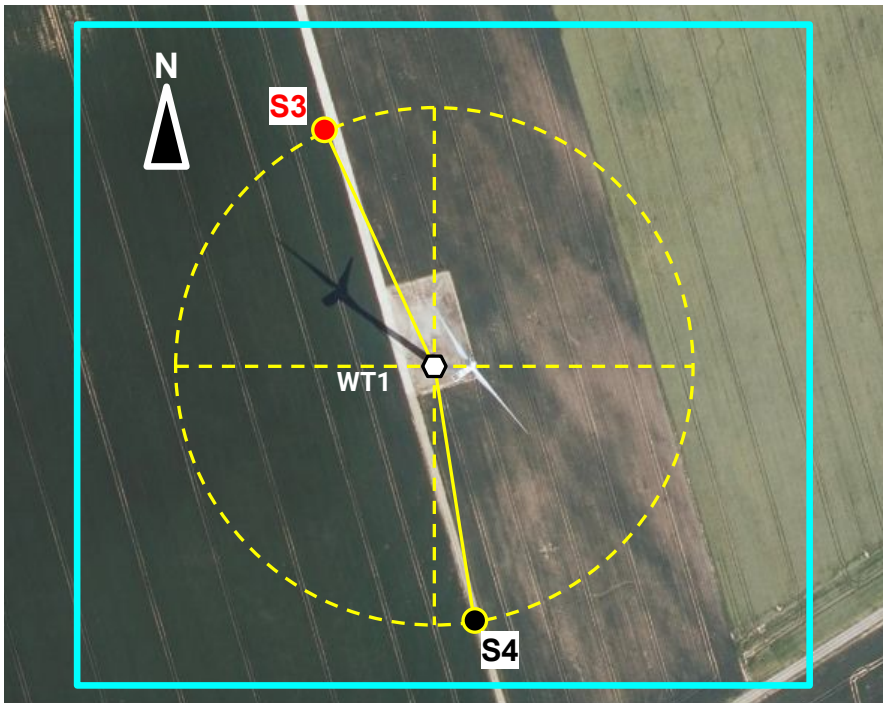

Figure 4.6: Focused map of the studied wind turbine WT1 with respect to the IEC points S3 and S4.

4.3 PIBE Experimental campaign

The PIBE measurement campaign was carried out by the Unité Mixte de Recherche en Acoustique Environnementale (UMRAE) with teams from CEREMA and l'Université Gustave Eiffel [22, 23, 1]. The wind farm where the campaign was conducted is located near the center of France and is composed of 8 wind turbines of 3MW nominal electrical power each with a rotor diameter 90m and a hub height of 80m (Fig. 4.5-4.6). The wind turbines are positioned almost linearly at an angle of around 60° with respect to North and are named WT1 to WT8 from right to left. The wind farm location was a flat site with the altitude gradient differing less than 1% over 3km. The long term campaign (LT) was carried out over 410 days (February 2020 to April 2021) within which the first period of intensive observation (POI) on this wind farm was carried out for 10 days from 23-06-2020 to 02-07-2020. We focus only on the POI campaign and describe all the relevant data obtained during this time.

Figure 4.7: The meteorological mast with multiple sensors at different heights and the location of the LIDAR highlighted (left). The LIDAR (Zephir ZX300) in red focus, fitted with the local weather data logger in green focus (right).

A mast of 80m fitted with multiple sensors along with a LIDAR recorded meteorological data at different heights (Fig. 4.7). The mast is located next to the acoustic point L3-S1 as can be seen in Fig. 4.5, approximately 330m from WT6. Below are the data recorded by the LIDAR and the meteorological mast:

1. LIDAR:
   - Air temperature (°C), atmospheric pressure (mbar), humidity (%), rain (mm) recorded at 1.2m at around 3 to 4 samples per minute.
   - Wind direction (°), horizontal wind speed (m/s), vertical wind speed (m/s) recorded at 185m, 165m, 145m, 130m, 115m, 100m, 85m, 70m, 55m, 40m, 39m at around 3 to 4 samples per minute.
2. Meteorological mast data:
   - Wind speed (m/s) at 80m, 75m and 35m, wind direction (°) at 80m and 70m, temperature (°C) and humidity (%) at 78m, 60m, 20m and 6m, sampled at 10 min intervals.

Three 3D ultrasonic anemometer with sampling frequency of 20Hz mounted on the mast at 10m, 50m and 80m gave the wind speed for the three directions as well as the virtual temperature. The data from the anemometers were processed to obtain the data on the atmospheric turbulence. However, for the POI campaign only the anemometer at 80m was functional. The data from the wind farm known as Supervisory Control and Data Acquisition (SCADA) was also acquired to understand the functioning of the wind turbines. The SCADA data over 10 minute periods, provided the RPM and active power for each wind turbine along with the wind speed and wind direction at 80m at the location of each wind turbine. For the duration of the POI campaign, the SCADA data shows that the wind turbines were functional with no periods of inactivity. As a result, it has not been possible to identify periods of background noise from this database. The ground impedance was measured at different locations around the wind farm using the two-microphone method [28, 35, 23] to give information on the type of ground during the campaign (See Appendix C).

The acoustic data recorded at the two IEC points (S3 and S4) are at a distance of 125 m from the base of the wind turbine WT1 (Fig. 4.6). In accordance with IEC 61400-11 recommendations, the microphone was placed on the ground in the centre of a circular reflective plate of 1m diameter, equipped with two windscreens of 9cm and 50cm diameter (Fig. 4.8). The acquired data was the sound level in the third octave bands measured for every 10-minute intervals. The IEC point S3 was at an

Figure 4.8: Left: The installation of the microphone at the IEC point on the ground in the centre of a circular reflective plate of 1m diameter. The installed wind screen of diameter 9cm can be seen. Right: The installed IEC point S3 with the wind screen of diameter 50cm.

angle of 26° and S4 at an angle of -171° relative to the North direction. Since the IEC point is on the ground and relatively close to the wind turbine, the influence of the ground and propagation effects are minimized as only the atmospheric absorption is influential mainly at high frequencies.

The sonometers used during the long term campaign are placed at a height of 1.5m except point L4-N2 that is placed at a height of 2.6m due to the presence of a wall (Fig. 4.5). The ten sonometers used for the POI campaign are placed at a height of 2m and are distributed along four lines with distances ranging from 330m to 1890m from the closest wind turbine (Fig. 4.9). Table 4.2 shows the distance between each pair of wind turbine and acoustic point. The acoustic points are named as L1-Ax, L2-Ax, L3-Ax and L4-Ax, where A is N for North or S for South with respect to the line of the wind turbines and x is the receiver number with respect to the nearest wind turbine (Fig. 4.5). The recorded data at these points, including the IEC points were in the form of third octave bands measured in 10 or 1 minute intervals. Each sonometer recorded the $L_{Z,100ms}$, $L_{A,100ms}$ and also L_{100ms} of third octave bands with center frequencies from 6.3Hz to 20000 Hz. The sonometers L3-S1, L4-N2, L1-N4, L2-S3 and L3-S4 of the long term campaign each had a meteorological data logger attached to them close to the height of the microphone. The attached meteorological data logger recorded the wind speed, wind direction, relative humidity, temperature, atmospheric pressure and rain sampled at 1 Hz.

The data collected in the duration of the POI need to be post-processed to

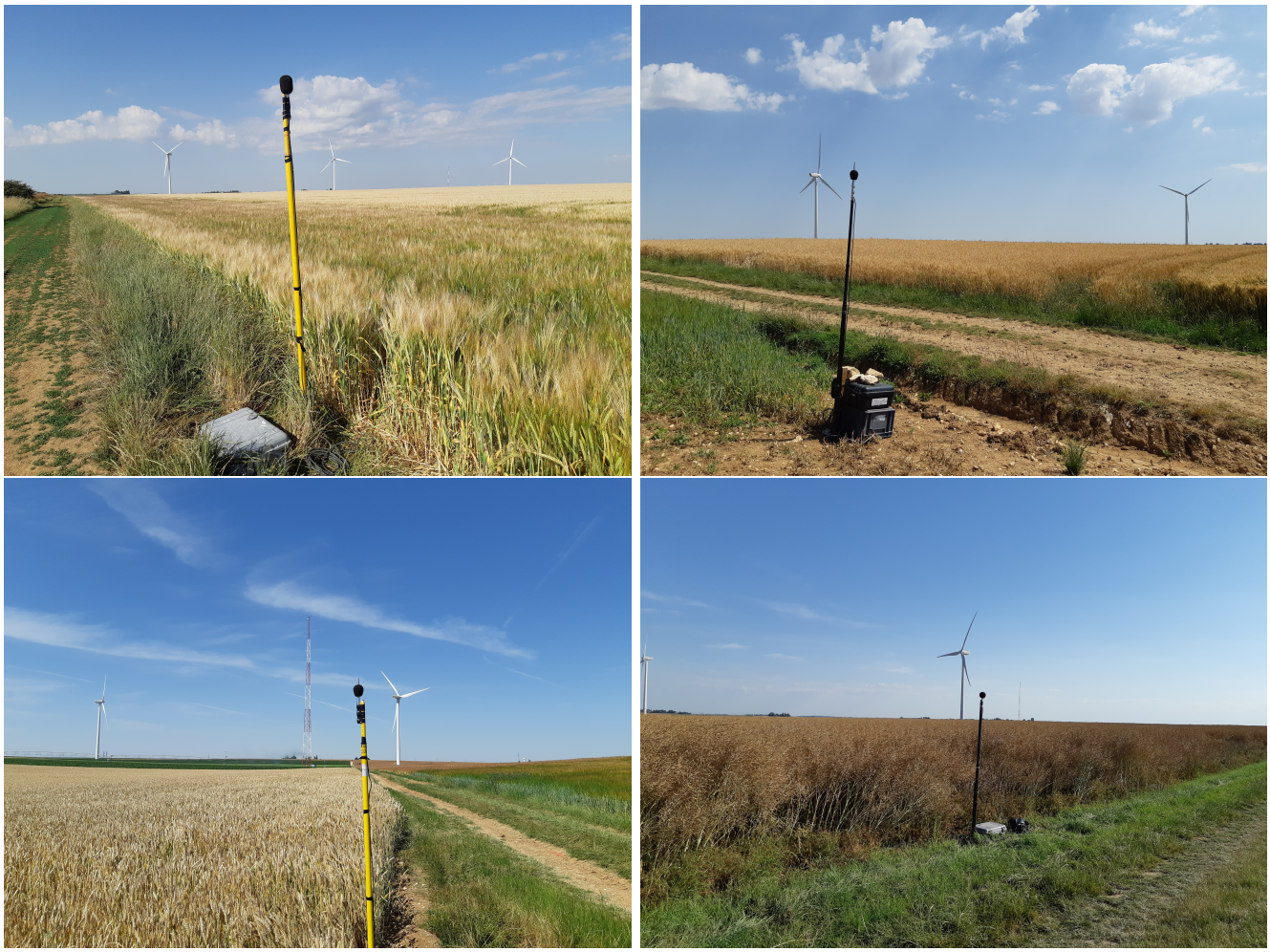

Figure 4.9: The installed sonometers at a height of 2m. The difference in the surrounding grounds can be clearly seen. From top left, clockwise: L1-N3, L2-S1, L3-S2, L4-N1.

be used for comparison against the model. A few details on the synchronization, calibration and necessary parameters that are derived from the recorded data are described in the next section. The processing of the data was done in part during a secondment visit at CEREMA in Strasbourg under the supervision of David Ecotière.

4.4 Data processing

The data collected from the campaign occasionally contains some erroneous values which are due to certain unexpected reasons. This is anticipated for an experimental campaign and thus requires the data to be cleansed of the false values and organized to obtain valuable information.

Acoustic point	WT1	WT2	WT3	WT4	WT5	WT6	WT7	WT8
L1-N1	1403	1010	609	530	736	1023	1372	1800
L1-N2	1506	1140	806	738	901	1127	1436	1839
L1-N3	1690	1360	1088	1021	1144	1301	1555	1916
L1-N4	1839	1553	1354	1318	1437	1565	1783	2109
L2-S1	1202	861	543	664	892	1296	1692	2138
L2-S2	1206	945	780	946	1160	1548	1934	2371
L2-S3	1285	1121	1079	1272	1476	1852	2227	2654
L3-S1	2310	1892	1320	899	553	334	516	909
L3-S2	2322	1916	1361	976	675	572	736	1078
L3-S3	2329	1948	1434	1115	887	885	1059	1365
L3-S4	2670	2322	1858	1588	1388	1372	1472	1684
L3-S5	2934	2636	2244	2042	1891	1916	2021	2208
L4-N1	2325	1909	1379	989	748	506	563	896
L4-N2	2527	2119	1609	1236	1008	743	677	883

Table 4.2: Distance in meters between the acoustic points and the wind turbines. The closest distances are highlighted in red.

The wind speed and wind direction values in the data of the LIDAR were limited between 0 to 99m/s and 0 to 360° for all heights while values above that were not considered. For the ultrasonic anemometer data, the values of directional wind speed whose absolute values were above 30m/s were removed. Similarly, the wind speeds above 30 m/s recorded on the meteorological mast as well as the wind turbines (SCADA) were not considered. It has to be noted here that the wind direction recorded for the wind turbine WT5 is wrong when compared to the other wind turbines and had to be manually calibrated (20°-Wind direction). The LIDAR is seen to have no fixed sampling frequency with around 3 to 4 samples per minute. For the analysis, the data from the LIDAR was averaged over 1 minute and then down-sampled to have 1 sample per 10 minutes.

It is also observed that the recorded meteorological as well as acoustic data was not synchronized. The unsynchronized meteorological data was observed by comparing the wind speeds obtained from the LIDAR at 85m, SCADA data of WT6 at hub height 80m, the sonic data of S3 at 80 m and the mast data at 80m with a difference of 2 hours (Fig. 4.10). This unsynchronized data was also observed for the recorded acoustic data of the sonometer. It was noticed via its attached meteorological data logger that the data was recorded with the local time stamp and the rest of the instruments was recorded with the UTC time stamp (Fig. 4.10). To synchronize all the data, it was found to be technically easier to shift the data of the LIDAR, mast and SCADA into the local time (UTC+2 hrs) to the reference of the sonometers and sonic anemometers. The synchronized data was then further

used for the analysis. Fig. 4.11 shows that the wind speed measured by all sensors overlap relatively well except the one measured on WT6. This can be explained by the fact that WT6 is located 330m from the other sensors, and that the anemometer located on the wind turbine hub is less accurate due to blockage effects.

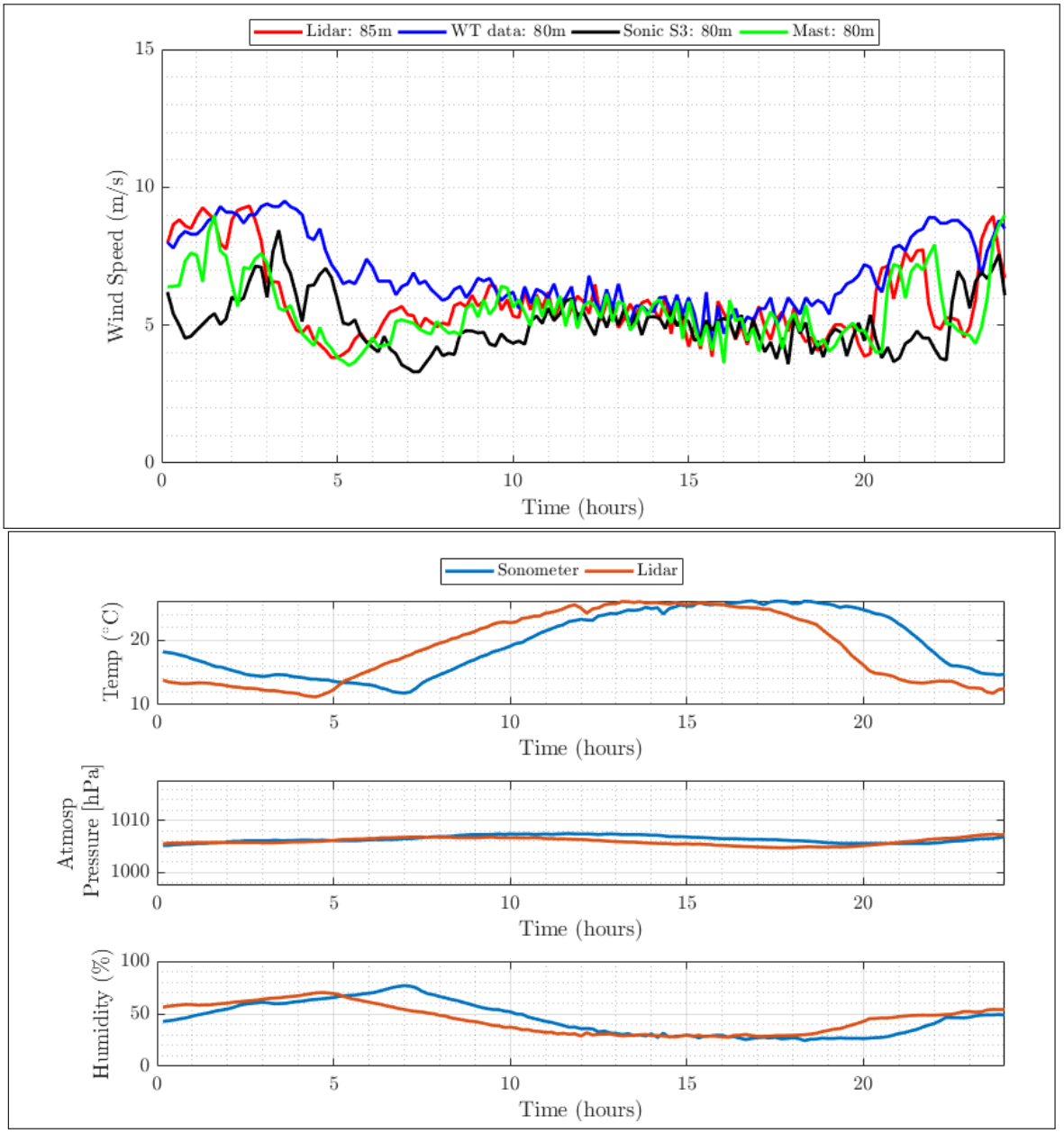

Figure 4.10: The unprocessed meteorological data for 21 July 2020 comparing the wind speed (top) and the recorded data corresponding to the sonometer compared to the data from the LIDAR (bottom).

The wind direction obtained from the LIDAR, sonic-anemometer, meteorological mast and the wind turbine data was observed to have constant differences in the wind direction (Fig 4.12). This is possibly because the instruments were not

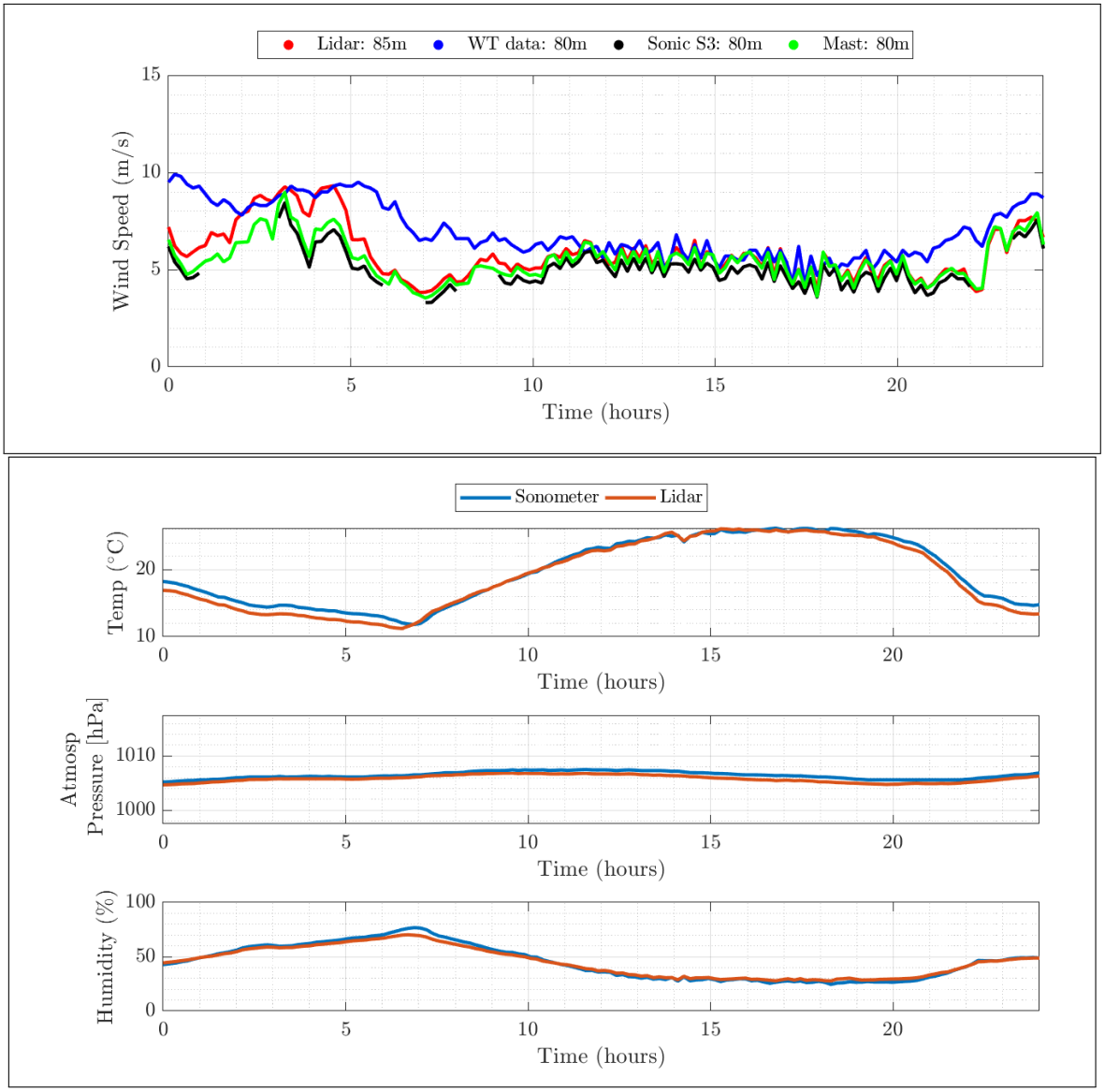

Figure 4.11: The synchronized meteorological data for 21 July 2020 for the wind speed (top) and synchronized data corresponding to the sonometer and the LIDAR (bottom).

calibrated with the reference of the north and with each other. It was concluded that LIDAR data for the wind direction needs to be shifted by +40°. This corrected wind direction from LIDAR is considered as a reference in the following analysis. As the LIDAR provided the wind speed at multiple heights, we avail of this to compute the wind shear profile in terms of log profile parameters as explained next.

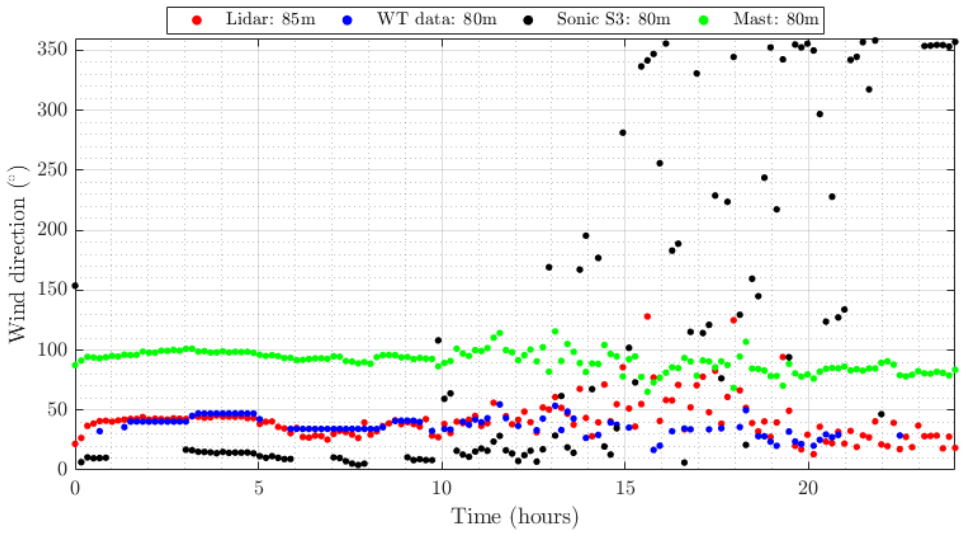

Figure 4.12: The wind direction for 21 July 2020 recorded by the LIDAR at 85m, SCADA data of WT6 at hub height 80m, the sonic data of S3 at 80 m and the mast data at 80m.

Wind shear

The wind shear is calculated from the wind speeds at 7 heights covering the typical rotor plane of the wind turbine from 40m to 130m. The wind profile is assumed to follow the power law profile and the wind shear coefficient α is calculated with reference to the wind speed U_{ref} at height z_{ref} as:

$$\alpha = \frac{\log[U(z)/U_{ref}]}{\log[z/z_{ref}]}, \tag{4.1}$$

where $U(z)$ corresponds to the wind speed at height z. To obtain one value of the wind shear corresponding to all heights, a least-square curve fitting technique was implemented with the reference wind speed U_{ref} obtained from the LIDAR data at a height of z_{ref}=85m. To avoid spurious results of the wind shear an arbitrary choice was made to not consider the values whose residue of the squares correspond to less than 0.6.

Turbulence dissipation rate

An important input parameter required for the calculation of the TIN is the turbulent dissipation rate (TDR) ϵ. The horizontal wind speed $u(t)$ and wind direction was calculated from the x-y components of the wind speed. The mean wind speed U and wind direction is obtained from the average over 10 minutes. The horizontal wind speed fluctuations computed as $u'(t) = u(t) - U$ are used to calculate the 1-D

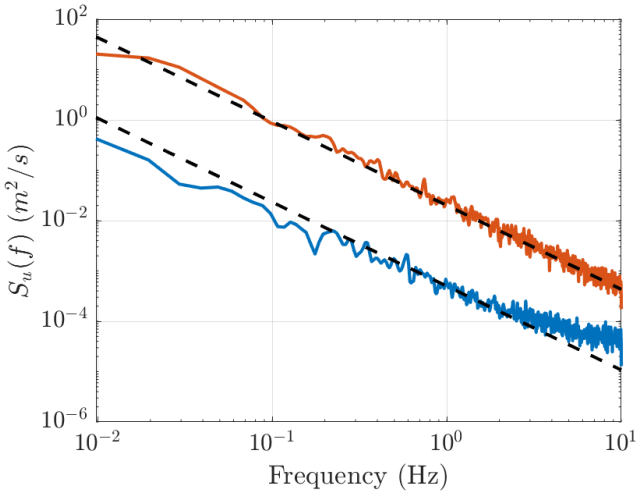

Figure 4.13: The PSD of the horizontal wind speed fluctuations u'. The comparison between the acceptable data (orange) and the unaccepted data (blue). The dashed lines correspond to the expected slope of $f^{-5/3}$.

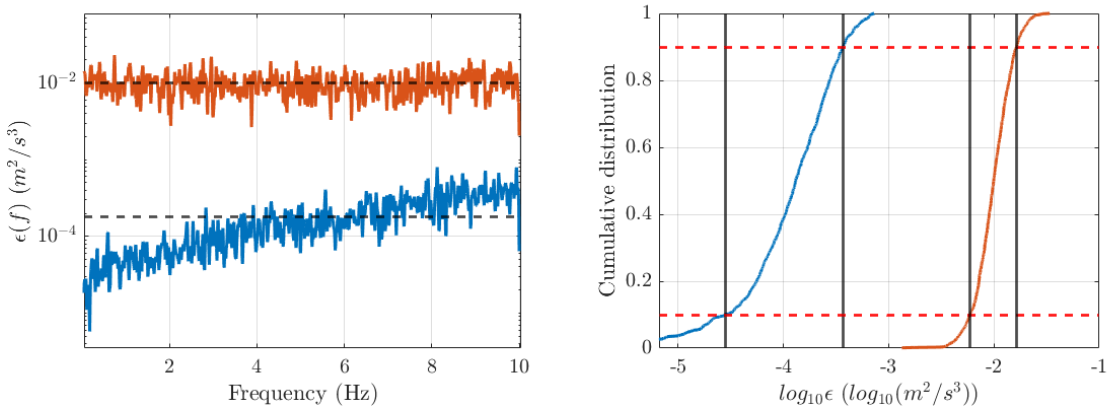

Figure 4.14: The turbulent dissipation rate (TDR) over all frequencies (left) and the cumulative distribution of the turbulent dissipation rate in the logarithmic scale (right). The comparison between the considered data (orange) and the not considered data (blue).

power spectral density (PSD) $S_u(f)$. Following Muñoz-Esparza *et al.* [60], the TDR is calculated as:

$$\epsilon = \frac{2\pi}{U}\left[\frac{S_u(f)f^{5/3}}{K}\right]^{3/2}. \tag{4.2}$$

The Welch method is used to compute the PSD $S_u(f)$ using a 60s window with a 50% overlap every 10 minutes. The typical slope of the $S_u(f)$ is expected to follow the theoretical slope of $f^{-5/3}$ which would give the correct value of $\epsilon(f)$ (Fig. 4.13). The TDR $\epsilon(f)$ is calculated for all the values of f and then averaged to obtain a mean

value of ϵ per 10 minutes. It is observed that the $S_u(f)$ for certain time segments did not follow the expected slope of $f^{-5/3}$ with a corresponding value of ϵ that may not be correct. To quantify this deviation from the expected slope, the empirical cumulative distribution of $\log_{10}(\epsilon(f))$ is taken and the distribution between 10% to 90% is considered. An arbitrary choice is made to disregard the computed value of ϵ if the difference between the 10% and 90% of the distribution of $\log_{10}(\epsilon(f))$ is greater than 0.6 (Fig. 4.14).

Finalized data used

The data base obtained for the POI campaign is relatively large. For consistency and clarity we consider the data obtained only from a few selected devices for the considered days. The meteorological and SCADA data along with the acoustic data are all converted to samples averaged over 10 minutes for the analysis of the 10 days. The finalized data used as input parameters for the model are the following:

- Wind speed (m/s) recorded by LIDAR at 85 m, see Fig. 4.15.
- Wind direction (deg) recorded by LIDAR at 85 m, see Fig. 4.16.
- Wind shear with reference height at 85 m derived from LIDAR data, see Fig. 4.17.
- Turbulence dissipation rate ϵ (m^2/s^3) at 80 m derived from the ultrasonic anemometer data, see Fig. 4.18.
- Temperature $°C$ and relative humidity (%) recorded on the meteorological mast at 6 m, see Fig. 4.19 and 4.20.
- RPM data of each wind turbine from SCADA data, see Fig. 4.21.
- Ground impedance parameters $\sigma(kNs/m^4)$ & e (m) provided by the teams of UMRAE, see Appendix C.

From Figs. 4.15 to 4.21 the data are plotted from 23-06-2020 00H00 to 02-07-2020 23H59. It has to be mentioned that the temperature profile is not considered while accounting for the refraction effect. The comparison of the source model is done in Section 4.5 and the comparison of the model inclusive of the propagation modelling is done in Section 4.6.

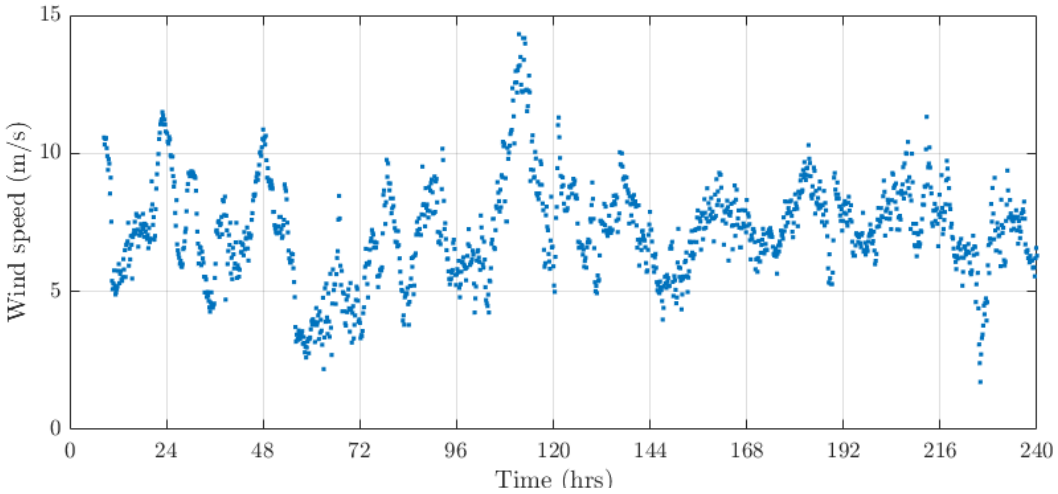

Figure 4.15: The wind speed recorded by the LIDAR at the height of 85m.

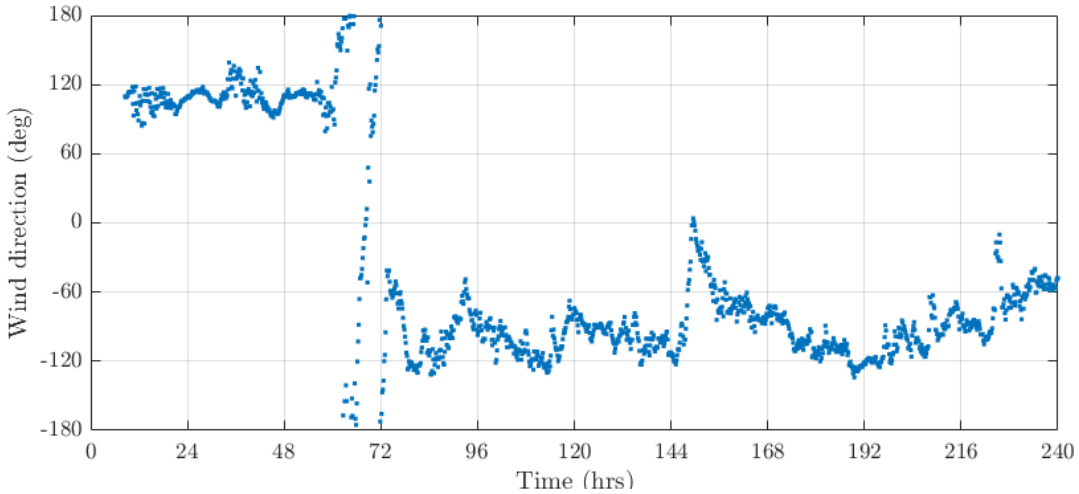

Figure 4.16: The wind direction recorded by the LIDAR at the height of 85m.

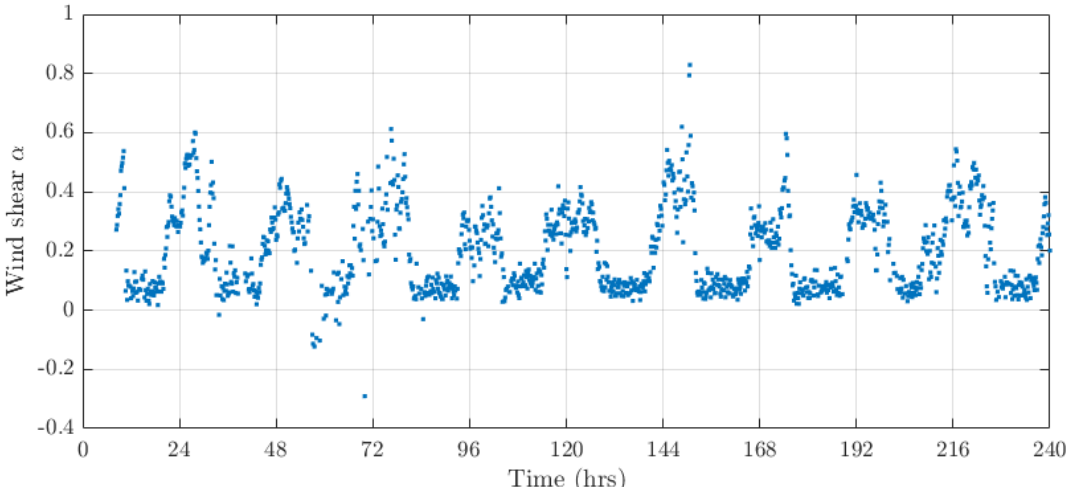

Figure 4.17: The wind shear calculated by the LIDAR data with the reference height at 85m.

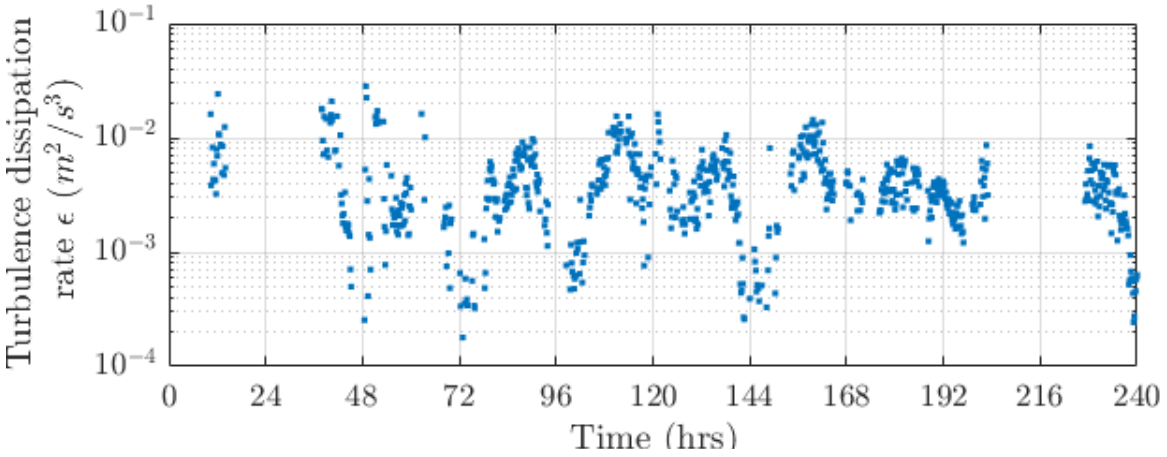

Figure 4.18: The turbulence dissipation rate processed from the sonic anemometer at the height of 80m on the mast.

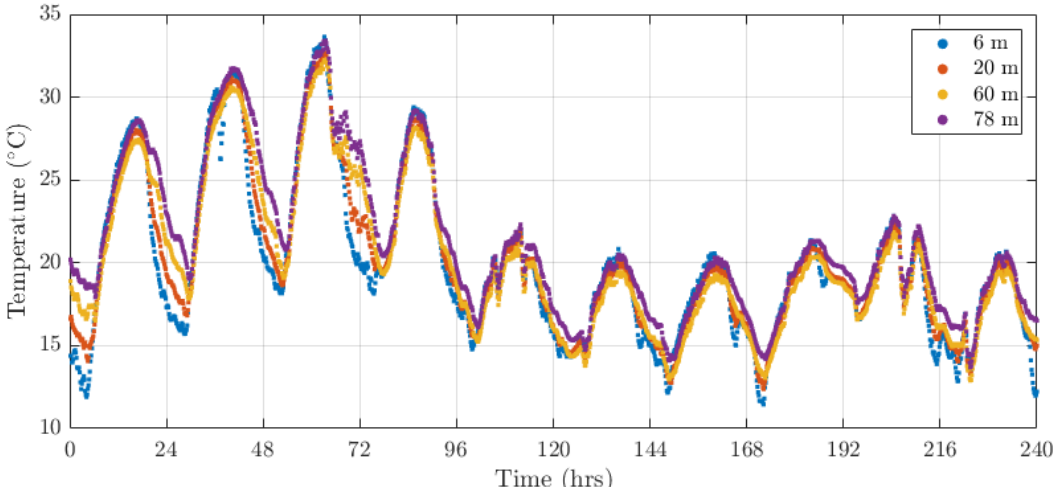

Figure 4.19: The temperature recorded at different heights on the meteorological mast.

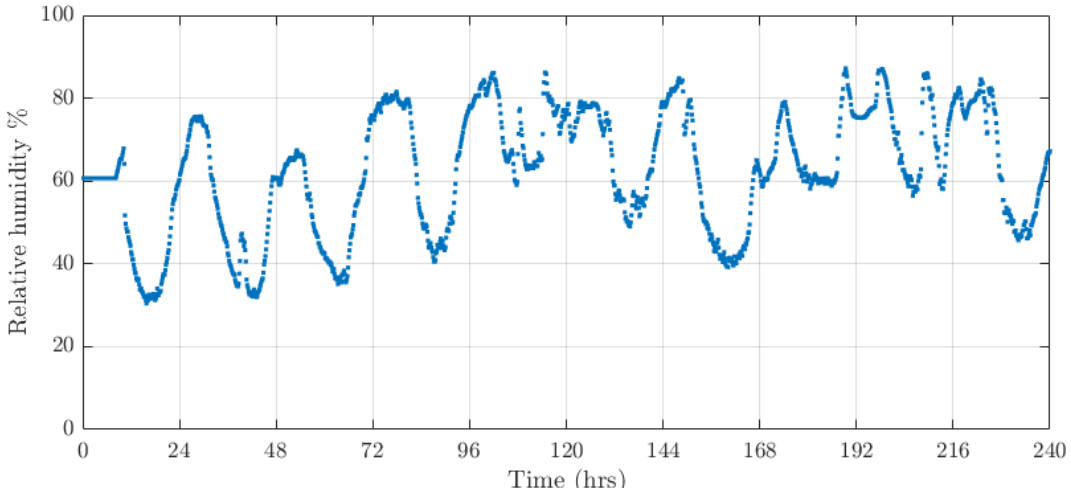

Figure 4.20: The relative humidity recorded on the meteorological mast at 6 m.

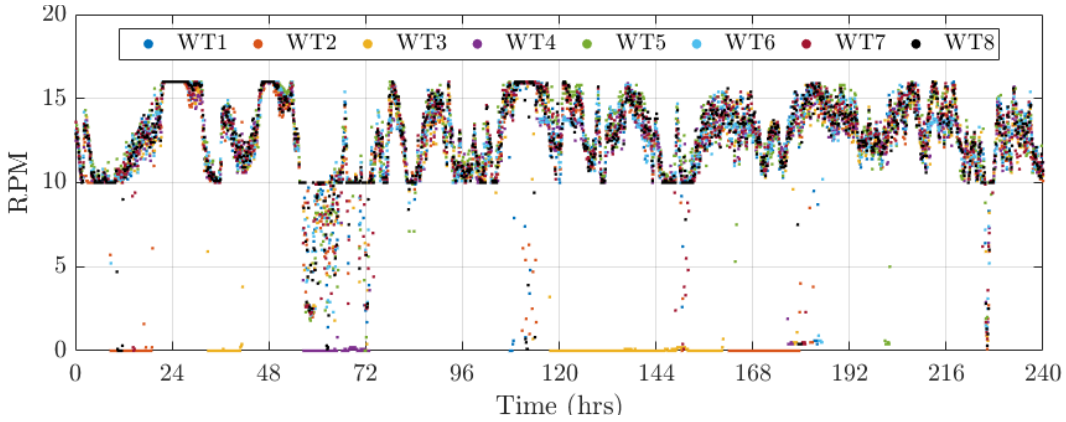

Figure 4.21: The RPM data provided by SCADA for all wind turbines.

4.5 Comparison of the source model

For the comparison of the source model the entire data set is sorted into wind speed and wind direction bins and the noise prediction of the model is done within the limits of these bins for individual cases. The distribution of the wind speed and wind direction bins can be seen in Fig. 4.22. Within a certain bin, the mean values of the relevant data are taken as input parameters for the prediction model. Table 4.3 summarizes a few cases studies and Figs. 4.23 to 4.25 show the corresponding comparison between the model and the field measurements. From Fig. 4.23 to 4.25, the error bars show the standard deviation of the field measurements. The lower curve and upper curve of the shaded area shows the prediction made with the lowest and highest values of the wind speed, ϵ and RPM observed within the respective bin correspondingly.

Case	θ **(deg)**	Wind speed (m/s)	ϵ (m^2/s^3) x10^{-3}	RPM	No. of samples
1 a	-25, -15	7, 8	2.4, 4.5	12.4, 14.9	9
1 b	-25, -15	8, 9	2.9, 4.7	13.1, 15.7	9
2 a	135, 145	6, 7	1.8, 3.1	10.9, 14	11
2 b	135, 145	8, 9	2.4, 6.0	13.1, 15.7	14
3 a	95, 105	7, 8	3.9, 7.6	11.1, 15.5	30
3 b	95, 105	9, 11	4.3, 12.0	13.4, 14.8	12

Table 4.3: Case studies for various wind speed and wind direction bins. The wind speed and wind direction columns shows the minimum and maximum value of the selected bin and the ϵ and RPM columns show the extremities observed within the respective bin.

From the different cases, it can be seen that the noise prediction model is fairly close to the field measurements. Cases 1a and 1b are for the receivers closer

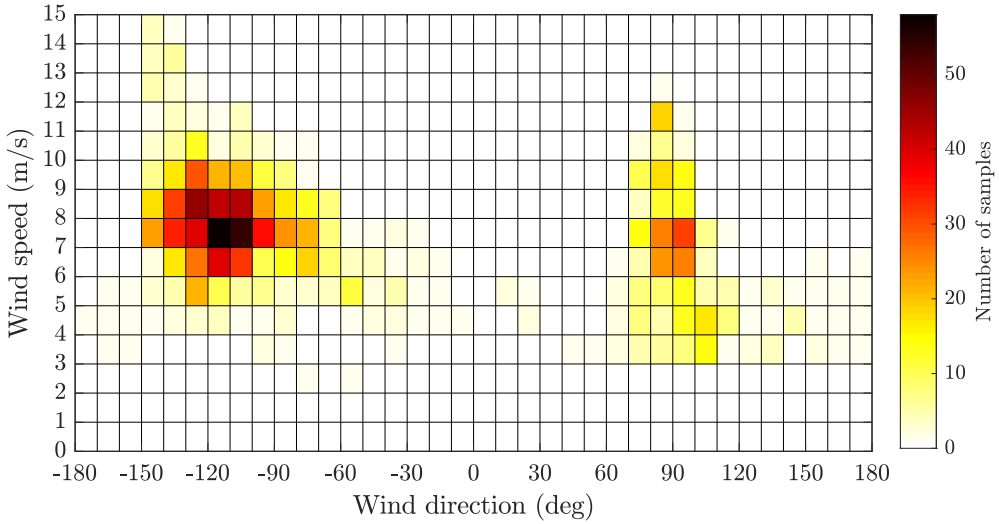

Figure 4.22: The distribution of the wind speed with respect to the wind direction relative to the north direction over 10 days per 10-min intervals, recorded by the LIDAR at the height of 85m.

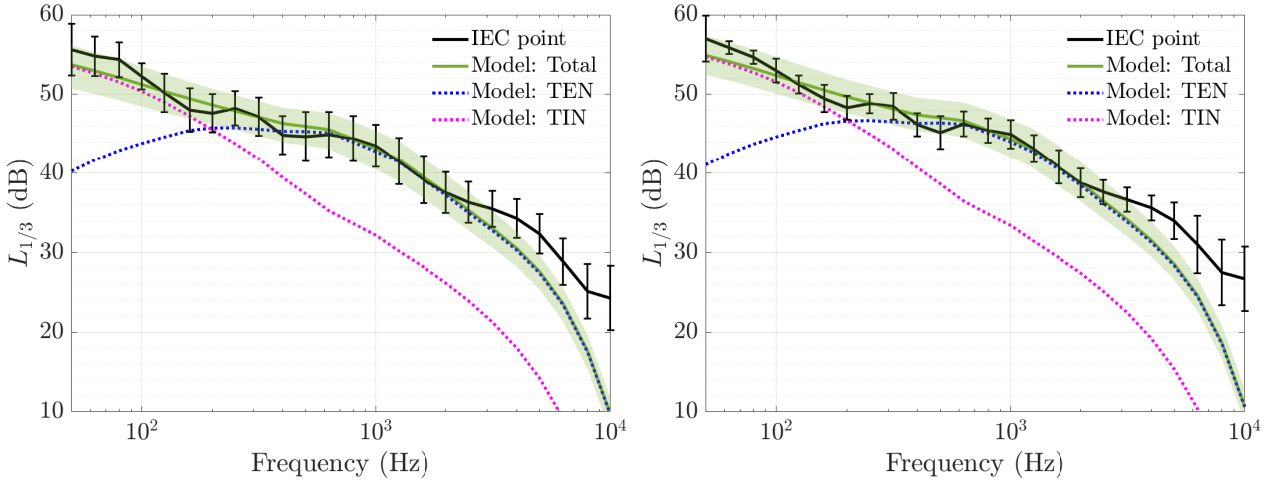

Figure 4.23: Comparison between the prediction model and the field measurements for the receiver orientation θ=-20±5° and the wind speed bin [7,8]m/s on the left and the wind speed bin [8,9]m/s on the right.

to downwind conditions while cases 2a and 2b are for receiver closer to upwind conditions and cases 3a and 3b are for receivers close to cross wind. It can be seen that the extremities of the predictions lie within the error of the standard deviation. The wind turbine WT2 lies at a distance for around 330 m from point S3 and 500 m from point S4. At these distances for certain orientations of WT1, the contribution of WT2 is significant. In particular for crosswind directions, Fig. 4.25 shows that the contribution of WT2 is significant for the levels at lower frequencies with the maximum difference of 4 dB at 50 Hz. It can also be seen in Fig. 4.25 that

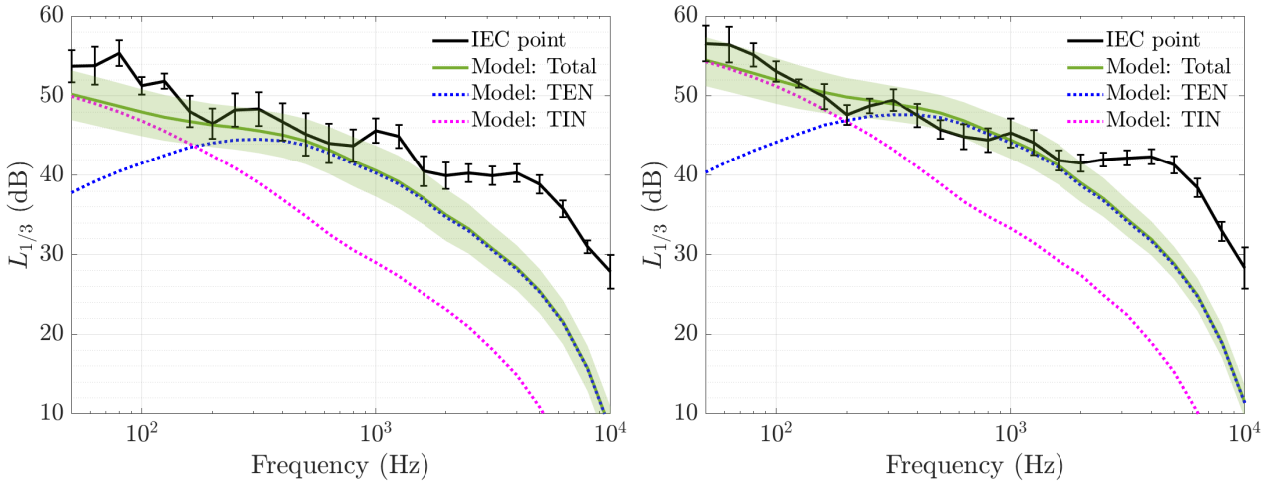

Figure 4.24: Comparison between the prediction model and the field measurements for the receiver orientation θ=140±5° and the wind speed bin [6,7]m/s on the left and the wind speed bin [8,9]m/s on the right.

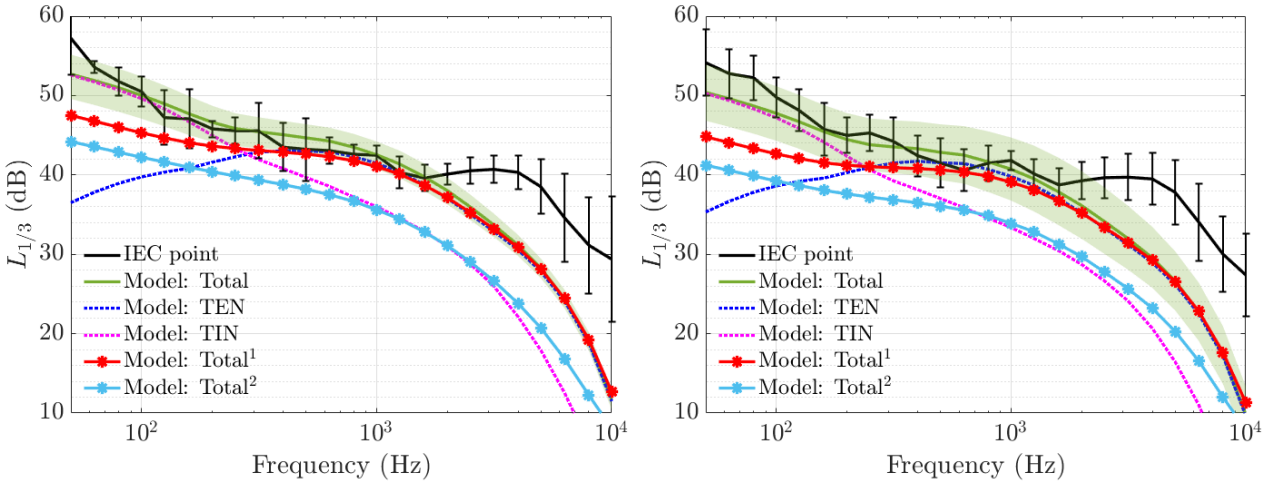

Figure 4.25: Comparison between the prediction model and the field measurements for the receiver orientation θ=100±5° and the wind speed bin [7,8]m/s on the left and the wind speed bin [9,11]m/s on the right. The curve 'Model: Total^1' corresponds to the prediction only with WT1 with the directivity correction, and 'Model: Total^2' corresponds to the prediction of noise from WT1 without the directivity correction.

without considering the directivity correction of $\mathcal{A}$=20% mentioned in Section 2.2.5, the levels are lower for all frequencies with a maximum difference of 6dB around 1 kHz. The frequencies near and above 10 kHz are considered as background noise. The TIN that dominates the lower frequencies is seen to be under-predicted in certain cases because the turbulence dissipation rate is not accurately calculated for the corresponding bin. However, the prominence of the TIN or the TEN at certain orientations of the receiver is well captured by the model. Some peaks around 100Hz and between 2 and 6kHz that are not well predicted may be due to

not accounting for certain noise mechanisms such as stall noise, mechanical noise, blade-tower interaction, tip noise etc. The increase in the SPL with the increase in the wind speed is captured by the model which is evident within each case.

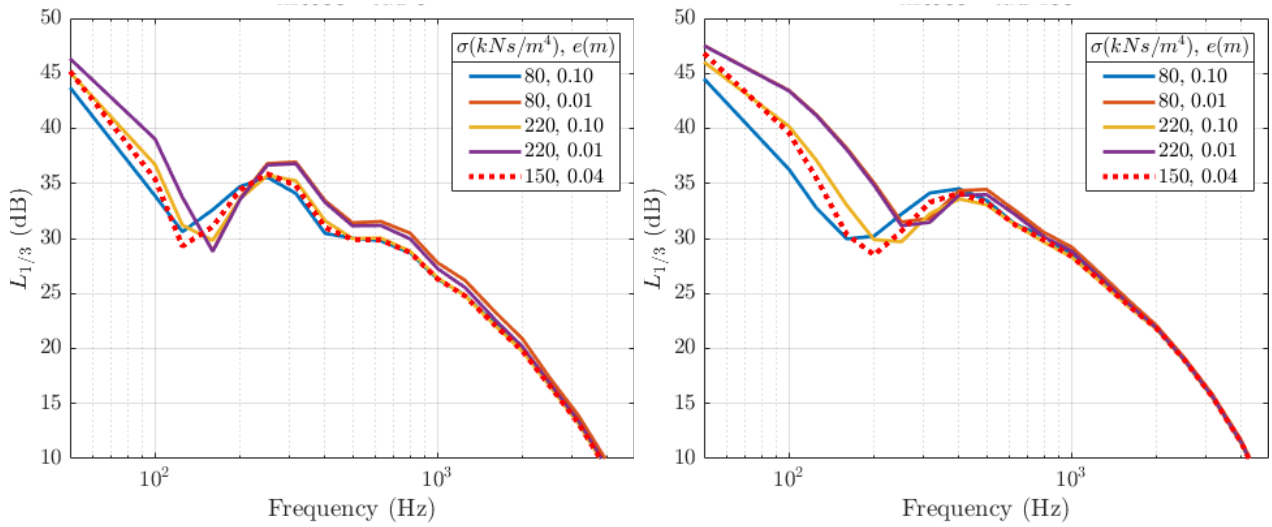

Figure 4.26: The predicted noise with different ground impedance parameters for the receiver at a distance of x_R=500m downwind (left) and upwind (right). The ground parameters are given as σ, e in the legend.

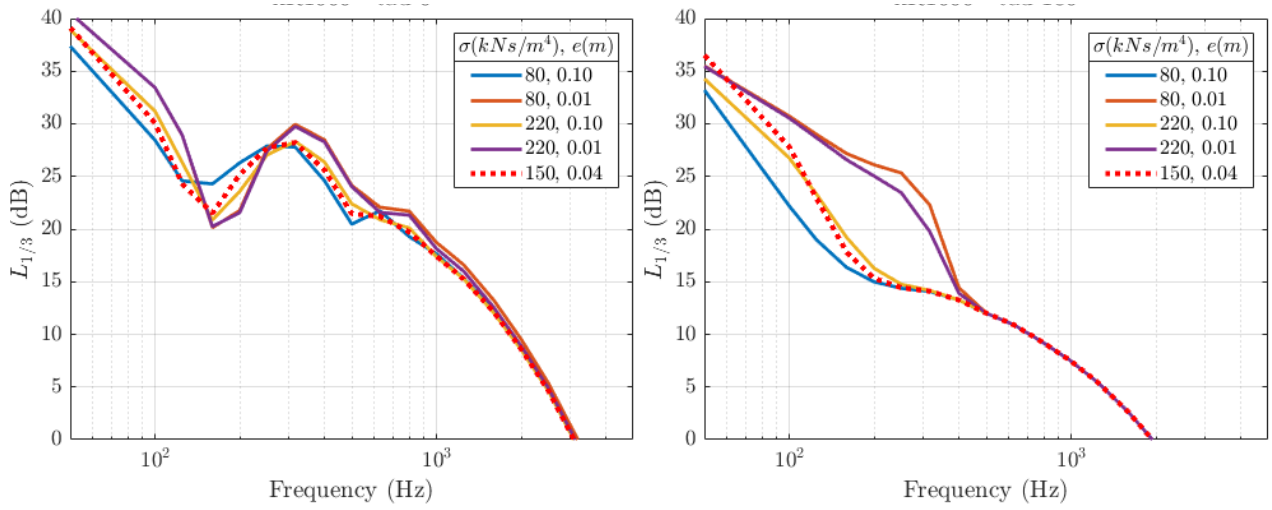

Figure 4.27: The predicted noise with different ground impedance parameters for the receiver at a distance of x_R=1000m downwind (left) and upwind (right). The ground parameters are given as σ, e in the legend.

4.6 Comparison of the source and propagation model

The acoustic data recorded at a particular height and different distances from the wind turbine is found to be sensitive to the prevailing atmospheric condition. Before proceeding to analyse the model, we first study the sensitivity of the model, inclusive of the propagation effects on the input parameters. The ground impedance parameters are observed to be variable (See Appendix C) while the data of the turbulence dissipation rate is sparse (See Fig. 4.18). In the simulation of the propagation model, the ground impedance parameters σ and e used in the Miki model presented in Section 2.3, influence the interference patterns of the received sound. However, the ground parameters estimated during the campaign seem to vary depending on the position of the receiver with $80kNs/m^4 \leq \sigma \leq 220kNs/m^4$ and $1.5cm \leq e \leq 5cm$. The different types of grounds such as "Terre", "Friche", "Jachère", etc. close to the individual receivers can also be seen from the map of the site in Fig. 4.5. A simulation with each individual ground parameter near every receiver position would be computationally expensive and so we analyze the effect of the extremities of the ground parameters on the predicted noise. We do a test case by calculating the noise from a single wind turbine with the rotational speed of $\Omega = 1.47$ rad/s. The wind speed U_{ref}=8m/s is taken at the reference height z_{ref}= 80 m with the wind shear α=0.5. For the calculation of the TIN, the turbulence dissipation rate is taken as $\epsilon = 0.01m^2/s^3$. The comparison of the calculated noise with different ground parameters is done for the upwind and downwind positions as can be seen in Fig. 4.26 at 500 m and Fig. 4.27 at 1000 m. It can be seen from the calculated spectra, the interference frequency and depth are different when the ground parameters vary. The difference is more evident in the predictions upwind and further away from the wind turbine. However, an approximate average of $\sigma = 150kNs/m^4$ and e= 4cm is seen to lie within the extremities of the predicted spectra. These values are taken for the ground impedance parameters in the calculation of the propagation effect for all receiver positions. We are aware that this approximation may yield to uncertainties.

For one receiver point, it is not sufficient to consider the noise contribution from the closest wind turbine. The receiver may be positioned such that it experiences contribution from different wind turbines. For example if the wind direction is 0° North, the receiver L3-S2 is downwind from WT7 but close to crosswind from WT5. Hence for a wind turbine at a distance of around 2 km, it is safe to consider its contribution even if it is small. As an example, we view the receiver point L3-S3

in the time period from 51.5 hrs to 52.5 hrs. In this time, the corresponding mean wind speed at 85 m is 7 m/s (Fig. 4.28) and the mean wind direction at 85 m is 73° (Fig. 4.29). The mean wind shear α =0.3 (Fig. 4.30) and $\epsilon = 5 \times 10^{-3} m^2/s^3$ is taken along with the RPM of the wind turbines (Fig. 4.31) to predict the noise levels at this point. The wind turbines closest to this point are WT6 (885 m) and WT5 (887 m) and WT7 (1059 m). It can be seen from Fig. 4.32 that with the contribution of only the nearest wind turbine, the levels are not predicted correctly. When considering the contribution from neighbouring wind turbines the predicted levels have a difference of around 2dB, while considering all the wind turbines the predicted levels have less than 1 dB difference.

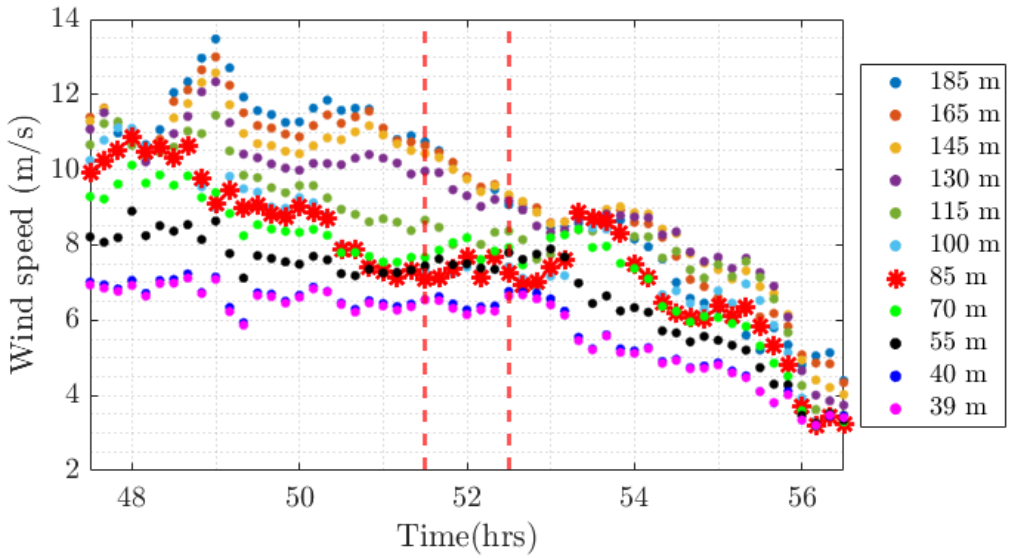

Figure 4.28: The wind speed recorded by the LIDAR for multiple heights for the duration under consideration.

Another important parameter that significantly influences the spectra of the predicted noise is the turbulence dissipation rate ϵ that is used in the calculation of the TIN and also the scattering due to turbulence. However, the turbulence dissipation rate calculated from the data of the sonic anemometer on the mast at 80m, is seen to be incomplete with missing data points in the duration of the POI (Fig. 4.18). With this constraint, along with the criterion set for choosing the cases, it is observed that the selected time slots appear to have either no turbulence information or erroneous data, which may be due to certain experimental deviations. Owing to the uncertainty of this parameter, we manually fit a value of ϵ at 80m for each case which is within the range of expected values observed which lies between $10^{-2} m^2/s^3$ and $10^{-3} m^2/s^3$ (Fig. 4.18). This is used to calculate the TIN (Eq. 2.10) obtained from each wind turbine. For the time slot considered before (51.5

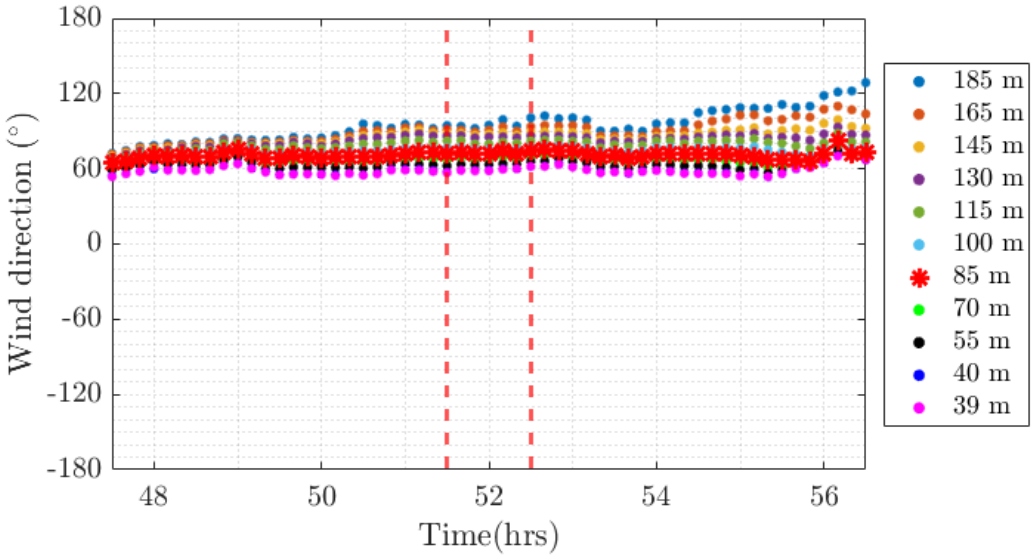

Figure 4.29: The wind direction recorded by the LIDAR at the height of 85m.

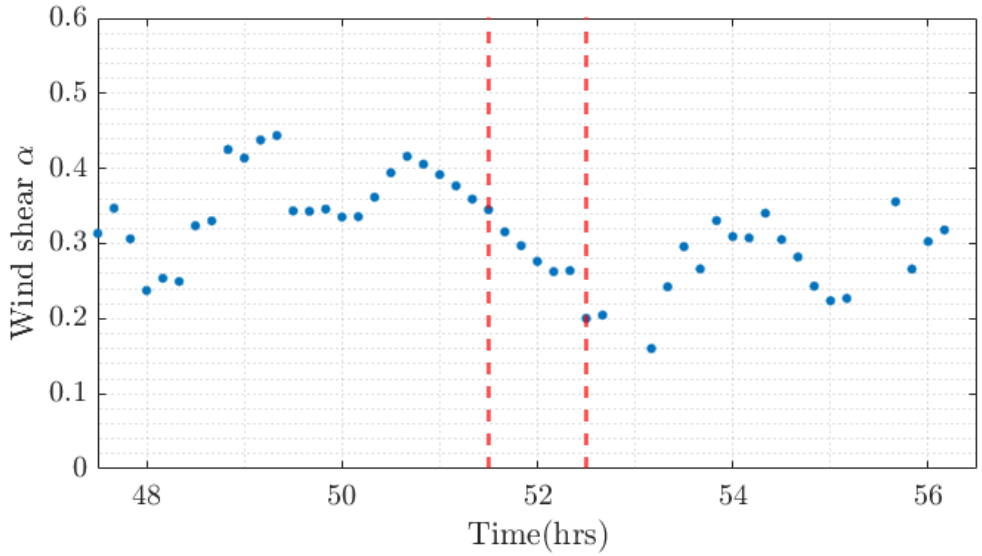

Figure 4.30: The wind shear calculated by the LIDAR data with the reference height at 85m for the duration under consideration.

to 52.5 hrs), Fig. 4.33 shows the predicted levels for the point L3-S3 with the two extremities of ϵ.

The TDR is also used to account for the scattering due to atmospheric turbulence. Muñoz-Esparza *et al.* [60] show that the turbulence dissipation rate near the ground can be close to 10 times that of the ϵ at 80m. We consider the same time slot as before (51.5 to 52.5 hrs) and observe the influence of the TDR on scattering for the points L3-S3 and L1-N3. For a fixed TDR, we consider a few levels of the

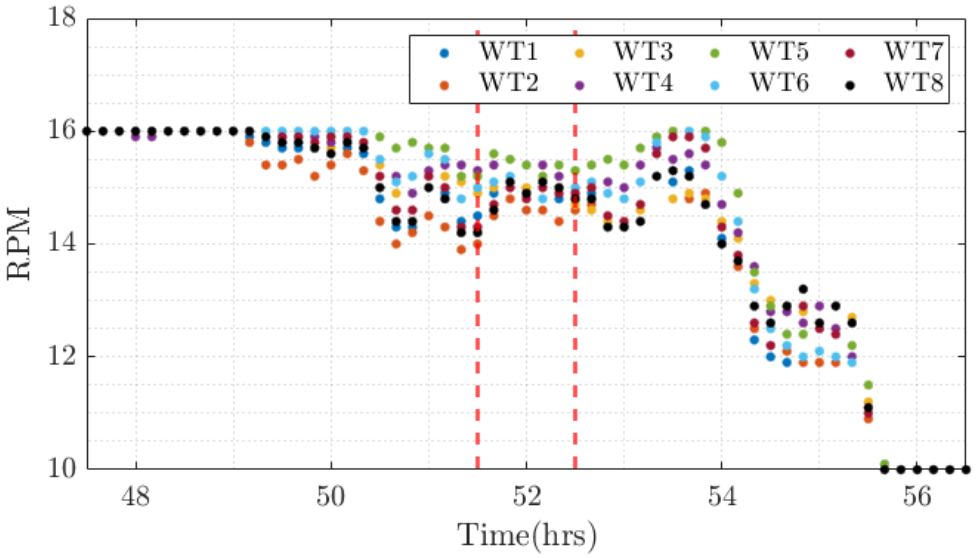

Figure 4.31: The RPM of each wind turbine for the duration under consideration.

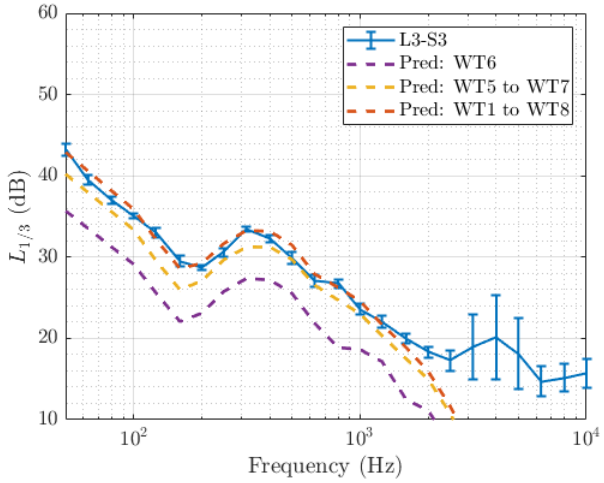

Figure 4.32: The predicted levels at receiver point L3-S3 considering the contribution from the nearest wind turbines.

scattering ϵ_{scat} that influence the scattering due to turbulence. Fig. 4.34 shows the predicted levels with different amounts of ϵ_{scat} for the upwind and downwind condition. It can be seen from Fig. 4.34 that for the downwind condition, the scattering due to turbulence is significant only close to the ground interference dips. This is in accordance with the results given in Section 2.3.4. For the upwind conditions, the influence due to the turbulence scattering is significant, with the highest assumed level of the scattering closest to the expected result.

For the comparison of the wind turbine model inclusive of the source and the propagation, we compare the model to the field measurements at certain interesting

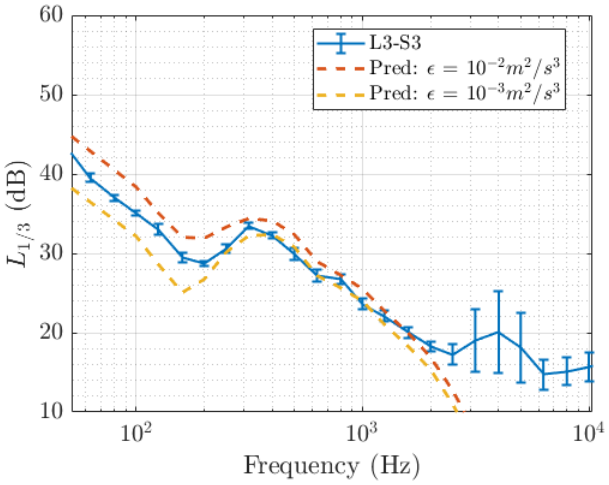

Figure 4.33: The predicted levels at the receiver point L3-S3 for the two extremities of the TDR values ϵ.

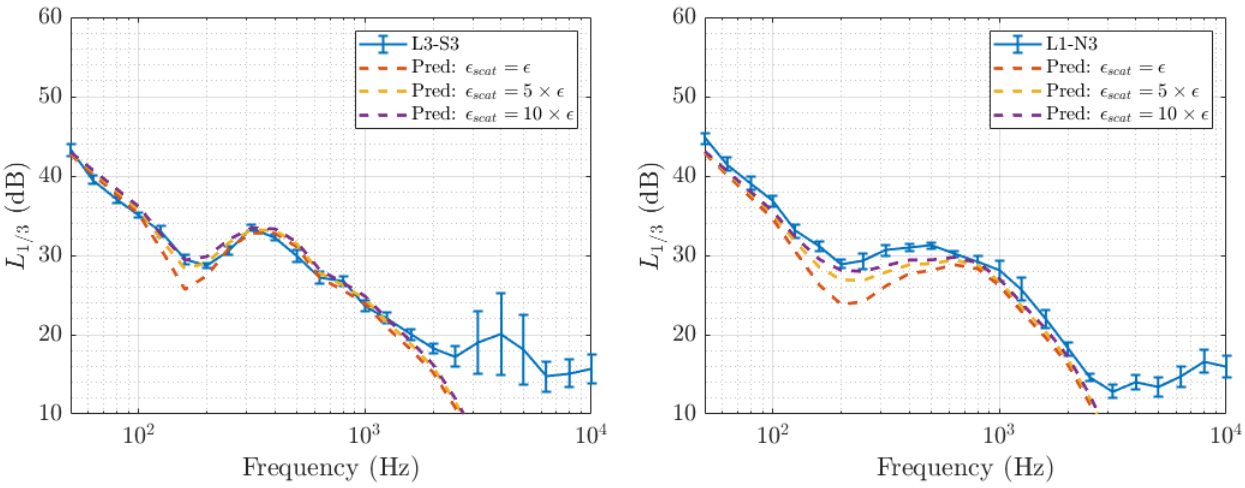

Figure 4.34: Comparison of the influence of ϵ_{scat} on the level of the spectra for downwind (left) and upwind (right).

time durations. The time durations that are manually selected are based on certain criteria: (i) the meteorological parameters such as wind speed, wind direction and wind shear are constant over the time duration and (ii) the acoustic measurement have a low standard deviation ($\leq$ 10dB) for most of the frequencies in interest. A few receiver positions are selected for the upwind and downwind conditions. The selected cases are given in Table 4.4 and are plotted in Figs. 4.35 to 4.37. The fitted values of the turbulence dissipation rate as ϵ^* are given in Table 4.4 for each case. The turbulence dissipation rate used for the scattering ϵ_{scat} is taken as 10 times of ϵ^*. The resultant simulations plotted as dashed lines are compared to the field measurements in Figures 4.35 to 4.37. In the figures, the solid lines show the field

measurements with the error bars depicting the standard deviation and the dashed lines showing the corresponding prediction of the model.

Case	Wind speed (m/s)	Wind shear α	Wind direction (deg)	Time (hrs)	Acoustic points	ϵ^* $(m^2/s^3) \times 10^{-3}$
4 a	8	0.34	-131	122 124	L1-2,4	10
4 b	7	0.3	73	51.5 52.5	L1-2,3,4	5
5 a	9	0.3	-134	124 126	L1-2,4	10
5 b	11	0.29	67	22.6 24	L1-2,3,4	5
6 a	7	0.28	73	51.5 52.5	L3-3,5	5
6 b	6	0.43	-131	220 221	L3-1,2,3,4,5	10

Table 4.4: Mean parameters used for the selected cases in the study of the propagation effects. ϵ^* shows the fitted TDR for each case.

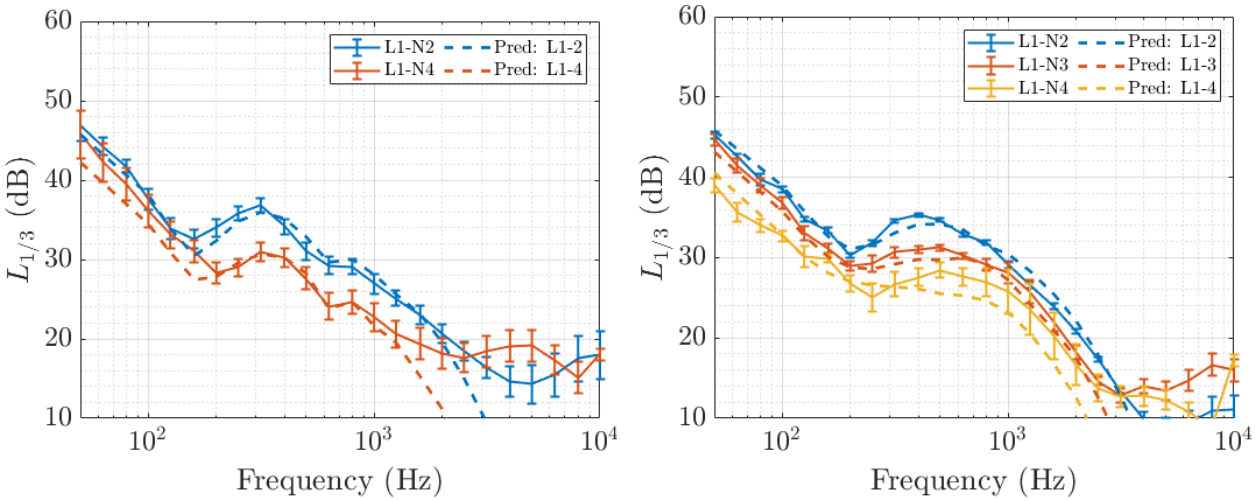

Figure 4.35: Third-octave band spectra of the measured (solid lines) and predicted (dashed lines) for cases 4a downwind (left) and 4b upwind (right) described in Table 2.

It can be seen from the selected cases that the predicted values are fairly close to the field measurements within certain frequency limits. Cases 4a, 5a and 6a show that the model captures the propagation effect for downwind conditions, while cases 4b, 5b and 6b show the same for upwind conditions. It can be seen that the interference pattern due to the ground effect is well captured for all the downwind cases, even at long range distances (L3-S5 in Case 6a). This validates a posteriori, the choice of the ground parameters for σ and e used in the Miki model. For the downwind condition, it can be seen that the model prediction is good over a broader range of frequencies for receivers that are closer to the wind turbine compared to those further away. This is possibly because the predicted values are lower than the

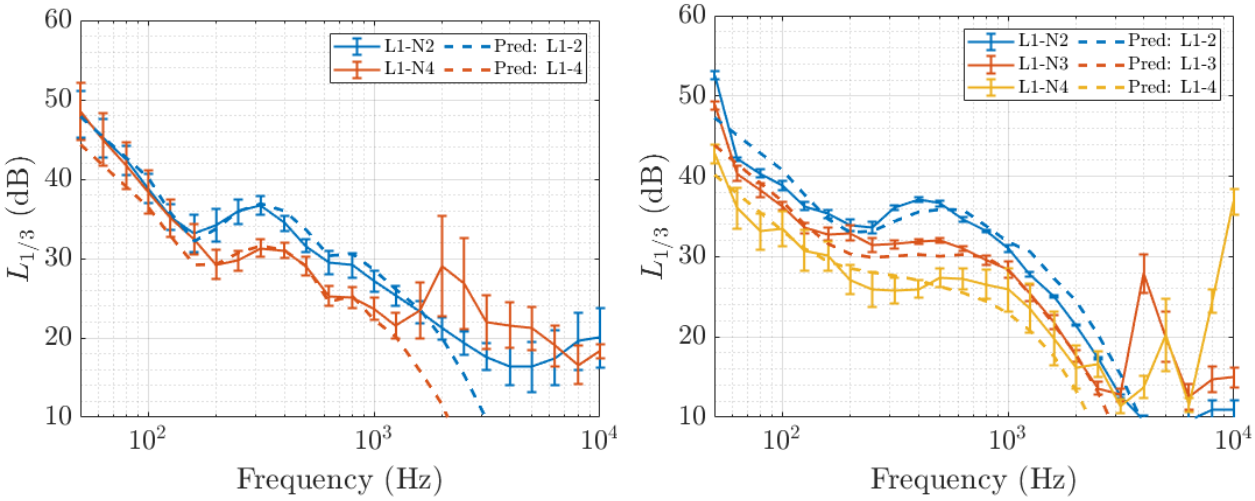

Figure 4.36: Third-octave band spectra of the measured (solid lines) and predicted (dashed lines) for cases 5a downwind (left) and 5b upwind (right) described in Table 2.

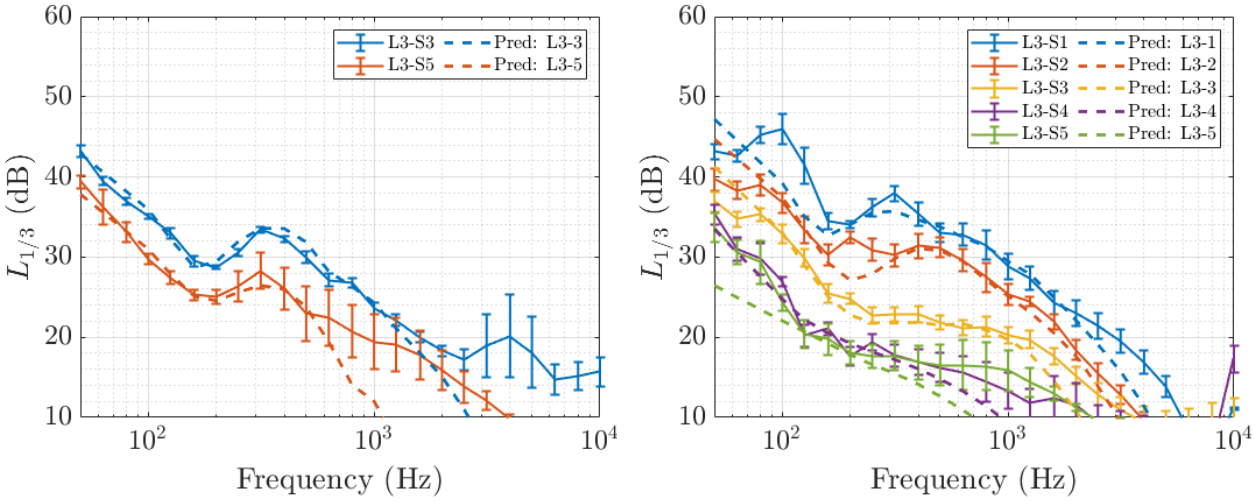

Figure 4.37: Third-octave band spectra of the measured (solid lines) and predicted (dashed lines) for cases 6a downwind (left) and 6b upwind (right) described in Table 2.

background noise that dominates the higher frequencies (L1-2 in Case 4a, 5a and L3-S5 in Case 6a).

For the upwind conditions, the predicted values are better for the receivers closer to the wind turbines compared to the ones further away (Cases 4b, 5b, 6b). However, the level of the spectra and also the general structure of each spectrum is well captured by the model. The evolution of the shadow zone with respect to distance is seen to be captured by the model, which is most evident in Case 6b.

4.7 Conclusion

The data collected by acoustic teams from CEREMA and l'Université Gustave Eiffel belonging to the UMRAE in the framework of the PIBE project was analyzed and compared to predictions from the studied wind turbine noise model. The PIBE campaign was carried out on a wind farm composed of 8 wind turbines of 3MW nominal electrical power each with a rotor diameter 90m and a hub height of 80m. The campaign was carried out for a duration of 410 days but only the first period of intensive observation (POI) that corresponds to 10 days from 23-06-2020 to 02-07-2020 is used in this thesis. A mast of 80m fitted with multiple sensors along with a LIDAR recorded the meteorological data while multiple sonometers at various distances recorded the acoustic data simultaneously.

The meteorological data was used as inputs for the wind turbine noise model and the comparison was done for the noise levels averaged over 10 minute intervals. The comparison of the source model to the recorded data at the IEC point shows that the prediction of the individual mechanisms of TIN and TEN are close to the field measurements. The peaks observed around 100 Hz and 4 kHz in the field measurements at the IEC point are not well predicted which may be a limitation of the source model. Accounting for the 2 nearest wind turbines in the model gives results that are closer to the field measurements. It is also shown that the inclusion of the directivity correction is important and the selected correction of $\mathcal{A}$=20% gives satisfactory results that are comparable to the measurements in the crosswind cases.

From the comparison of the model inclusive of the source as well as the propagation effects, it can be said that the model predictions are fairly close to the measured values considering the uncertainties on the ground impedance parameters and the turbulence dissipation rate. The model is able to capture the main effects of refraction due to the wind profile and ground reflection. For downwind conditions, the model is able to predict the noise levels for distances close to 1.5 km. In the case of the upwind conditions, the model is more reliable for distances closer to the wind turbine compared to further away. Overall, the developed model is validated against field measurements and appears to be reasonably good in predicting the third octave band spectra for the noise from the wind farm for various atmospheric conditions.

It has to be mentioned that the physical validation of the propagation modelling is done with certain assumptions which need to be verified. The prediction done is based on assigning the value of the turbulence dissipation rate ϵ for each

test case. One way of excluding the uncertainty of this parameter is to use multiple anemometers at different locations to understand the turbulence across the studied wind farm. A good estimate of ϵ would give more insight on the validity of the model. The assumption of the high turbulence scattering near the ground that influence the upwind conditions also needs to be confirmed with an anemometer placed closer to the ground. Better confidence in the ground parameters influencing the interference patterns would show the limitation of the model for this certain parameter. The comparison of the model is done while neglecting the effect of the temperature profile. However, in the parabolic equation that is used in the model, the temperature profile can be added easily to account for the corresponding refraction. The influence of the temperature profile on the propagation effects needs to be accounted for to have a better understanding on the refraction effects that are predicted by the model.

5

Conclusions and perspectives

Contents

5.1 Main conclusion of the thesis

The presented model that is developed for the synthesis of the wind turbine noise is physics-based as per our initial aim. The synthesis model advances from the frequency-domain model of Tian and Cotté [89] for wind turbine noise. Noise from the leading and trailing edge of the blades are predicted using Amiet's theory. The prediction is done for a blade that is segmented along its length. For the calculation of the trailing edge noise, the wall pressure spectra recently proposed by Lee [49] as an improvement of Rozenberg's model [82] is used for the suction side while for the pressure side, we use the model of Goody [34]. The turbulent inflow noise generated by the leading edge of the blade uses the Kolmogorov spectrum rather than the von Kármán spectrum. The segmentation done for Amiet's theory followed the large aspect ratio criteria. The limitations due to the segmentation of the blade are investigated using the Inverse Strip theory and it is concluded that this large aspect ratio criteria is no longer necessary while modelling the wind turbine blades. The directivity of the blade segments are corrected empirically to obtain predicted levels that are comparable to the measurements close to the rotor plane. To account for the propagation effect of refraction and ground reflection, the model uses the parabolic equation in a moving medium following the formulation given by Ostashev *et al.* [70]. This new formulation accounts for the wind speed profile separately without the assumption of the effective sound speed approximation. The advantage of this formulation is that the wind speed profile and temperature profile can be accounted for separately. We also include the Harmonoise model to account for the scattering

due to turbulence [83].

A synthesis tool is developed to obtain a time signal from the predicted wind turbine noise spectrum. The synthesis is done by availing of the inverse Discrete Fourier Transform to convert the frequency domain response of each segment at every angular transition, known as a grain. A window function is designed to achieve a smoother transition between grains. The window function takes into account the difference in the time duration due to the motion of the blade relative to the observer. The influence of certain parameters of the window function are investigated and their optimal value is determined. For a perceptual compliance, brown noise of the appropriate level is added to the signal of each grain. Multiple test cases are presented for the synthesis of the wind turbine noise under various conditions.

Finally, we compare the model to field measurements and investigate the validity of the model. We benefit from the data collected by the Unité Mixte de Recherche en Acoustique Environnementale (UMRAE) composed of the acoustic teams from CEREMA and l'Université Gustave Eiffel [22, 23, 1]. We focus on a specific period of ten days during this campaign when intensive observations on the wind farm were carried out. The data obtained during this intensive period included information on the functionality of the wind turbines on the wind farm, the meteorological conditions as well as the corresponding acoustic information. The data was processed to have relevant information to be used as input parameters for the developed wind turbine noise model. The comparison of the model is done separately for the source and propagation. For the comparison of the source part of the model, the predicted values of the model are compared to the third octave band noise levels at the IEC point at 125 m from the base of the wind turbine on a rigid platform. The model is able to predict the correct levels of the noise within the uncertainty margin. The model inclusive of the propagation effects is compared against field measurements at multiple locations for receiver distances varying from 330 m to 1.9 km from the closest wind turbine. The model predictions include the contributions of all eight wind turbines that compose the wind farm. The comparison is also done for downwind conditions as well as upwind. The model works well for the downwind condition and arguably well for the upwind condition.

5.2 Perspectives

Real time synthesis of wind turbine noise

The presented model currently does not function in real time. One of the main reasons for this is because the computational time required for the Parabolic equation is large. A possible solution is that a set of calculations are done beforehand and then selected as desired.

Psychoacoustic evaluation of the model

For the major part of the model, the synthesis and the evaluation is done objectively. However, from a perceptual point of view the synthesized model may differ from what is observed in reality. For this a psychoacoustic evaluation of the model is necessary to understand the perceptual limitations of the model. A few types of test which could be conducted are similarity test, confusion matrix test or ABX tests. However, all of these tests would require a reference signal of a wind turbine noise. One main factor that distinguishes the recorded signals from the synthesized sounds is the influence of the background noise. An unconventional method that can be used is to record background noise and layer it with the synthesized signal to be used in the tests mentioned above.

Inclusion of stall noise in the synthesis model

The model accounts for the trailing edge noise and the leading edge noise of the blade segments. The two types of noise occur at all angles of attack and are thus observed at all times. For high angles of attack when boundary separation occurs, stall noise is observed. This in turn leads to a sudden momentarily increase in the noise levels leading to increased amplitude modulation [62]. An inclusion of this type of noise as a first step would lead to having a more complete model of the wind turbine noise.

Inclusion of extraneous noise sources

To have a more realistic sound signal, certain sources need to be added to the signal. A few of such sounds are mechanical noise from the gearbox, tonal noise from the blade tower interaction and background noise.

A more robust validation of the model for various conditions

The comparison of the model done here for the source and propagation is done with uncertainties observed in the experimental data. A more robust technique is required to evaluate the data needed for the comparison with the model for different meteorological conditions. In this thesis, the model is compared to the time averaged spectral levels over 10 minute intervals. The characteristic of amplitude modulation of the wind turbine noise is not capture over such a large time period. To compare the amplitude modulation of the wind turbine noise we would need to look at the data with the time periods much less than the rotational period of the wind turbine. Comparing audio recordings or L_{100ms} with the predicted data is a possibility to validate the AM prediction of the model.

Abridging the gap between citizens, local authorities and acousticians for wind turbine noise

The model presented in this work gives the synthesized signals for wind turbine noise. It is also shown that the model predicts the wind turbine noise at the right spectral level. Acousticians and law makers can benefit of surveys that include listening tests which can be conducted with the help of the model. Using this model many misconceptions and problems regarding noise levels and disturbances due to wind turbine noise can be addressed to the public domain by local authorities.

Published articles during the thesis

During the course of the thesis, few articles have been published on this work. They are detailed as follows:

- ## Peer review journals

Title: **Synthesis of wind turbine trailing edge noise in free field**
Authors: David Mascarenhas, Benjamin Cotté, Olivier Doaré
Article in: JASA-Express Letters, Published Online: 3 March 2022

Title: **Propagation effects in the synthesis of wind turbine noise**
Authors: David Mascarenhas, Benjamin Cotté, Olivier Doaré
Article in: Acta Acustica, Under minor revisions: 10 March 2023

Title: **Validity of the effective sound speed approximation in parabolic**

equation models for wind turbine noise propagation
Authors: Bill Kayser, David Mascarenhas, Benjamin Cotté, David Ecotière, Benoit Gauvreau
Article in: JASA, Accepted on 7 March 2023

- **Conference papers**

Title: **Physics-based auralization of wind turbine noise**
Authors: David Mascarenhas, Benjamin Cotté, Olivier Doaré
Conference: 9^{th} International Conference on Wind Turbine Noise, Remote from Europe - 18 to 21 May 2021

Title: **Wind turbine noise modeling including aeroacoustic sources and propagation effects : Comparison against field measurements**
Authors: David Mascarenhas, Benjamin Cotté, Olivier Doaré, David Ecotière, Gwenaël Guillaume, Benoit Gauvreau, Isabelle Schmich-Yamane, Fabrice Junker
Conference: InterNoise 2022, Glasgow - 21 to 24 August 2022

Title: **Auralization of Wind Turbine Noise Using Physics-Based Emission and Propagation Models**
Authors: David Mascarenhas, Benjamin Cotté, Olivier Doaré
Conference: 24^{th} International Congress on Acoustics, Korea - 24 to 28 October 2022

Appendices

A

Numerical solution for the wide angle parabolic equation in moving medium

In this Appendix, we explain how the parabolic equation presented in Sec.2.3.2 can be numerically solved. First, the solution of Eq. (2.25) is advanced along x using the Crank-Nicholson (CN) scheme:

$$\left[\Psi_1 - \frac{ik_0\Delta x}{2}\Psi_2\right]\bar{\phi}(x+\Delta x) = \left[\Psi_1 + \frac{ik_0\Delta x}{2}\Psi_2\right]\bar{\phi}(x), \tag{A.1}$$

where the terms Ψ_1 and Ψ_2 can be written:

$$\Psi_1 = 1 + \frac{\eta}{4} + \frac{1}{4k_0^2\zeta_x^2}\frac{\partial^2}{\partial z^2}, \tag{A.2}$$

$$\Psi_2 = \frac{\zeta_x^2\eta}{2} - \left(1+\frac{\eta}{4}\right)\tilde{\tau} + \frac{(2\zeta_x^2 - \tilde{\tau})}{4k_0^2\zeta_x^2}\frac{\partial^2}{\partial z^2}. \tag{A.3}$$

The domain is now discretized with mesh sizes Δx and Δz: $\phi_m^n = \bar{\phi}(m\Delta x, n\Delta z)$, with $m = 1..M$ and $n = 1..N$. The second derivative with respect to z is estimated using a second order finite difference scheme:

$$\left(\frac{\partial^2}{\partial z^2}\right)\phi_m^n = \frac{\phi_m^{n+1} - 2\phi_m^n + \phi_m^{n-1}}{k_0^2\Delta z^2}. \tag{A.4}$$

The numerical scheme associated with the CN for the WAPE method is thus:

$$M_1\phi_{m+1}^n = M_2\phi_m^n, \tag{A.5}$$

where the matrices M_1 and M_2 are given by:

$$M_1\phi_m^n = \left[1 + \frac{\eta_m^n}{4} - \frac{ik_0\Delta x}{2}\left(\frac{(\zeta_x^2)_m^n\eta_m^n}{2} - (1+\frac{\eta_m^n}{4})\tilde{\tau}_m^n\right)\right]\phi_m^n + \left[\frac{2 - ik_0\Delta x(2(\zeta_x^2)_m^n - \tilde{\tau}_m^n)}{8k_0^2(\zeta_x^2)_m^n}\right]\frac{\phi_m^{n+1} - 2\phi_m^n + \phi_m^{n-1}}{\Delta z^2}, \tag{A.6}$$

$$M_2\phi_m^n = \left[1 + \frac{\eta_m^n}{4} - \frac{ik_0\Delta x}{2}\left(\frac{(\zeta_x^2)_m^n\eta_m^n}{2} - (1+\frac{\eta_m^n}{4})\tilde{\tau}_m^n\right) - \frac{2 - ik_0\Delta x(2(\zeta_x^2)_m^n - \tilde{\tau}_m^n)}{4k_0^2(\zeta_x^2)_m^n\Delta z^2}\right]\phi_m^n + \left[\frac{2 - ik_0\Delta x(2(\zeta_x^2)_m^n - \tilde{\tau}_m^n)}{8k_0^2(\zeta_x^2)_m^n\Delta z^2}\right]\left(\phi_m^{n+1} + \phi_m^{n-1}\right). \tag{A.7}$$

The matrix M_1 in Eq. (A.6) is tridiagonal with diagonal elements

$$b_n = \left[1 + \frac{\eta}{4} - \frac{ik_0\Delta x}{2}\left(\frac{\zeta_x^2\eta}{2} - (1+\frac{\eta}{4})\tilde{\tau}\right) - \frac{2 - ik_0\Delta x(2\zeta_x^2 - \tilde{\tau})}{4k_0^2\zeta_x^2\Delta z^2}\right], \tag{A.8}$$

and off-diagonal elements

$$a_n = c_n = \left[\frac{2 - ik_0\Delta x(2\zeta_x^2 - \tilde{\tau})}{8k_0^2\zeta_x^2\Delta z^2}\right]. \tag{A.9}$$

Similarly, the matrix M_2 in Eq. (A.7) is tridiagonal with diagonal elements

$$e_n = \left[1 + \frac{\eta}{4} + \frac{ik_0\Delta x}{2}\left(\frac{\zeta_x^2\eta}{2} - (1+\frac{\eta}{4})\tilde{\tau}\right) - \frac{2 + ik_0\Delta x(2\zeta_x^2 - \tilde{\tau})}{4k_0^2\zeta_x^2\Delta z^2}\right], \tag{A.10}$$

and off-diagonal elements

$$d_n = f_n = \left[\frac{2 + ik_0\Delta x(2\zeta_x^2 - \tilde{\tau})}{8k_0^2\zeta_x^2\Delta z^2}\right]. \tag{A.11}$$

The boundary condition at $z = 0$ (n = 1) written with respect to the normalized admittance $\beta = 1/Z$ can be obtained by using the centered second order scheme at the fictitious point ϕ_m^0 with $z = -\Delta z$:

$$\frac{\phi_m^2 - \phi_m^0}{2\Delta z} + ik_0\beta\phi_m^1 = 0. \tag{A.12}$$

The first lines of the matrices M_1 and M_2 are changed accordingly, with modified coefficients:

$$c_{1g} = 2c_1, \qquad b_{1_g} = b_1 + 2ik_0\Delta z\beta c_1,$$
$$f_{1g} = 2f_1, \qquad e_{1_g} = e_1 + 2ik_0\Delta z\beta f_1.$$

B

Time difference between grains studied using ray-tracing method

We need to see the influence of the temperature and wind speed profiles on the time duration of the synthesized grain (Eq.3.4). The relative time difference due to propagation between two grains in free field and homogeneous medium without wind is given by Δt_p. The maximum time difference Δt_p is observed at the crosswind direction and minimum for the upwind and downwind directions. To isolate the effect of the propagation on the time of each grain, we look in the direction of the wind where the refraction effect is maximum.

Based on the ray-tracing model if the distance of the ray path from point A to point B is l, the time taken for a sound wavefront to travel the path is given by [72]:

$$t'_n = \int_A^B \frac{dl}{\mathbf{v}\cdot\mathbf{x}' + \sqrt{c_z^2 - v^2 + (\mathbf{v}\cdot\mathbf{x}')^2}}, \tag{B.1}$$

where c_z is the sound speed, v is the velocity of the medium, $\mathbf{x}' = d\mathbf{x}/dl$ denotes the ray direction in the $\mathbf{x}$ coordinates system and $\mathbf{v}\cdot\mathbf{x}'$ is the velocity projected in the ray direction . We compute the time taken for each ray to travel from the tip of the wind turbine blade (point A) at every discrete angular position to a receiver in the far field, x_R=1000m (point B). The propagation time difference between two successive grains is thus given by $\Delta t'_p = t'_n - t'_{n+1}$, where t'_n is the propagation time for the refracted ray calculated from Eq. B.1. To see how much the time duration of the each grain changes with and without the influence of the propagation effect, the absolute maximum difference $|\Delta t'_p - \Delta t_p|$ is calculated.

A power law profile is used for the wind speed at different heights given by: $U(z) = U_{ref}\,(z/z_{ref})^{\alpha}$ with $z_{ref} = 80m$. To account for the effect of a temperature gradient a logarithmic sound speed profile is used given as: $c_z = c_0 + b_t \log(1 + z/z_0)$,

$z_0 = 0.1$ [84]. The different profiles studied are given in Table B.1. We compare the direct and refracted time differences for a receiver downwind at x_R=1000 m, z_R=2 m for a sound emitted by the tip segment of blade radius 45 m and hub height 80 m rotating through 36 angular positions. The maximum absolute time difference between each grain $\max(|\Delta t'_p - \Delta t_p|)$ and the difference between the direct and refracted ray $|t'_n - R/c_0|$ is given in Table B.1.

Wind and sound speed profile parameters			$\max(\lvert\Delta t'_p - \Delta t_p\rvert)$	$\max(\lvert t'_n - R/c_0\rvert)$
U_{ref}(m/s)	α	b_t	(ms)	(ms)
0	-	0	0.0	0.0
8	0.2	0	0.9	10.6
8	0.5	0	1.9	21.1
0	-	1	0.8	9.4
8	0.5	1	2.3	26.1
10	0.5	1	2.8	30.1

Table B.1: The wind speed and sound speed profiles parameters studied along with the maximum difference between the direct and refracted ray.

It can be seen that with the maximum refraction, the difference between the grain duration is at most 3 ms. The propagation time difference between the direct and refracted ray for the studied cases is less than 50 ms. For this study using the ray tracing model, only the downwind direction is considered. This is because in this direction there is a downward refraction of the wave, while for the upwind direction there is an upward refraction of the wave and the calculated sound ray does not reach the receiver if the receiver is well in the shadow zone. This is not entirely true if a atmospheric scattering is considered and this restriction of the model is due to the high frequency approximation of the sound wave to a geometrical ray. The model is thus used to study only the time difference between each grain downwind. In conclusion, it can be said from this study that the influence of the refraction effect on the duration of each grain is negligible.

C

Document provided by CEREMA for the ground parameter

PIBE - Mesure d'impédance DLCF juin 2020 – Bonneval (28)

Matériel de mesure DLCF et version MIAME

DELL Latitude E5510 sous XP Pro – Logiciel Proto_Plume_V15_Auto sous Scilab 5.4.1

Tableau récapitulatif des résultats de mesure du DLCF

Dates	Lieu	Essai	σ (résistance) $kNsm^{-4}$	e (épaisseur) cm
23/06/2020	Terre	1g	60	5
24/06/2020	Chemin roues	1a	2100	1
		1b	4600	0.7
		1c	4500	0.7
24/06/2020	Milieu chemin	2a	810	1
		2b	800	1
		2c	790	1
24/06/2020	Friche	3a	410	1,5
		3b	330	2
		3c	10	1,5
24/06/2020	Terre	4a	60	5
		4b	60	5
		4c	60	5
01/07/2020	Terre	1a	80	4.5
		1c	100	4
		1d	70	5
		2a	140	3.5
		2b	150	3.5
		2d	140	3.5
01/07/2020	Friche	3a	210	2.5
		3b	210	2.5
		3c	210	2.5
		4a	150	3
		4c	150	3
		4d	150	3
01/07/2020	Jachère	5a	120	3.5
		5b	110	3.5
		5c	120	3.5
		6a	10	2.5
		6b	10	2.5

Les résultats en rouge ont été jugés non conformes et ne sont pas pris en compte dans la moyenne des essais.

Graphes des mesures d'impédance

24/06/2020 – Roues chemin – 1a - 10h17, 1b - 10h31, 1c - 10h38, σ = 3733 kNsm^{-4} – e = 0.8 cm

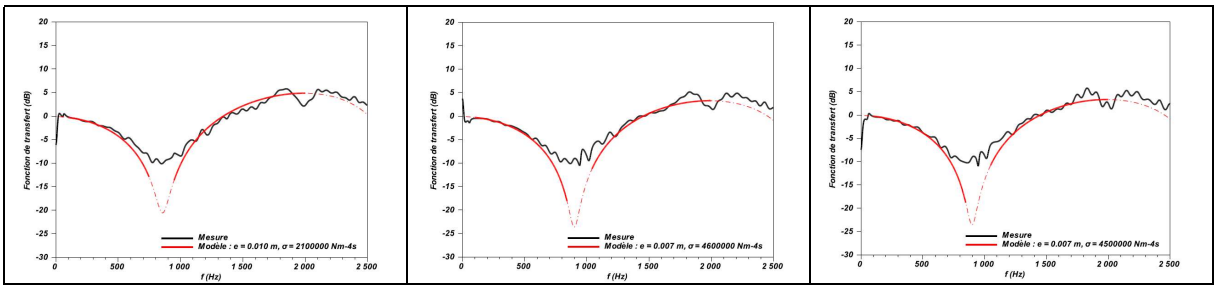

24/06/2020 – Milieu chemin – 2a - 10h43, 2b - 10h48, 2c - 10h58, σ = 800 kNsm^{-4} – e = 1 cm

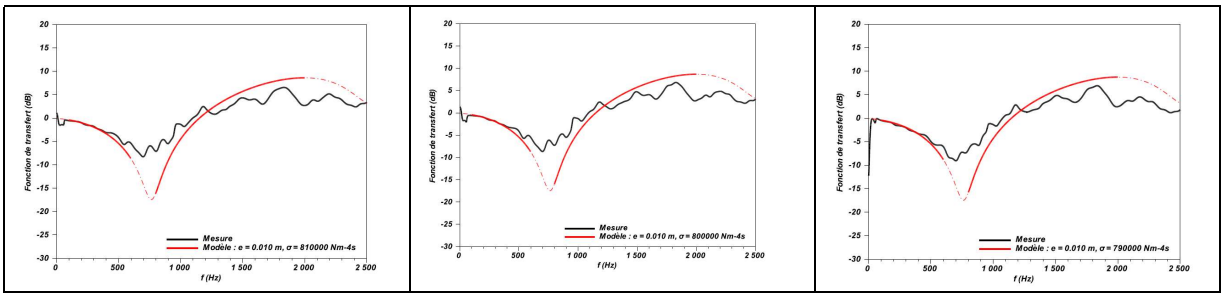

24/06/2020 – Friche – 3a - 11h19, 3b - 11h34, 3c - 11h40, σ = 370 kNsm^{-4} – e = 1.8 cm

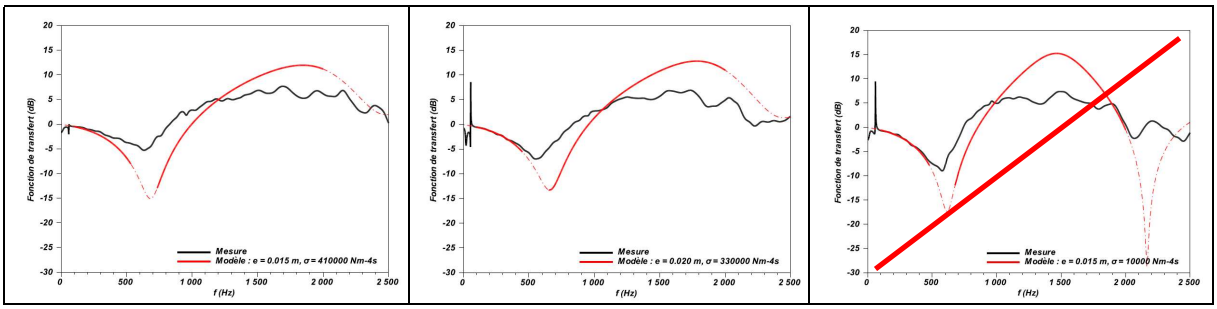

24/06/2020 – Terre – 4a - 11h50, 4b - 11h53, 4c - 11h56, σ = 60 kNsm^{-4} – e = 5 cm

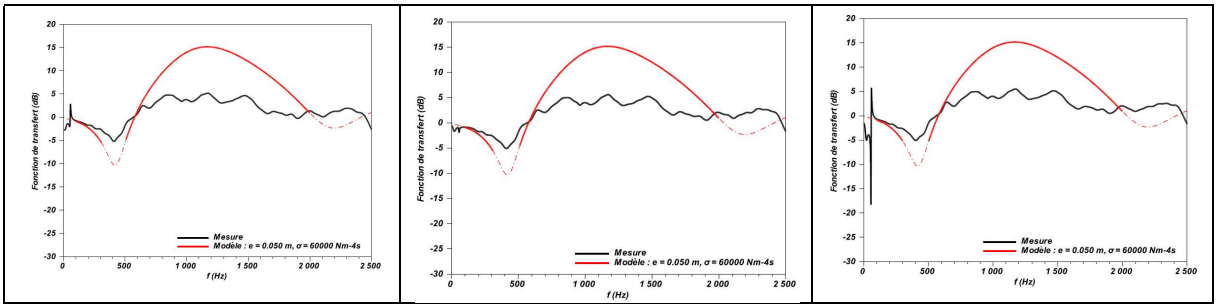

01/07/2020 – Terre n°1 – 1a – 13h34, 1c – 13h39, 1d – 13h42, σ = 83 kNsm^{-4} – e = 4.5 cm

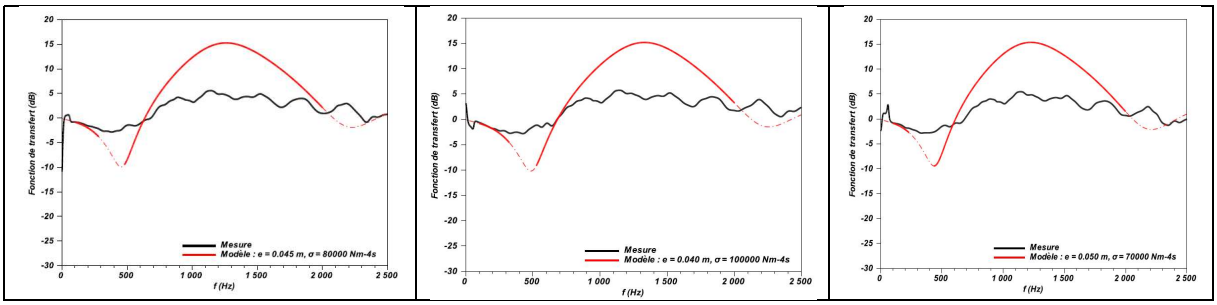

01/07/2020 - Terre n°2 – 2a – 13h48, 2b – 13h53, 2d – 14h02, σ = 143 kNsm^{-4} – e = 3.5 cm

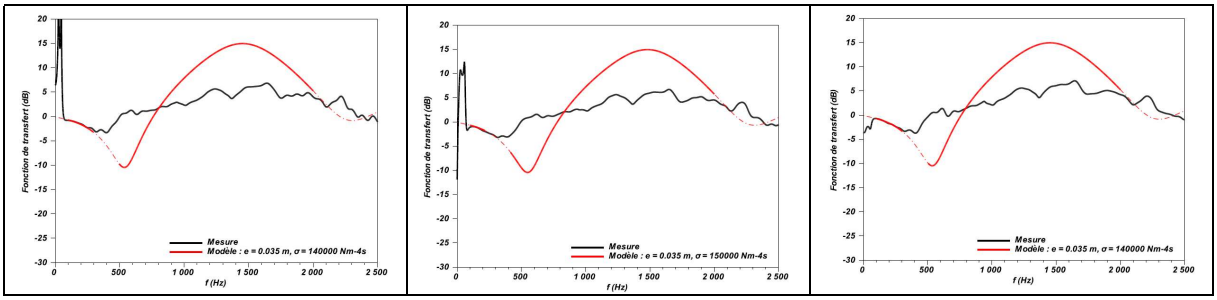

01/07/2020 - Friche n°1 – 3a – 14h22, 3b – 14h26, 3c – 14h30, σ = 210 kNsm^{-4} – e = 2.5 cm

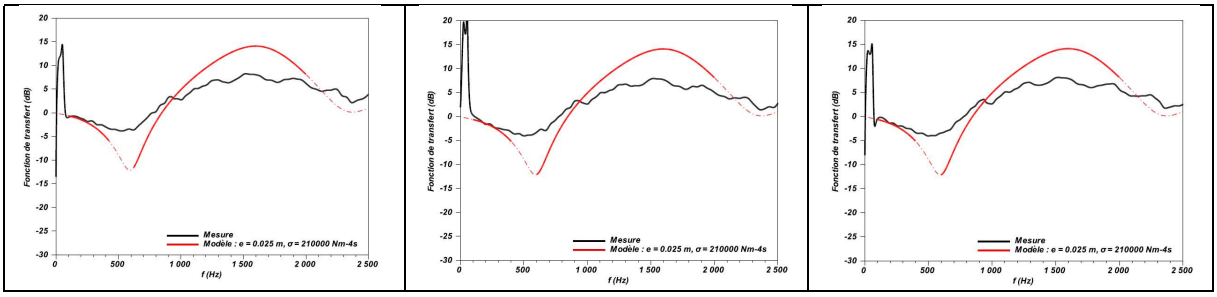

01/07/2020 - Friche n°2 – 4a – 14h37, 4c – 14h46, 4d – 14h53, σ = 150 kNsm^{-4} – e = 3 cm

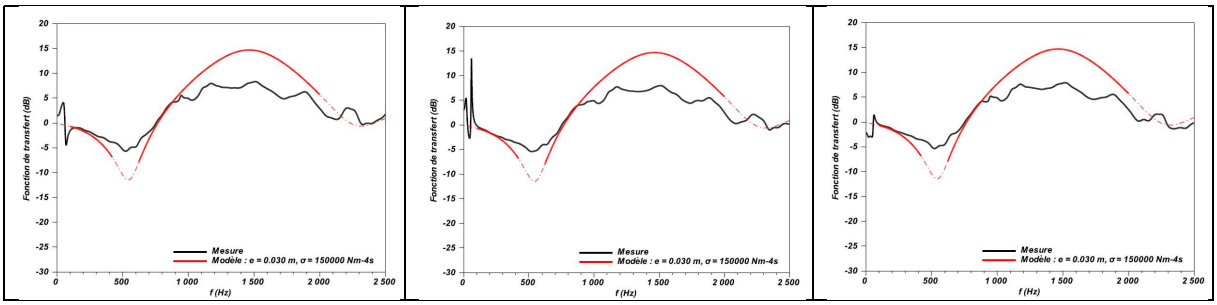

01/07/2020 - Jachère n°1 – 5a – 15h39, 5b – 15h42, 5c – 15h44, σ = 117 kNsm^{-4} – e = 3.5 cm

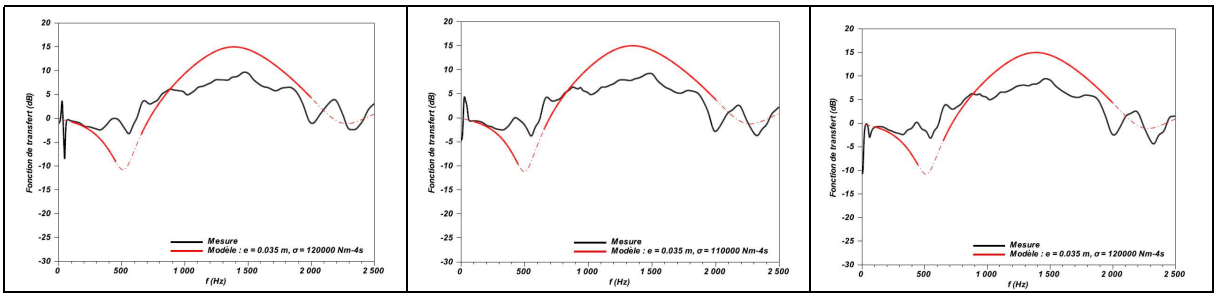

01/07/2020 - Jachère n°2 – 6a – 15h50, 6b – 15h53, arrêt (pluie), σ = 10 kNsm^{-4} – e = 2.5 cm

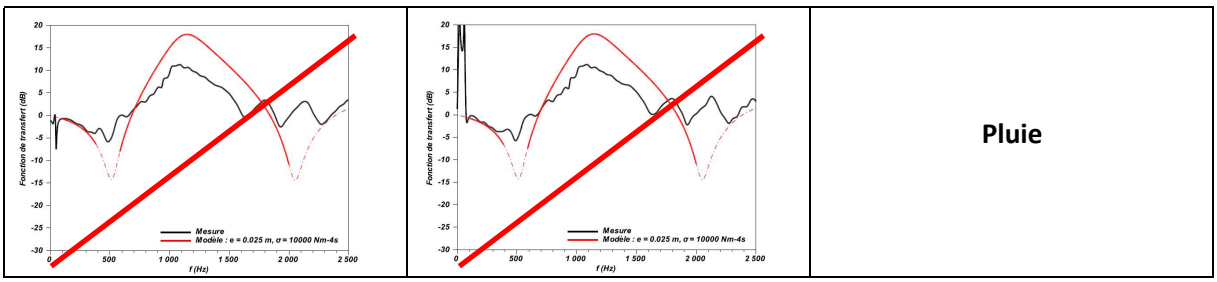

Remarques :

Les mesures d'impédance semblent cohérentes avec une gamme comprise entre σ = 3733 kNsm^{-4} pour une terre compactée par le passage des véhicules sur le chemin et σ = 60 kNsm^{-4} pour une terre meuble le 24/06/2020.

Une évolution de l'impédance sur 7 jours passant de 60 à 113 kNsm^{-4} pour la terre meuble sans culture pouvant provenir du piétinement des opérateurs.

Une évolution en sens contraire pour la friche sur 7 jours passant de 370 à 180 kNsm^{-4} sans doute due à l'assèchement de la végétation.

On note une différence suivant les positions de mesure entre la position initiale et celle réalisée à environ 90° de la première du fait du sol non plan (sillons, présence de cailloux).

Certaines modélisations sont non conformes : 3c du 24/06/2020 et 6a et 6b du 01/07/2020 avec un deuxième pic d'absorption vers 2000 Hz.

Photos

		
Milieu du chemin **σ = 800 kNsm^{-4}**	Friche **σ = 370 kNsm^{-4}**	Jachère **σ = 117 kNsm^{-4}**

	
Terre le 24/06/2020 **σ = 60 kNsm^{-4}**	Terre le 01/07/2020 **σ = 113 kNsm^{-4} (moyenne 6 valeurs)**

	
Friche le 24/06/2020 **σ = 370 kNsm^{-4}**	Friche le 01/07/2020 **σ = 180 kNsm^{-4} (moyenne 6 valeurs)**

Bibliography

[1] `https://www.anr-pibe.com/en`. Accessed on: 25th April 2022.

[2] Roy K Amiet. "Acoustic radiation from an airfoil in a turbulent stream". In: *Journal of Sound and vibration* 41.4 (1975), pp. 407–420.

[3] Roy K Amiet. "Noise due to turbulent flow past a trailing edge". In: *Journal of sound and vibration* 47.3 (1976), pp. 387–393.

[4] M Arntzen and DG Simons. "Modeling and synthesis of aircraft flyover noise". In: *Applied Acoustics* 84 (2014), pp. 99–106.

[5] *Arrêté du 26 août 2011 relatif aux installations de production d'électricité utilisant l'énergie mécanique du vent au sein d'une installation soumise à autorisation au titre de la rubrique 2980 de la législation des installations classées pour la protection de l'environnement.* JORF n°0198 du 27 août 2011. 2011.

[6] Tom Bäckström. "Overlap-add Windows with Maximum Energy Concentration for Speech and Audio Processing". In: *ICASSP 2019-2019 IEEE International Conference on Acoustics, Speech and Signal Processing (ICASSP)*. IEEE. 2019, pp. 491–495.

[7] Emre Barlas et al. "Consistent modelling of wind turbine noise propagation from source to receiver". In: *The Journal of the Acoustical Society of America* 142.5 (2017), pp. 3297–3310.

[8] Emre Barlas et al. "Effects of wind turbine wake on atmospheric sound propagation". In: *Applied Acoustics* 122 (2017), pp. 51–61.

[9] Franck Bertagnolio, H Aa Madsen, and Andreas Fischer. "A combined aeroelastic-aeroacoustic model for wind turbine noise: verification and analysis of field measurements". In: *Wind Energy* 20.8 (2017), pp. 1331–1348.

[10] Franck Bertagnolio et al. "A semi-empirical airfoil stall noise model based on surface pressure measurements". In: *Journal of Sound and Vibration* 387 (2017), pp. 127–162.

[11] Ph Blanc-Benon, L Dallois, and D Juvé. “Long range sound propagation in a turbulent atmosphere within the parabolic approximation”. In: *Acta Acustica united with Acustica* 87.6 (2001), pp. 659–669.

[12] Karl Bolin, Mathieu Boué, and Ilkka Karasalo. “Long range sound propagation over a sea surface”. In: *The Journal of the Acoustical Society of America* 126.5 (2009), pp. 2191–2197.

[13] Karl Bolin, Mats E Nilsson, and Shafiquzzaman Khan. “The potential of natural sounds to mask wind turbine noise”. In: *Acta Acustica united with Acustica* 96.1 (2010), pp. 131–137.

[14] Andrea PC Bresciani, Julien Maillard, and Leandro D De Santana. “Perceptual evaluation of wind turbine noise”. In: *16ème Congrès Français d’Acoustique*. 2022.

[15] Thomas F Brooks and TH Hodgson. “Trailing edge noise prediction from measured surface pressures”. In: *Journal of sound and vibration* 78.1 (1981), pp. 69–117.

[16] Thomas F Brooks, D Stuart Pope, and Michael A Marcolini. *Airfoil self-noise and prediction*. Vol. 1218. National Aeronautics and Space Administration, Office of Management ..., 1989.

[17] Steven Buck, Stefan Oerlemans, and Scott Palo. “Experimental validation of a wind turbine turbulent inflow noise prediction code”. In: *AIAA Journal* 56.4 (2018), pp. 1495–1506.

[18] J Christophe, J Anthoine, and S Moreau. “Amiet’s theory in spanwise-varying flow conditions”. In: *AIAA journal* 47.3 (2009), pp. 788–790.

[19] Benjamin Cotté. “Coupling of an aeroacoustic model and a parabolic equation code for long range wind turbine noise propagation”. In: *Journal of Sound and Vibration* 422 (2018), pp. 343–357.

[20] Benjamin Cotté. “Extended source models for wind turbine noise propagation”. In: *The Journal of the Acoustical Society of America* 145.3 (2019), pp. 1363–1371.

[21] N Curle. “The influence of solid boundaries upon aerodynamic sound”. In: *Proceedings of the Royal Society of London. Series A. Mathematical and Physical Sciences* 231.1187 (1955), pp. 505–514.

[22] D Ecotière et al. “PIBE: A new French project for predicting the impact of wind turbine noise”. In: *Proceedings of the 8th International Conference on Wind Turbine Noise, Lisbon, Portugal*. 2019, pp. 12–14.

[23] D. Ecotière et al. “A large-scale, long-term experimental campaign for the investigation of wind turbine noise fluctuations and amplitude modulation

phenomena". In: *Proceedings of the 51st Internoise Congress., Glasgow, UK*. 2022.

[24] Anne-Sophie Evrard et al. "Research on the impacts of wind turbine noise on humans: Sound, perception, health (RIBEolH)". In: *Proceedings of the 13th ICBEN International Congress on Noise as a Public Health Problem, Stockholm, Sweden*. 2021, pp. 14–17.

[25] Marco Fink, Martin Holters, and Udo Zölzer. "SIGNAL-MATCHED POWER-COMPLEMENTARY CROSS-FADING AND DRY-WET MIXING". In: *Proceedings of the 19th International Conference on Digital Audio Effects (DAFx-16)* (2016).

[26] Andreas Fischer, Franck Bertagnolio, and Helge Aa Madsen. "Improvement of TNO type trailing edge noise models". In: *European Journal of Mechanics-B/Fluids* 61 (2017), pp. 255–262.

[27] Thomas Foken. "50 years of the Monin–Obukhov similarity theory". In: *Boundary-Layer Meteorology* 119.3 (2006), pp. 431–447.

[28] Benoit Gauvreau et al. "Traffic noise prediction with the parabolic equation method: Validation of a split-step Padé approach in complex environments". In: *The Journal of the Acoustical Society of America* 112.6 (2002), pp. 2680–2687.

[29] Fernando Gea-Aguilera. "Aerodynamic and aeroacoustic modelling of engine fan broadband noise". PhD thesis. University of Southampton, 2017.

[30] Matthieu BR Gelot and Jae Wook Kim. "Broadband noise prediction for aerofoils with a serrated trailing edge based on Amiet's theory". In: *Journal of Sound and Vibration* 512 (2021), p. 116352.

[31] Fotis Georgiou, Maarten Hornikx, and Armin Kohlrausch. "Auralization of a car pass-by inside an urban canyon using measured impulse responses". In: *Applied Acoustics* 183 (2021), p. 108291.

[32] Fotis Georgiou, Maarten Hornikx, and Armin Kohlrausch. "Auralization of a car pass-by using impulse responses computed with a wave-based method". In: *Acta Acustica united with Acustica* 105.2 (2019), pp. 381–391.

[33] SAL Glegg, SM Baxter, and AG Glendinning. "The prediction of broadband noise from wind turbines". In: *Journal of sound and vibration* 118.2 (1987), pp. 217–239.

[34] Michael Goody. "Empirical spectral model of surface pressure fluctuations". In: *AIAA journal* 42.9 (2004), pp. 1788–1794.

[35] Gwenaël Guillaume et al. “Estimation of impedance model input parameters from in situ measurements: Principles and applications”. In: *Applied Acoustics* 95 (2015), pp. 27–36.

[36] Francisco Haces-Fernandez, Mariee Cruz-Mendoza, and Hua Li. “Onshore Wind Farm Development: Technologies and Layouts”. In: *Energies* 15.7 (2022), p. 2381.

[37] Dietrich Heimann, Antonia Englberger, and Arthur Schady. “Sound propagation through the wake flow of a hilltop wind turbine—A numerical study”. In: *Wind Energy* 21.8 (2018), pp. 650–662.

[38] Dietrich Heimann, Yvonne Käsler, and Günter Gross. “The wake of a wind turbine and its influence on sound propagation”. In: *Meteorologische Zeitschrift* 20 (2011), pp. 449–460.

[39] Michaela Herr et al. “Broadband trailing-edge noise predictions—overview of BANC-III results”. In: *21st AIAA/CEAS Aeroacoustics Conference*. 2015, p. 2847.

[40] Michael S Howe and Michael S Howe. *Acoustics of fluid-structure interactions*. Cambridge university press, 1998.

[41] *IEA (2019), World Energy Outlook 2019*. IEA, Paris, 2019.

[42] IPCC. “Summary for Policymakers”. In: *Global Warming of 1.5°C: IPCC Special Report on Impacts of Global Warming of 1.5°C above Pre-industrial Levels in Context of Strengthening Response to Climate Change, Sustainable Development, and Efforts to Eradicate Poverty*. Cambridge University Press, 2022, pp. 1–24. DOI: 10.1017/9781009157940.001.

[43] Jan Jagla, Julien Maillard, and Nadine Martin. “Sample-based engine noise synthesis using an enhanced pitch-synchronous overlap-and-add method”. In: *The Journal of the Acoustical Society of America* 132.5 (2012), pp. 3098–3108.

[44] Lee Joyce and Zhao Feng. *GLOBAL WIND REPORT 2021*. Global wind energy council, 2021.

[45] M Kamruzzaman et al. “A semi-empirical surface pressure spectrum model for airfoil trailing-edge noise prediction”. In: *International Journal of Aeroacoustics* 14.5-6 (2015), pp. 833–882.

[46] M Kamruzzaman et al. “Validations and improvements of airfoil trailing-edge noise prediction models using detailed experimental data”. In: *Wind Energy* 15.1 (2012), pp. 45–61.

[47] Bill Kayser et al. “Validity of the effective sound speed approximation in parabolic equation models for wind turbine noise propagation (submitted)”. In: *JASA* (2022).

[48] Erik Koppen and Kevin Fowler. “International legislation for wind turbine noise”. In: *Proceedings of the Euronoise*. NAG, ABAV Maastricht, The Netherlands. 2015, pp. 321–326.

[49] Seongkyu Lee. “Empirical wall-pressure spectral modeling for zero and adverse pressure gradient flows”. In: *AIAA Journal* 56.5 (2018), pp. 1818–1829.

[50] Seongkyu Lee and Jessica G Shum. “Prediction of airfoil trailing-edge noise using empirical wall-pressure spectrum models”. In: *AIAA Journal* 57.3 (2019), pp. 888–897.

[51] Seunghoon Lee, Seungmin Lee, and Soogab Lee. “Numerical modeling of wind turbine aerodynamic noise in the time domain”. In: *The Journal of the Acoustical Society of America* 133.2 (2013), EL94–EL100.

[52] RJ Lowe and P Drummond. “Solar, wind and logistic substitution in global energy supply to 2050–Barriers and implications”. In: *Renewable and Sustainable Energy Reviews* 153 (2022), p. 111720.

[53] Julien Maillard. “Auralisation of environmental sources”. In: *Presentation at the VRACE technical workshop, Paris*. May 2022.

[54] Julien Maillard and Jan Jagla. “Auralization of non-stationary traffic noise using sample based synthesis-Comparison with pass-by recordings”. In: *INTER-NOISE and NOISE-CON Congress and Conference Proceedings*. Vol. 2012. 5. Institute of Noise Control Engineering. 2012, pp. 5978–5989.

[55] Julien Maillard et al. “Physically-Based Auralization of Railway Rolling Noise”. In: *Proceedings of the 23rd International Congress on Acoustics : integrating 4th EAA Euroregio 2019 : 9-13 September 2019 in Aachen, Germany*.

[56] S McBride and R Burdisso. “A comprehensive Hamiltonian ray tracing technique for wind turbine noise propagation under arbitrary weather conditions”. In: *Seventh International Meeting on Wind Turbine Noise*. 2017, pp. 1–12.

[57] David S Michaud et al. “Effects of wind turbine noise on self-reported and objective measures of sleep”. In: *Sleep* 39.1 (2016), pp. 97–109.

[58] David S Michaud et al. “Exposure to wind turbine noise: Perceptual responses and reported health effects”. In: *The Journal of the Acoustical Society of America* 139.3 (2016), pp. 1443–1454.

[59] Yasushi Miki. “Acoustical properties of porous materials-Modifications of Delany-Bazley models”. In: *Journal of the Acoustical Society of Japan (E)* 11.1 (1990), pp. 19–24.

[60] Domingo Muñoz-Esparza, Robert D Sharman, and Julie K Lundquist. “Turbulence dissipation rate in the atmospheric boundary layer: Observations

and WRF mesoscale modeling during the XPIA field campaign". In: *Monthly Weather Review* 146.1 (2018), pp. 351–371.

[61] CM Nyborg et al. "Propagation of wind turbine noise: measurements and model evaluation". In: *Journal of Physics: Conference Series*. Vol. 2265. 3. IOP Publishing. 2022, p. 032041.

[62] Stefan Oerlemans. "Effect of wind shear on amplitude modulation of wind turbine noise". In: *International Journal of Aeroacoustics* 14.5-6 (2015), pp. 715–728.

[63] Stefan Oerlemans and J Gerard Schepers. "Prediction of wind turbine noise and validation against experiment". In: *International journal of aeroacoustics* 8.6 (2009), pp. 555–584.

[64] Stefan Oerlemans, Pieter Sijtsma, and B Méndez López. "Location and quantification of noise sources on a wind turbine". In: *Journal of sound and vibration* 299.4-5 (2007), pp. 869–883.

[65] AG Olabi and Mohammad Ali Abdelkareem. "Renewable energy and climate change". In: *Renewable and Sustainable Energy Reviews* 158 (2022), p. 112111.

[66] Igho J Onakpoya et al. "The effect of wind turbine noise on sleep and quality of life: A systematic review and meta-analysis of observational studies". In: *Environment international* 82 (2015), pp. 1–9.

[67] Steven P Oncley et al. "Surface-layer fluxes, profiles, and turbulence measurements over uniform terrain under near-neutral conditions". In: *Journal of Atmospheric Sciences* 53.7 (1996), pp. 1029–1044.

[68] Vladimir E Ostashev and D Keith Wilson. *Acoustics in moving inhomogeneous media*. CRC Press, 2015.

[69] Vladimir E Ostashev and D Keith Wilson. "Relative Contributions from Temperature and Wind Velocity Fluctuations to the Statistical Moments of a Sound Field in a Turbulent Atmosphere". In: *Acta Acustica united with Acustica* 86.2 (2020), pp. 260–268.

[70] Vladimir E Ostashev, D Keith Wilson, and Michael B Muhlestein. "Wave and extra-wide-angle parabolic equations for sound propagation in a moving atmosphere". In: *The Journal of the Acoustical Society of America* 147.6 (2020), pp. 3969–3984.

[71] Vladimir E Ostashev et al. "Equations for finite-difference, time-domain simulation of sound propagation in moving inhomogeneous media and numerical implementation". In: *The Journal of the Acoustical Society of America* 117.2 (2005), pp. 503–517.

[72] Allan D Pierce. *Acoustics: an introduction to its physical principles and applications*. Springer, 2019.

[73] RD Pieren. "Auralization of Environmental Acoustical Sceneries: Synthesis of Road Traffic, Railway and Wind Turbine Noise". PhD thesis. Delft University of Technology, 2018.

[74] Reto Pieren, Thomas Bütler, and Kurt Heutschi. "Auralization of accelerating passenger cars using spectral modeling synthesis". In: *Applied Sciences* 6.1 (2015), p. 5.

[75] Reto Pieren and Dorothea Lincke. "Auralization of aircraft flyovers with turbulence-induced coherence loss in ground effect". In: *The Journal of the Acoustical Society of America* 151.4 (2022), pp. 2453–2460.

[76] Reto Pieren et al. "Auralization of railway noise: Emission synthesis of rolling and impact noise". In: *Applied Acoustics* 127 (2017), pp. 34–45.

[77] Reto Pieren et al. "Auralization of wind turbine noise: emission synthesis". In: *Acta Acustica United with Acustica* 100.1 (2014), pp. 25–33.

[78] Birger Plovsing. "Proposal for nordtest method: Nord2000–prediction of outdoor sound propagation". In: *DELTA Acoustics, Report AV* 1106.07 (2007).

[79] Stephen A Rizzi et al. "A comparison of aircraft flyover auralizations by the aircraft noise simulation working group". In: *AIAA AVIATION 2020 FORUM*. 2020, p. 2582.

[80] Michel Roger and Stéphane Moreau. "Extensions and limitations of analytical airfoil broadband noise models". In: *International Journal of Aeroacoustics* 9.3 (2010), pp. 273–305.

[81] Y Rozenberg, G Robert, and S Moreau. "Spectral model accounting for pressure gradient and Reynolds effects for the prediction of trailing-edge noise using RANS simulations". In: *AIAA J* 50.10 (2012), pp. 2168–2179.

[82] Yannick Rozenberg, Gilles Robert, and Stéphane Moreau. "Wall-pressure spectral model including the adverse pressure gradient effects". In: *AIAA journal* 50.10 (2012), pp. 2168–2179.

[83] Erik Salomons et al. "The Harmonoise sound propagation model". In: *Acta acustica united with acustica* 97.1 (2011), pp. 62–74.

[84] Erik M Salomons. *Computational atmospheric acoustics*. Springer Science & Business Media, 2001.

[85] Daniel Shepherd et al. "Evaluating the impact of wind turbine noise on health-related quality of life". In: *Noise and Health* 13.54 (2011), p. 333.

[86] Samuel Sinayoko, Mike Kingan, and Anurag Agarwal. "Trailing edge noise theory for rotating blades in uniform flow". In: *Proceedings of the Royal So-*

ciety A: Mathematical, Physical and Engineering Sciences 469.2157 (2013), p. 20130065.

[87] Oksana Stalnov, Paruchuri Chaitanya, and Phillip F Joseph. "Towards a non-empirical trailing edge noise prediction model". In: *Journal of Sound and Vibration* 372 (2016), pp. 50–68.

[88] Pontus Thorsson. "A Parametric Method to Synthesize Wind Turbine Sounds". In: *Proceedings of the 23rd International Congress on Acoustics : integrating 4th EAA Euroregio 2019 : 9-13 September 2019 in Aachen, Germany.*

[89] Yuan Tian and Benjamin Cotté. "Wind turbine noise modeling based on Amiet's theory: Effects of wind shear and atmospheric turbulence". In: *Acta Acustica united with Acustica* 102.4 (2016), pp. 626–639.

[90] GP Van den Berg. "The beat is getting stronger: the effect of atmospheric stability on low frequency modulated sound of wind turbines". In: *Journal of low frequency noise, vibration and active control* 24.1 (2005), pp. 1–23.

[91] GP Van den Berg. "Wind turbine power and sound in relation to atmospheric stability". In: *Wind Energy: An International Journal for Progress and Applications in Wind Power Conversion Technology* 11.2 (2008), pp. 151–169.

[92] GP Van den Berg. "Wind-induced noise in a screened microphone". In: *The Journal of the Acoustical Society of America* 119.2 (2006), pp. 824–833.

[93] Timothy Van Renterghem. "Sound propagation from a ridge wind turbine across a valley". In: *Philosophical Transactions of the Royal Society A: Mathematical, Physical and Engineering Sciences* 375.2091 (2017), p. 20160105.

[94] Michael Vorländer. *Auralization*. Springer, 2020.

[95] Siegfried Wagner, Rainer Bareiss, and Gianfranco Guidati. *Wind turbine noise*. Springer Science & Business Media, 2012.

[96] WW Willmarth and FW Roos. "Resolution and structure of the wall pressure field beneath a turbulent boundary layer". In: *Journal of Fluid Mechanics* 22.1 (1965), pp. 81–94.

[97] Branko Zajamsek et al. "Experimental and numerical investigation of blade–tower interaction noise". In: *Journal of Sound and Vibration* 443 (2019), pp. 362–375.

[98] Branko Zajamšek et al. "Characterisation of wind farm infrasound and low-frequency noise". In: *Journal of Sound and Vibration* 370 (2016), pp. 176–190.

[99] Wei Jun Zhu et al. "Modeling of Aerodynamically Generated Noise From Wind Turbines". In: *Journal of Solar Energy Engineering* 127.4 (June 2005), pp. 517–528.

[100] Wei Jun Zhu et al. “Wind turbine noise generation and propagation modeling at DTU Wind Energy: A review”. In: *Renewable and Sustainable Energy Reviews* 88 (2018), pp. 133–150.

DOCTORAL SCHOOL

Titre : Synthèse basée sur la physique du bruit des éoliennes

Mots clés : Bruit des éoliennes, synthèse basée sur la physique, turbulent inflow noise, trailing edge noise, window function, équation parabolique

Résumé : Il est connu que le bruit des éoliennes est une source potentielle de dérangement et de gêne pour les personnes vivant à proximité des parcs éoliens. Le travail présenté dans la thèse a abordé le problème du bruit des éoliennes en développant un modèle basé sur la physique pour le synthétiser et l'étudier. Le modèle de domaine fréquentiel pour le bruit des éoliennes prédit le bruit aéroacoustique à large bande généré par les pales en mouvement interagissant avec l'atmosphère turbulente. Le bruit du bord d'attaque et de fuite de la pale est prédit à l'aide de la théorie d'Ameit. Le bruit de bord de fuite utilise le spectre de pression de paroi calculé avec le modèle de Lee pour le côté aspiration et le modèle de Goody pour le côté aspiration. côté pression. Le bruit du bord d'attaque de la pale est prédit à l'aide du spectre de Kolmogorov pour la turbulence. L'équation parabolique dans un milieu en mouvement est utilisée pour tenir compte des effets de propagation de la réfraction et de la réflexion au sol. Le modèle Harmonoise est considéré comme prenant en compte la diffusion due à la turbulence. Le bruit des segments de pale est synthétisé sous forme de monopôles, se déplaçant à travers différentes couches de l'atmosphère. Un outil de synthèse est créé pour convertir les prédictions de bruit dans le domaine fréquentiel en un signal temporel à l'aide d'une fonction de fenêtre de fondu enchaîné. La fonction de fenêtre conçue est conçue pour tenir compte de la différence de temps de propagation observée en raison de la rotation des pales. Quelques cas de test du son synthétisé peuvent être trouvés dans la thèse pour différents scénarios. Le modèle est finalement comparé aux mesures de terrain effectuées pour l'ensemble d'un parc éolien et montre d'assez bons résultats tant pour la source que pour la partie propagation. Le modèle développé est un outil utile qui peut être utilisé pour l'évaluation psychoacoustique afin de comprendre la perception et le facteur de gêne du bruit des éoliennes. En plus d'obtenir les niveaux spectraux du bruit attendu du parc éolien, l'outil produit également des signaux sonores qui peuvent ensuite être utilisés aux fins souhaitées. Ce qui en fait un outil utile qui comble le fossé entre les citoyens, les collectivités locales et les acousticiens.

Title : Physics-based synthesis of wind turbine noise.

Keywords : Wind turbine noise, physics-based synthesis, turbulent inflow noise, trailing edge noise, adaptive window function, parabolic equation

Abstract : It is known that the wind turbine noise is a potential source of disturbance and annoyance for the people living in the vicinity of the wind farms. The work presented in the thesis addressed the problem of wind turbine noise by developing a physics-based model to synthesize and study it. The frequency-domain model for wind turbine noise predicts the broadband aeroacoustic noise generated by the moving blades interacting with the turbulent atmosphere. The noise from the leading and trailing edge of the blade are predicted using Ameit's theory. The trailing edge noise uses the wall pressure spectrum calculated with Lee's model for the suction side and Goody's model for the pressure side. The noise from the leading edge of the blade is predicted using the Kolmogorov spectrum for turbulence. The parabolic equation in moving medium is used to account for the propagation effects of refraction and ground reflection. The Harmonoise model is considered to account for the scattering due to turbulence. The noise from the blade segments are synthesized as monopoles, moving through different layers of the atmosphere. A synthesis tool is created to convert the frequency domain noise predictions to a time signal with the help of a cross-fading window function. The designed window function is made to account for the difference in the propagation time observed due to the rotation of the blades. A few test cases of the synthesized sound can be found in the thesis for different scenarios. The model is finally compared to the field measurements done for an entire wind farm and show fairly good results for the source as well as the propagation part. The developed model is a useful tool which can be used for psychoacoutic evaluation to understand the perception and annoyance factor of wind turbine noise. Along with obtaining the spectral levels of the expected noise from the wind farm, the tool also produces audible signals that can be further used for the desired purpose. Thus making it a useful tool that abridges the gap between citizens, local authorities and acousticians.

Institut Polytechnique de Paris
91120 Palaiseau, France